



US Army Corps
of Engineers
Waterways Experiment
Station

Technical Report HL-93-10
August 1993

AD-A269 870

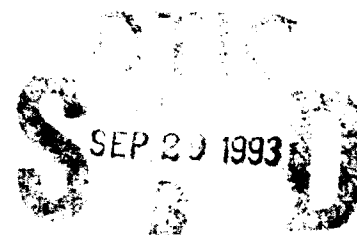


2

Free-Surface Flow Over Curved Surfaces

by *Rutherford C. Berger, Jr.*
Hydraulics Laboratory

Approved For Public Release; Distribution Is Unlimited



93-22561



Prepared for Headquarters, U.S. Army Corps of Engineers

The contents of this report are not to be used for advertising, publication, or promotional purposes. Citation of trade names does not constitute an official endorsement or approval of the use of such commercial products.



PRINTED ON RECYCLED PAPER

Technical Report HL-93-10
August 1993

Free-Surface Flow Over Curved Surfaces

by Rutherford C. Berger, Jr.
Hydraulics Laboratory

U.S. Army Corps of Engineers
Waterways Experiment Station
3909 Halls Ferry Road
Vicksburg, MS 39180-6199

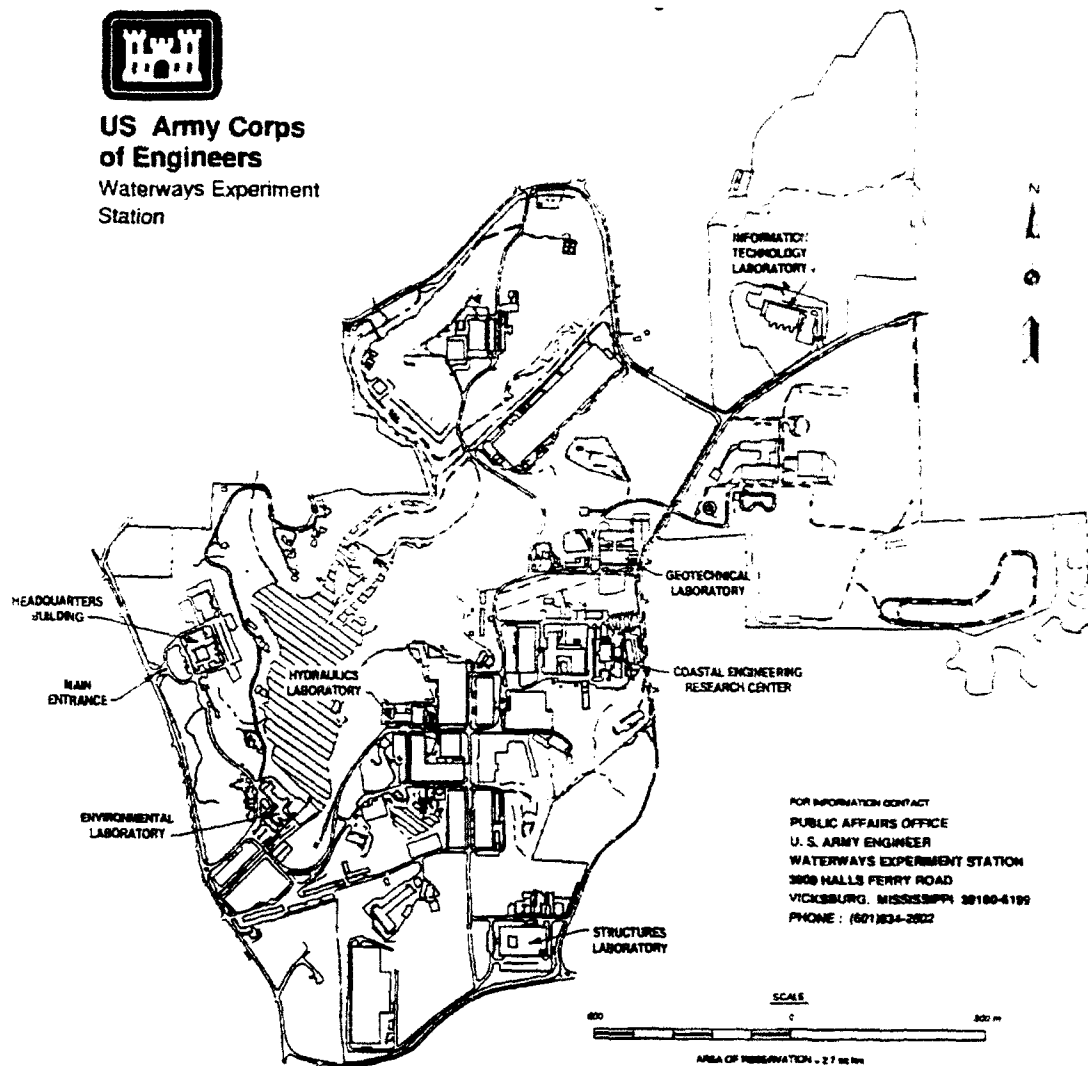
Final report

Approved for public release; distribution is unlimited

Prepared for U.S. Army Corps of Engineers
Washington, DC 20314-1000



**US Army Corps
of Engineers**
Waterways Experiment
Station



FOR INFORMATION CONTACT
PUBLIC AFFAIRS OFFICE
U. S. ARMY ENGINEER
WATERWAYS EXPERIMENT STATION
3800 HALLS FERRY ROAD
VICKSBURG, MISSISSIPPI 39180-6199
PHONE : (601)834-2822

Waterways Experiment Station Cataloging-in-Publication Data

Berger, Rutherford C.

Free-surface flow over curved surfaces / by Rutherford C. Berger, Jr. ;
prepared for U.S. Army Corps of Engineers.

149 p. : ill. ; 28 cm. -- (Technical report; HL-93-10)

1. Hydrodynamics -- Statistical methods. 2. Channels (Hydraulic
engineering) 3. Cavitation -- Mathematical models. 4. Finite element
method. I. United States. Army. Corps of Engineers. II. U.S. Army En-
gineer Waterways Experiment Station. III. Title. IV. Series: Technical
report (U.S. Army Engineer Waterways Experiment Station); HL-93-10.
TA7 W34 no.HL-93-10

Table of Contents

List of Tables	v
List of Figures	vi
Preface	ix
1. Introduction	1
1.1 Background	3
1.2 Previous Research	4
1.3 Objectives	8
1.4 Important Results	9
1.5 Outline of Treatment	10
2. Equation Development	12
2.1 Basic Equations	12
2.2 Perturbation Analysis	18
2.3 Generalized Shallow Water Equations	22
3. One-Dimensional Problem and Exploratory Studies	24
3.1 Introduction	24
3.2 One-Dimensional Equations	26
3.3 Discussion	27
3.4 Finite Element Approximation	30
3.4.1 Choice of Basis	30
3.4.2 Artificial Dissipation	32
3.4.3 Finite Element Approximation	37
3.5 Model Results	38

3.6	Conclusions	44
4.	Model Extensions	46
4.1	Introduction	46
4.2	Finite Element Treatment - Convection Scheme	47
4.3	Model Equations	55
4.4	Application to Generalized Equations	58
4.5	Viscous Stress	61
4.6	Bed Drag	62
4.7	Model Description	64
5.	Validation and Practical Simulation	67
5.1	Model Validation	67
5.1.1	Constant Curvature	68
5.1.2	Variable Curvature	74
5.2	Comparison to Physical Measurements in Flumes	77
5.2.1	Supercritical Transition	78
5.2.2	Spillway Form	83
5.2.3	Outletworks Flume	91
5.3	Discussion	104
6.	Conclusion	112
A.	Integration of Coefficients	117
	BIBLIOGRAPHY	125

SF 298

List of Tables

4.1	Number of boundary conditions required.	60
5.1	Circular channel, subcritical flow.	69
5.2	Circular channel subcritical flow results.	69
5.3	Circular channel, supercritical flow.	73
5.4	Circular channel supercritical flow results.	73
5.5	Variable curvature flume.	75
5.6	Variable curvature flow results.	77
5.7	Supercritical transition.	80
5.8	Spillway form.	85
5.9	Outletworks model.	96

Approved For	
Name	<input checked="" type="checkbox"/>
Date	<input type="checkbox"/>
Signature	<input type="checkbox"/>
<small> Approved For Date Signature </small>	
<div style="font-size: 2em; font-weight: bold; margin-left: 10px;">A-1</div>	

List of Figures

1.1	Hydraulic spillway model.	2
1.2	One-dimensional equation coordinate system.	6
2.1	Bed-fitted coordinate system.	14
3.1	Average velocity profile — effect of curvature terms.	40
3.2	Pressure ratio profile — centrifugal/hydrostatic pressure.	41
3.3	Water surface profile — effect of curvature terms.	42
3.4	Water surface profile — effect of refinement.	44
4.1	Infinitesimal volume for calculation of bed drag force.	63
4.2	Local bilinear element.	65
5.1	Circular channel, subcritical flow: bed velocity and water surface elevation.	70
5.2	Circular channel, subcritical flow: comparison of depth from model with analytic solution.	71
5.3	Circular channel, subcritical flow: comparison of the bed velocity from the model with analytic solution.	72
5.4	Circular channel, supercritical flow: bed velocity and water surface elevation profiles.	74

5.5	Circular channel, supercritical flow: comparison of depth from model with analytic solution.	75
5.6	Circular channel, supercritical flow: comparison of the bed velocity from the model with analytic solution.	76
5.7	Flume geometry: supercritical transition.	78
5.8	Computational grid, supercritical transition.	79
5.9	Supercritical transition: water surface, 3-d perspective view. . .	81
5.10	Supercritical transition: comparison of water surface contours, all units ft.	82
5.11	Spillway form: comparison of water surface results.	85
5.12	Geometry for mild-slope evaluation.	87
5.13	Subcritical flow: water surface slope comparison.	88
5.14	Supercritical flow: water surface slope comparison.	89
5.15	Spillway form: comparison of bed pressure results.	89
5.16	Spillway form: shallowness parameter.	90
5.17	Outletworks flume: flume and numerical model geometry.	92
5.18	Outletworks flume: water surface results, perspective view. . . .	95
5.19	Outletworks model: computational mesh.	96
5.20	Outletworks flume: depth contours.	97
5.21	Outletworks model: generalized shallow water equations, depth contours.	98

5.22 Outletworks model: standard steep-slope shallow water equations, depth contours.	98
5.23 Outletworks model: St. Venant equations, depth contours.	99
5.24 Outletworks flume: lateral depth profiles.	100
5.25 Outletworks model: generalized shallow water equations, lateral depth profiles.	101
5.26 Outletworks model: standard steep-slope shallow water equations, lateral depth profiles.	102
5.27 Outletworks flume: lateral velocity profiles, $x = 1.0\text{ft}$	104
5.28 Outletworks flume: lateral velocity profiles, $x = 1.6\text{ft}$	108
5.29 Outletworks flume: lateral velocity profiles, $x = 2.8\text{ft}$	109
5.30 Outletworks flume: lateral velocity profiles, $x = 5.0\text{ft}$	110
5.31 Spillway capacity ratio.	111

PREFACE

This report is the product of research conducted from 1986 to 1992 by Dr. R. C. Berger, Jr., of the Estuaries Division (ED), Hydraulics Laboratory (HL), U.S. Army Engineer Waterways Experiment Station (WES). Dr. Berger is under the general supervision of Messrs. F. A. Herrmann, Jr., Director, HL; R. A. Sager, Assistant Director, HL; and W. H. McAnally, Chief, ED.

This report is a dissertation in partial fulfillment of the requirements for the degree of Doctor of Philosophy from the University of Texas at Austin.

This work is a result of contributions by several people. Dr. Graham Carey as advisor has provided sound advice and suggestions for this work as well as navigation through graduate school. The author would also like to thank the advisory committee, Professors Larry Mack, Harry Swinney, Linda Hayes, and Tinsley Oden, for their interest and participation. Mr. Charles Tate and Mr. James Cessna, WES, modified the flume and collected the outlet works data.

At the time of publication of this report, Director of WES was Dr. Robert W. Whalin. Commander was COL Bruce K. Howard, EN.

Chapter 1

Introduction

Flood flows in excess of a reservoir's capacity must be passed downstream in a manner which does not endanger the dam or surrounding hydraulic structures. This is not a trivial task as the flow must fall a great distance to reach the river bed. These high current velocities coupled with a free-surface can easily lead to regions of low pressure in which cavitation may occur or to the formation of standing waves and an uneven flow distribution. Poor flow distribution will yield circulation and high velocities at the base of the spillway (or outlet channel) known as the "stilling basin," resulting in downstream scour, potentially undermining the structure and causing both bank erosion and stilling basin damage.

Presently, the design of these structures is accomplished primarily through large scale hydraulic models. An example is the Grapevine Emergency Spillway Model at the Waterways Experiment Station (WES) shown in Figure 1.1. A large scale is necessary to eliminate scale-effects due to the viscosity of the model fluid; i.e., the same fluid (water) is used as in the field problem. The model shown is a 1:60 undistorted scale reproduction of the spillway section and the apron; it includes a portion of the upstream reservoir and the channel downstream. In the figure we see the jump at the toe of the spillway apron, in which the flow rapidly decelerates and becomes subcriti-



Figure 1.1: Hydraulic Spillway Model.

cal. Along the apron the flow is supercritical (flow velocity is greater than the wave speed) and in this case is relatively smooth. If the upstream approach conditions are poor, oblique jumps will develop producing circulation in the downstream subcritical channel. This will cause excessive scour and damage. The model is used to eliminate the cause of poor circulation. The model is rebuilt or modified for each design trial; e.g., by sidewall boundary reshaping and changing the bed's lateral curvature. Each modification is expensive to construct and time consuming. A detailed numerical model could significantly reduce the design costs and enhance understanding of the flow phenomena.

1.1 Background

A principal aspect of high velocity flow associated with spillways and outlet channels is the formation of standing waves. A disturbance caused by an obstacle in the flow or by lateral transition will propagate out away from the source. If the flow velocity is faster than the wave celerity, c , the disturbance cannot travel upstream. Instead it will be swept downstream forming a wake or standing wave.

The wave celerity is dependent upon its wavelength [40] and is given by

$$c = [(g\lambda/2\pi) \tanh(2\pi h/\lambda)]^{1/2} \quad (1.1)$$

where, c is the wave celerity, g is the acceleration of gravity λ is the wavelength, and h is depth. The dispersion of these wavelengths is a result of the reduction of the pressure gradient due to the vertical accelerations (with the shorter wavelengths more greatly affected).

From (1.1), the maximum celerity is associated with the longest wavelength/depth ratio and has a value $c_{max} = (gh)^{\frac{1}{2}}$. Thus, if the Froude Number, $F_r \equiv \frac{|v|}{(gh)^{\frac{1}{2}}}$ (where, v is the flow velocity), is greater than unity all wavelengths will propagate downstream. This is known as supercritical flow. Conversely, if $F_r < 1$ the flow is subcritical. A common simplification in numerical modeling of these flows is the long-wave or shallow water approximation. This results in a hydrostatic pressure distribution with all wavelengths having the same celerity, c_{max} .

1.2 Previous Research

One approach to flow over curved beds in hydraulic modeling is through the use of potential flow theory. The water surface is determined via the Bernoulli equation. An inverse approach in which the coordinates are the dependent variables and the stream function and velocity potential are independent variables has been used by several researchers, e.g. see Watters and Street [62] for an early application and Cassidy [10] and Moayeri [44] for methods which handled more general geometry.

Examples of the direct approach are given in Bettles and Bettles [7] and Ikegawa and Washizu [30]. Here the stream function and velocity potential are the dependent variables. The grids adapt to follow the water surface. These examples are two-dimensional (longitudinal and vertical resolution) and thus cannot determine the standing wave patterns and nonuniform flow distributions laterally.

Another approach is to use the shallow water equations. These equa-

tions may be derived following the procedure originated by Friedrichs [24] and extended by Keller [35] (see also Stoker [56]) by utilizing an asymptotic expansion in a shallowness parameter

$$\varepsilon \equiv \left(\frac{d}{l}\right)^2 \quad (1.2)$$

where, l is the radius of curvature of the free-surface and d is a characteristic depth. To lowest order, the standard shallow water equations are hydrostatic and assume a small channel slope, these equations are referred to as the St. Venant equations [50]. There have been applications to conditions of high velocity (see e.g. [39, 16, 32]), but the assumption of mild slope and hydrostatic pressure limits its use in some practical applications such as spillway simulations.

A nonhydrostatic pressure distribution may be incorporated by including higher-order terms (see Abbott and Rodenhuis [2]) known as the Boussinesq terms. Applications of these equations to supercritical flow have been made by Gharangik and Chaudry [26], though the bed is again assumed to have a mild slope and the equation set involves higher derivatives.

Dressler [20] produced a more general set of one-dimensional shallow water equations, in which channel bed curvature is included without resorting to incorporation of higher-order terms in the shallowness expansion. This formulation leads to the equations

$$\hat{u}_t + \frac{\hat{u}\hat{u}_{s_1}}{J(h)^2} + \left\{ g \cos \theta + \frac{\kappa \hat{u}^2}{J(h)^3} \right\} h_{s_1} - \left\{ \kappa g \sin \theta - \frac{\kappa_{s_1} \hat{u}^2}{J(h)^3} \right\} h + g \sin \theta = 0 \quad (1.3)$$

$$h_t + \frac{\hat{u}h_{s_1}}{J(h)^2} - \frac{\log \{J(h)\}}{J(h)\kappa} \hat{u}_{s_1} + \frac{\kappa_{s_1}}{\kappa} \left\{ \frac{\kappa h}{J(h)^2} + \frac{\log \{J(h)\}}{J(h)} \right\} \hat{u} = 0 \quad (1.4)$$

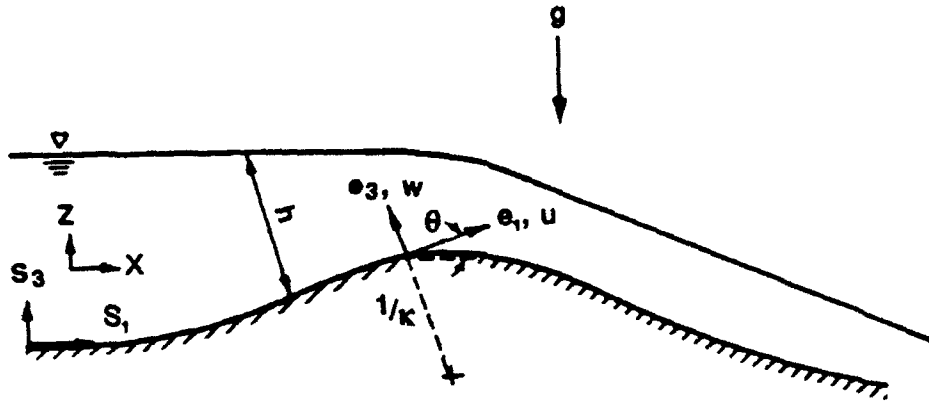


Figure 1.2: One-dimensional equation coordinate system.

$$w(s_1, s_3, t) = \frac{\log \{J(s_3)\} \hat{u}_{s_1}}{J(s_3) \kappa} - \frac{\kappa_{s_1}}{\kappa^2} \left\{ \frac{\kappa s_3}{J(s_3)^2} + \frac{\log \{J(s_3)\}}{J(s_3)} \right\} \hat{u} = 0 \quad (1.5)$$

$$P(s_1, s_3, t) = \rho g \cos \theta \{h - s_3\} + \frac{\rho \hat{u}^2}{2} \{J(h)^{-2} - J(s_3)^{-2}\} \quad (1.6)$$

where alphabetic subscripts indicate differentiation and the pertinent variables are (see Figure 1.2):

t is time

s_1 is the coordinate parallel to flow bed

s_3 is the coordinate orthogonal to s_1

κ is the bed curvature; $\kappa(s_1)$

θ is the angle from horizontal to the tangent of the channel bed;

$\theta(s_1)$

h is the depth; $h(s_1, t)$

J is the jacobian, $J = (1 - \kappa(s_1)s_3)$; $J(s_1, s_3)$

P is the pressure

- u is the current velocity in the s_1 direction $u = \hat{u}/J(s_3)$; $u(s_1, s_3, t)$
- \hat{u} is the current velocity in the s_1 direction at the channel bottom,
i. e., $\hat{u} = u(s_1, 0, t)$
- w is the current velocity in the s_3 direction; $w(s_1, s_3, t)$
- ρ is the density, assumed to be a constant
- g is the acceleration of gravity.

Dressler's expansion is applied to the two-dimensional Euler equations in the orthogonal curvilinear system defined by s_1, s_3 . In the same manner as Friedrichs, irrotationality is assumed. The other basic assumptions are constant density, no lateral variation and that the ambient surface pressure is zero. The usual kinematic surface conditions, of no penetration at the channel bed and that a particle on the free-surface remains on the surface, are enforced. The irrotationality assumption is reasonable for converging flow [38], as is the case in the vicinity of the spillway crest. Even after the development of the turbulent boundary layer this assumption for the flow profile is quite reasonable. The resistive action of the channel and eddy viscosities resulting from turbulence can be included in an empirical term like the Chezy formula. Furthermore, Dressler [21] developed corrections to the Chezy and Manning coefficients to accommodate bed curvature.

Dressler's formulation yields u , h , and P to order ϵ^0 and w to order ϵ^1 . (The value of w to order ϵ^0 is simply $w \equiv 0$ which is identical to the result in standard shallow water theory.) Given the zero-order perturbation for the solution u and h , the next higher approximation of w may be calculated. This treatment utilizes evaluation of the equations at the channel bed to re-

move some complicating terms. Sivakumaran [51, 52] generalizes the derivation further to a two-dimensional surface. Again, irrotationality is assumed. The one-dimensional equations when evaluated at the bed then become:

$$J(h)h_t + \frac{\partial}{\partial s_1} \left[-\frac{\hat{u}}{\kappa} \log [J(h)] \right] = 0 \quad (1.7)$$

$$\hat{u}_t + gE_{s_1} = 0 \quad (1.8)$$

where,

$$E(s_1, t) \equiv \zeta + h \cos \theta + \frac{P_o}{\rho g} + \frac{1}{J(h)^2} \frac{\hat{u}^2}{2g}$$

$$\frac{P - P_o}{\rho g} = [h - s_3] \cos \theta + [J(h)^{-2} - J(s_3)^{-2}] \frac{\hat{u}^2}{2g} \quad (1.9)$$

$$w = \frac{1}{J(s_3)} \frac{\partial}{\partial s_1} \left[\frac{\hat{u}}{\kappa} \log \{J(s_3)\} \right] \quad (1.10)$$

and ζ is the elevation of the bed above some reference level with P_o the ambient pressure at the free-surface. Both of these sets shall be referred to as Dressler's equations throughout the present study as these two formulations are equivalent. This model appears applicable for $-0.85 \leq \kappa h < 0.5$ and Sivakumaran [51, 53] has demonstrated a good agreement with experimental results over the wider range $-2 \leq \kappa h \leq 0.54$.

1.3 Objectives

The principal objective of this present research is to develop and evaluate a generalized set of shallow water equations containing bed curvature effects to simulate important aspects of flow over curved beds, specifically associated with spillways or outlet works.

Subordinate objectives in support of the primary aim are:

1. Via a perturbation analysis develop the generalized set of shallow equations without excluding vorticity about the direction normal to the bed.
2. Develop a one-dimensional finite element model for preliminary tests of these equations with a particular emphasis on the effects of curvature. Results will be compared to the steep-slope shallow water equations which do not include bed curvature.
3. Develop a two-dimensional numerical model of this equation set.
 - (a) Make self-consistency test of the model to demonstrate that the model matches the derived equations.
 - (b) Test the numerical method employed by comparison to flume water surface data.
 - (c) Make comparisons to flume results for these equations, the standard steep-slope shallow water equations and the St. Venant equations.

1.4 Important Results

The important results from this work are:

1. The development of a system of nonhydrostatic two-dimensional shallow water equations that are not restricted to irrotationality.
2. A comparison with the standard steep-slope shallow water equations reveals unexpected errors upstream of a simulated dam crest.
3. A numerical scheme that shows promise for super- and subcritical flow in hydrodynamic modeling.

4. An in-depth comparison of the usefulness and limitations of these new equations along with more traditional St. Venant and steep-slope standard shallow water equations.
5. A numerical model capable of numerically simulating hydraulic flow along chute spillways and outlet works.
6. A data set of water surface elevations from an outlet works that is of general use.

1.5 Outline of Treatment

A general set of shallow water equations which is nonhydrostatic and which allows vorticity is derived in Chapter 2. The derivation involves an asymptotic expansion in a shallowness parameter for the bed-fitted Euler equations. Preliminary testing of these equations in one dimension is conducted in Chapter 3. A comparison with a standard steep-slope shallow water equation set is made. In Chapter 4 we detail the development of the two-dimensional model with special attention to a numerical scheme to better treat the highly convective flow conditions. A more in-depth set of tests is then conducted for the two-dimensional generalized shallow water equations (Chapter 5). We first test the validity of the code for several test problems. The numerical scheme and the treatment of boundary conditions are then compared with the measured water surface in a flume for a supercritical transition. The influence of curvature and the mild-slope assumption (for the St. Venant equations) are made apparent by comparison with previously collected flume data. The most general test of the equations is a comparison to water surface of an outlet-

works flume. Here the bed contains curvature and there are lateral transitions. Tests on this configuration are made for the St. Venant equations, the steep-slope standard shallow water equations and the generalized set by comparison of predicted water surface elevations with flume results. Chapter 6 contains conclusions concerning the usefulness of these equations, their advantages and disadvantages, and recommendations for additional research.

Chapter 2

Equation Development

The free-surface and the nonhydrostatic pressure aspects of the flow were included in the previous equations, but vorticity about the bed-normal direction was excluded. It is important that eddy patterns and vorticity resulting from sidewalls and the drag due to bottom friction be reflected in the equations to distinguish the design alternatives. Also, the variation in pressure due to curvature, in fact, may rival that of the hydrostatic pressure. These problems cannot be adequately modeled using the previous perturbation formulations. The present approach yields a more general formulation that does not restrict vorticity about bed-normal axes while including bed-curvature effects.

The derivation developed here employs concepts common to the studies of Friedrichs, Keller and Dressler and also involves easing of the irrotationality restriction with extension to a two-dimensional surface. The basic approach is to use an asymptotic expansion of the dependent variables of the three-dimensional Euler equations (written for an orthogonal curvilinear coordinate system) in a shallowness parameter ϵ .

2.1 Basic Equations

The derivation begins with the Euler equations:

$$\nabla \cdot \mathbf{v} = 0 \quad (2.1)$$

$$\mathbf{v}_t + \frac{1}{2}\nabla(\mathbf{v} \cdot \mathbf{v}) - \mathbf{v} \times \boldsymbol{\omega} + \frac{1}{\rho}\nabla P - \mathbf{g} = \mathbf{0} \quad (2.2)$$

where, $\boldsymbol{\omega}$ is the vorticity vector, and \mathbf{g} is the body force per unit mass. The free-surface kinematic boundary condition requires that a particle on the surface remain on the surface, so that

$$h(s_1, s_2, t) - s_3 = 0 \quad (2.3)$$

This may be written

$$h_t + \mathbf{v}(s_1, s_2, h, t) \cdot \nabla h = w(s_1, s_2, h, t) \quad (2.4)$$

where, u , v , and w are in the s_1 , s_2 , and s_3 directions, respectively. There is also a bottom kinematic boundary condition that the velocity normal to the bed be zero. This implies

$$w(s_1, s_2, 0, t) = 0 \quad (2.5)$$

The pressure at the free-surface is a constant, here taken as the reference value zero,

$$P(s_1, s_2, h, t) = 0 \quad (2.6)$$

The irrotationality condition implies that the vorticity vector components in the s_1 and s_2 directions are zero,

$$\omega_1 = \omega_2 = 0 \quad (2.7)$$

The coordinate system shown in Figure 2.1 is a mutually orthogonal system. The coordinate directions s_1 and s_2 are in fact curvilinear, and s_3 is normal to the surface so defined. Therefore, $s_3(x, y, z) = c$ (where x, y, z

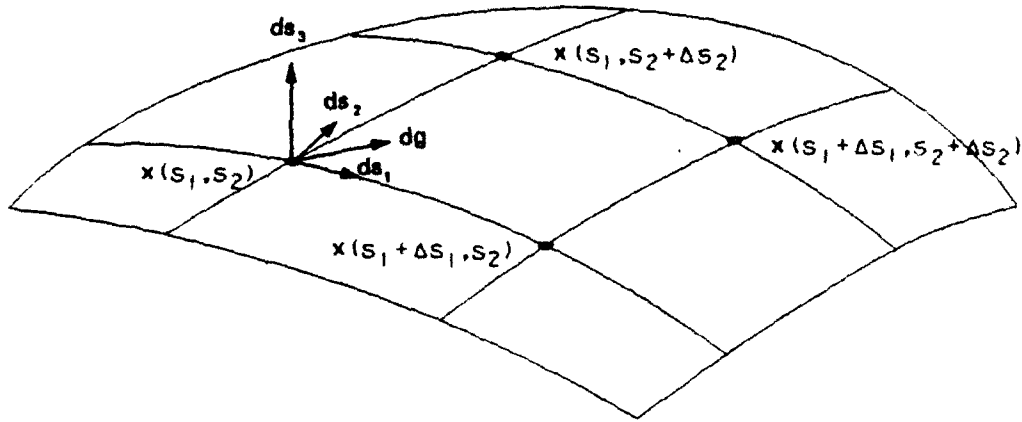


Figure 2.1: Bed-fitted coordinate system.

are cartesian coordinates) defines a coordinate surface above the bed. An infinitesimal vector \mathbf{dg} that lies within the bed has a length given by

$$|\mathbf{dg}|^2 = \left(\frac{\partial \mathbf{x}}{\partial s_1} ds_1 + \frac{\partial \mathbf{x}}{\partial s_2} ds_2 \right) \cdot \left(\frac{\partial \mathbf{x}}{\partial s_1} ds_1 + \frac{\partial \mathbf{x}}{\partial s_2} ds_2 \right)$$

or,

$$|\mathbf{dg}|^2 = \zeta_1^2 (ds_1)^2 + \zeta_2^2 (ds_2)^2$$

where,

$$\zeta_1 = \left(\frac{\partial \mathbf{x}}{\partial s_1} \cdot \frac{\partial \mathbf{x}}{\partial s_1} \right)^{\frac{1}{2}}$$

$$\zeta_2 = \left(\frac{\partial \mathbf{x}}{\partial s_2} \cdot \frac{\partial \mathbf{x}}{\partial s_2} \right)^{\frac{1}{2}}$$

and \mathbf{x} is a position vector. For the surface-normal coordinate $\left(\frac{\partial \mathbf{x}}{\partial s_3} \cdot \frac{\partial \mathbf{x}}{\partial s_3} \right)^{\frac{1}{2}} \equiv 1$. As one moves along the s_3 direction, ζ_1 and ζ_2 are scaled in relation to s_3

as $j_1 \equiv \zeta_1(1 - \kappa_1 s_3)$ and similarly for the s_2 direction. This formulation of the metrics requires that s_1 and s_2 not only be orthogonal but also principal directions. The curvature in the s_1 direction, for example, is given by, (see [41]):

$$\kappa_1 = -\frac{\frac{\partial \mathbf{x}}{\partial s_1}}{\left(\frac{\partial \mathbf{x}}{\partial s_1} \cdot \frac{\partial \mathbf{x}}{\partial s_1}\right)^{\frac{1}{2}}} \cdot \frac{\frac{\partial \mathbf{N}}{\partial s_1}}{\left(\frac{\partial \mathbf{x}}{\partial s_1} \cdot \frac{\partial \mathbf{x}}{\partial s_1}\right)^{\frac{1}{2}}} \quad (2.8)$$

Where \mathbf{N} is the unit vector normal to the $s_1 - s_2$ surface; if $\frac{\partial \mathbf{N}}{\partial s_1}$ is parallel to the s_1 tangent vector then the curvature along s_1 is an extremum and s_1 is a principal direction. The normal vector remains in the $s_1 - s_3$ plane: s_2 is normal to s_1 and hence is also a principal direction. Introducing this coordinate system (2.1)-(2.7) and simplifying, we find the following equation set.

Continuity Equation:

$$\frac{\partial(j_2 u)}{\partial s_1} + \frac{\partial(j_1 v)}{\partial s_2} + \frac{\partial(j_1 j_2 w)}{\partial s_3} = 0 \quad (2.9)$$

s_1 Momentum Equation:

$$u_t + \frac{u}{j_1} u_{s_1} + \frac{v}{j_2} u_{s_2} + w u_{s_3} - \frac{v^2}{j_1 j_2} \frac{\partial j_2}{\partial s_1} + \frac{uv}{j_1 j_2} \frac{\partial j_1}{\partial s_2} - \left(\frac{\zeta \kappa}{j}\right)_1 u w + \frac{1}{j_1 \rho} P_{s_1} - g_1 = 0 \quad (2.10)$$

s_2 Momentum Equation:

$$v_t + \frac{u}{j_1} v_{s_1} + \frac{v}{j_2} v_{s_2} + w v_{s_3} - \frac{u^2}{j_1 j_2} \frac{\partial j_1}{\partial s_2} + \frac{uv}{j_1 j_2} \frac{\partial j_2}{\partial s_1} - \left(\frac{\zeta \kappa}{j}\right)_2 v w + \frac{1}{j_2 \rho} P_{s_2} - g_2 = 0 \quad (2.11)$$

s_3 Momentum Equation:

$$w_t + \frac{u}{j_1} w_{s_1} + \frac{v}{j_2} w_{s_2} + w w_{s_3} + \left(\frac{\zeta \kappa}{j}\right)_1 u^2 + \left(\frac{\zeta \kappa}{j}\right)_2 v^2 + \frac{1}{\rho} P_{s_3} - g_3 = 0 \quad (2.12)$$

Irrotationality Condition:

$$w_{s_2} - (j_2 v)_{s_3} = 0 \quad (2.13)$$

$$(j_1 u)_{s_3} - w_{s_1} = 0 \quad (2.14)$$

Free-Surface Boundary Conditions (at $s_3 = h$):

$$h_t + \frac{u}{j_1} h_{s_1} + \frac{v}{j_2} h_{s_2} = w \quad (2.15)$$

$$P(s_1, s_2, h, t) = 0 \quad (2.16)$$

Channel Bed Boundary Condition:

$$w(s_1, s_2, 0, t) = 0 \quad (2.17)$$

These equations are quite complex and our objective now is to extract the important simplifications of these equations that result when the flow depth is small.

In the manner of Friedrichs, the equations may be nondimensionalized and the dependent variables expanded in powers of ε . Typical length scales are the depth " d " and the free-surface radius of curvature " l ". As in shallow water theory the relationship with velocity and thus time is assumed by the approximate celerity of a free-surface wave, $(gd)^{\frac{1}{2}}$ [56].

Nondimensionalizing, we let α , β , γ and τ be the new independent variables so that

$$\begin{aligned} s_1 &= l\alpha & u &= (gd)^{\frac{1}{2}} \tilde{u} & \zeta_1 &= \tilde{\zeta}_1 & \kappa_1 &= \tilde{\kappa}_1/d & j_1 &= \zeta_1 (1 - \tilde{\kappa}_1 \beta) \\ s_2 &= l\gamma & v &= (gd)^{\frac{1}{2}} \tilde{v} & \zeta_2 &= \tilde{\zeta}_2 & \kappa_2 &= \tilde{\kappa}_2/d & j_2 &= \zeta_2 (1 - \tilde{\kappa}_2 \beta) \\ s_3 &= d\beta & w &= \frac{l(gd)^{\frac{1}{2}}}{d} \tilde{w} & P &= \rho g d \pi & t &= \frac{l}{(gd)^{\frac{1}{2}}} \tau & \left(\frac{d}{l}\right)^2 &\equiv \varepsilon \\ h &= dY \end{aligned} \quad (2.18)$$

where the tildes (\sim) indicate nondimensional quantities. Recasting the governing equations in the dimensionless form and then dropping the tildes for convenience, equations (2.9)-(2.17) become

Continuity Equation:

$$\varepsilon \{ (j_2 u)_\alpha + (j_1 v)_\gamma \} + (j_1 j_2 w)_\beta = 0 \quad (2.19)$$

α Momentum Equation:

$$\varepsilon \left\{ u_\tau + \frac{u}{j_1} u_\alpha + \frac{v}{j_2} u_\gamma - \frac{v^2}{j_1 j_2} \frac{\partial j_2}{\partial \alpha} + \frac{uv}{j_1 j_2} \frac{\partial j_1}{\partial \gamma} + \frac{\pi_\alpha}{j_1} - F \right\} + w u_\beta - \left(\frac{\zeta \kappa}{j} \right)_1 u w = 0 \quad (2.20)$$

γ Momentum Equation:

$$\varepsilon \left\{ v_\tau + \frac{u}{j_1} v_\alpha + \frac{v}{j_2} v_\gamma - \frac{u^2}{j_1 j_2} \frac{\partial j_1}{\partial \gamma} + \frac{uv}{j_1 j_2} \frac{\partial j_2}{\partial \alpha} + \frac{\pi_\gamma}{j_2} - G \right\} + w v_\beta - \left(\frac{\zeta \kappa}{j} \right)_2 v w = 0 \quad (2.21)$$

β Momentum Equation:

$$\varepsilon \left\{ w_\tau + \frac{u}{j_1} w_\alpha + \frac{v}{j_2} w_\gamma + \left(\frac{\zeta \kappa}{j} \right)_1 u^2 + \left(\frac{\zeta \kappa}{j} \right)_2 v^2 + \pi_\beta - H \right\} + w w_\beta = 0 \quad (2.22)$$

Irrotationality Condition:

$$w_\gamma - (j_2 v)_\beta = 0 \quad (2.23)$$

$$(j_1 u)_\beta - w_\alpha = 0 \quad (2.24)$$

Free-Surface Boundary Conditions (at $\beta = Y$):

$$\varepsilon \left\{ Y_\tau + \frac{u}{j_1} Y_\alpha + \frac{v}{j_2} Y_\gamma \right\} = w \quad (2.25)$$

$$\pi(\alpha, \gamma, Y, \tau) = 0 \quad (2.26)$$

Channel Bed Boundary Condition:

$$w(\alpha, \gamma, 0, \tau) = 0 \quad (2.27)$$

2.2 Perturbation Analysis

A perturbation analysis in ϵ is now developed for the flow equations in the curvilinear system. We expand each dependent variable in a power series in ϵ as follows:

$$\begin{aligned}
 u(\alpha, \gamma, \beta, \tau; \epsilon) &= u^{(0)}(\alpha, \gamma, \beta, \tau) + \epsilon u^{(1)}(\alpha, \gamma, \beta, \tau) + \dots \\
 v(\alpha, \gamma, \beta, \tau; \epsilon) &= v^{(0)}(\alpha, \gamma, \beta, \tau) + \epsilon v^{(1)}(\alpha, \gamma, \beta, \tau) + \dots \\
 w(\alpha, \gamma, \beta, \tau; \epsilon) &= w^{(0)}(\alpha, \gamma, \beta, \tau) + \epsilon w^{(1)}(\alpha, \gamma, \beta, \tau) + \dots \quad (2.28) \\
 \pi(\alpha, \gamma, \beta, \tau; \epsilon) &= \pi^{(0)}(\alpha, \gamma, \beta, \tau) + \epsilon \pi^{(1)}(\alpha, \gamma, \beta, \tau) + \dots \\
 Y(\alpha, \gamma, \beta, \tau; \epsilon) &= Y^{(0)}(\alpha, \gamma, \beta, \tau) + \epsilon Y^{(1)}(\alpha, \gamma, \beta, \tau) + \dots
 \end{aligned}$$

These expansions are substituted into equations: (2.19)-(2.27) yielding:

$$\begin{aligned}
 \epsilon \left\{ [j_2 u(\alpha, \gamma, \beta, \tau; \epsilon)]_\alpha + [j_1 v(\alpha, \gamma, \beta, \tau; \epsilon)]_\gamma \right\} \\
 + [j_1 j_2 w(\alpha, \gamma, \beta, \tau; \epsilon)]_\beta = 0 \quad (2.29)
 \end{aligned}$$

$$\begin{aligned}
 \epsilon \left\{ [u(\alpha, \gamma, \beta, \tau; \epsilon)]_\tau + \frac{1}{j_1} u(\alpha, \gamma, \beta, \tau; \epsilon) [u(\alpha, \gamma, \beta, \tau; \epsilon)]_\alpha \right. \\
 + \frac{1}{j_2} v(\alpha, \gamma, \beta, \tau; \epsilon) [u(\alpha, \gamma, \beta, \tau; \epsilon)]_\gamma \\
 - \frac{1}{j_1 j_2} [v(\alpha, \gamma, \beta, \tau; \epsilon)]^2 \frac{\partial j_2}{\partial \alpha} + \frac{1}{j_1 j_2} u(\alpha, \gamma, \beta, \tau; \epsilon) v(\alpha, \gamma, \beta, \tau; \epsilon) \frac{\partial j_1}{\partial \gamma} \\
 \left. + \frac{1}{j_1} [\pi(\alpha, \gamma, \beta, \tau; \epsilon)]_\alpha - F \right\} + w(\alpha, \gamma, \beta, \tau; \epsilon) [u(\alpha, \gamma, \beta, \tau; \epsilon)]_\beta \\
 - \left[\frac{\zeta \kappa}{j} \right]_1 u(\alpha, \gamma, \beta, \tau; \epsilon) w(\alpha, \gamma, \beta, \tau; \epsilon) = 0 \quad (2.30)
 \end{aligned}$$

$$\epsilon \left\{ [v(\alpha, \gamma, \beta, \tau; \epsilon)]_\tau + \frac{1}{j_1} u(\alpha, \gamma, \beta, \tau; \epsilon) [v(\alpha, \gamma, \beta, \tau; \epsilon)]_\alpha \right.$$

$$\begin{aligned}
& + \frac{1}{j_2} v(\alpha, \gamma, \beta, \tau; \epsilon) [v(\alpha, \gamma, \beta, \tau; \epsilon)]_\gamma \\
& - \frac{1}{j_1 j_2} [u(\alpha, \gamma, \beta, \tau; \epsilon)]^2 \frac{\partial j_1}{\partial \gamma} + \frac{1}{j_1 j_2} u(\alpha, \gamma, \beta, \tau; \epsilon) v(\alpha, \gamma, \beta, \tau; \epsilon) \frac{\partial j_2}{\partial \alpha} \\
& + \frac{1}{j_2} \left\{ \pi(\alpha, \gamma, \beta, \tau; \epsilon) \right\}_\gamma - G \Big\} + w(\alpha, \gamma, \beta, \tau; \epsilon) [v(\alpha, \gamma, \beta, \tau; \epsilon)]_\beta \\
& - \left(\frac{\zeta \kappa}{j} \right)_2 v(\alpha, \gamma, \beta, \tau; \epsilon) w(\alpha, \gamma, \beta, \tau; \epsilon) = 0 \tag{2.31}
\end{aligned}$$

$$\begin{aligned}
\epsilon \Big\{ & [w(\alpha, \gamma, \beta, \tau; \epsilon)]_\tau + \frac{1}{j_1} u(\alpha, \gamma, \beta, \tau; \epsilon) [w(\alpha, \gamma, \beta, \tau; \epsilon)]_\alpha \\
& + \frac{1}{j_2} v(\alpha, \gamma, \beta, \tau; \epsilon) [w(\alpha, \gamma, \beta, \tau; \epsilon)]_\gamma \\
& + \left(\frac{\zeta \kappa}{j} \right)_1 [u(\alpha, \gamma, \beta, \tau; \epsilon)]^2 + \left(\frac{\zeta \kappa}{j} \right)_2 [v(\alpha, \gamma, \beta, \tau; \epsilon)]^2 \\
& + [\pi(\alpha, \gamma, \beta, \tau; \epsilon)]_\beta - H \Big\} \\
& + w(\alpha, \gamma, \beta, \tau; \epsilon) [w(\alpha, \gamma, \beta, \tau; \epsilon)]_\beta = 0 \tag{2.32}
\end{aligned}$$

$$[w(\alpha, \gamma, \beta, \tau; \epsilon)]_\gamma - [j_2 v(\alpha, \gamma, \beta, \tau; \epsilon)]_\beta = 0 \tag{2.33}$$

$$[j_1 u(\alpha, \gamma, \beta, \tau; \epsilon)]_\beta - [w(\alpha, \gamma, \beta, \tau; \epsilon)]_\alpha = 0 \tag{2.34}$$

$$\begin{aligned}
\epsilon \Big\{ & [Y(\alpha, \gamma, \beta, \tau; \epsilon)]_\tau \\
& + \frac{1}{j_1(\alpha, \gamma, Y, \tau)} u(\alpha, \gamma, Y, \tau; \epsilon) [Y(\alpha, \gamma, \beta, \tau; \epsilon)]_\alpha \\
& + \frac{1}{j_2(\alpha, \gamma, Y, \tau)} v(\alpha, \gamma, Y, \tau; \epsilon) [Y(\alpha, \gamma, \beta, \tau; \epsilon)]_\gamma \Big\} \\
& = w(\alpha, \gamma, Y, \tau; \epsilon) \tag{2.35}
\end{aligned}$$

$$\pi(\alpha, \gamma, Y, \tau; \epsilon) = 0 \tag{2.36}$$

$$w(\alpha, \gamma, 0, \tau; \epsilon) = 0 \tag{2.37}$$

Perturbation equations are developed by collecting terms of identical order in ϵ . Thus, these equations reflect the relative significance of the flow shallowness. Beginning with the lowest order effect (ϵ^0), the continuity equation in conjunction with the channel bed boundary condition imply that

$$w^{(0)} \equiv 0 \quad (2.38)$$

The irrotationality conditions yield the relationship between the flow velocities $u^{(0)}$, $v^{(0)}$ and depth

$$v^{(0)} = \frac{(\hat{v}\zeta_2)}{j_2} \quad (2.39)$$

$$u^{(0)} = \frac{(\hat{u}\zeta_1)}{j_1} \quad (2.40)$$

where,

$$\hat{v} \equiv v^{(0)}(\alpha, \gamma, 0, \tau) \quad (2.41)$$

$$\hat{u} \equiv u^{(0)}(\alpha, \gamma, 0, \tau) \quad (2.42)$$

Now consider the first-order perturbation effect. We obtain the continuity equation contribution

$$(j_2 u^{(0)})_\alpha + (j_1 v^{(0)})_\gamma + (j_1 j_2 w^{(1)})_\beta = 0$$

Note that this can then be integrated with respect to β over the depth to yield:

$$\begin{aligned} w^{(1)}(Y) = \frac{1}{j_1(Y)j_2(Y)} & \left[-\frac{\partial}{\partial \alpha} \left[\frac{\hat{u}\zeta_2}{\kappa_1} \left\{ \left(\frac{\kappa_2 - \kappa_1}{\kappa_1} \right) \log(f_1(Y)) + \kappa_2 Y^{(0)} \right\} \right] \right. \\ & - \frac{\partial}{\partial \gamma} \left[\frac{\hat{v}\zeta_1}{\kappa_2} \left\{ \left(\frac{\kappa_1 - \kappa_2}{\kappa_2} \right) \log(f_2(Y)) + \kappa_1 Y^{(0)} \right\} \right] \\ & \left. + \hat{u} \frac{j_2(Y)}{f_1(Y)} Y_\alpha^{(0)} + \hat{v} \frac{j_1(Y)}{f_2(Y)} Y_\gamma^{(0)} \right] \quad (2.43) \end{aligned}$$

where,

$$f_1(Y^{(0)}) \equiv 1 - \kappa_1 Y^{(0)}$$

$$f_2(Y^{(0)}) \equiv 1 - \kappa_2 Y^{(0)}$$

Substituting in the free-surface equation resulting from the terms of order ϵ we obtain

$$\begin{aligned} & j_1(Y) j_2(Y) Y_\tau^{(0)} \\ & + \frac{\partial}{\partial \alpha} \left[\hat{u} \frac{\zeta_2}{\kappa_1} \left\{ \left(\frac{\kappa_2 - \kappa_1}{\kappa_1} \right) \log(f_1(Y^{(0)})) + \kappa_2 Y^{(0)} \right\} \right] \\ & + \frac{\partial}{\partial \gamma} \left[\hat{v} \frac{\zeta_1}{\kappa_2} \left\{ \left(\frac{\kappa_1 - \kappa_2}{\kappa_2} \right) \log(f_2(Y^{(0)})) + \kappa_1 Y^{(0)} \right\} \right] = 0 \quad (2.44) \end{aligned}$$

Now, the momentum equation for the normal direction when integrated with respect to β yields the zero-order perturbation pressure contribution,

$$\begin{aligned} \pi^{(0)}(\beta) = & \frac{1}{2} \left\{ \hat{u}^2 \left((f_1(Y^{(0)}))^{-2} - (f_1(\beta))^{-2} \right) \right. \\ & \left. + \hat{v}^2 \left((f_2(Y^{(0)}))^{-2} - (f_2(\beta))^{-2} \right) \right\} + H \{ Y^{(0)} - \beta \} \quad (2.45) \end{aligned}$$

The terms within the first set of braces are the contribution to the pressure from the curvature "centrifugal" effect and the second set is simply the hydrostatic component. The momentum equation in the α direction can be simplified by the realization that $u_\beta^{(0)} - \left(\frac{\zeta_2}{j} \right)_1 u^{(0)} = 0$ due to (2.40). This implies then,

$$u_\tau^{(0)} + \frac{u^{(0)} u_\alpha^{(0)}}{j_1} + \frac{v^{(0)} u_\gamma^{(0)}}{j_2} - \frac{(v^{(0)})^2}{j_1 j_2} \frac{\partial j_2}{\partial \alpha} + \frac{u^{(0)} v^{(0)}}{j_1 j_2} \frac{\partial j_1}{\partial \gamma} + \frac{\pi_\alpha^{(0)}}{j_1} - F = 0 \quad (2.46)$$

and similarly for the γ momentum equation,

$$v_\tau^{(0)} + \frac{u^{(0)} v_\alpha^{(0)}}{j_1} + \frac{v^{(0)} v_\gamma^{(0)}}{j_2} - \frac{(u^{(0)})^2}{j_1 j_2} \frac{\partial j_1}{\partial \gamma} + \frac{u^{(0)} v^{(0)}}{j_1 j_2} \frac{\partial j_2}{\partial \alpha} + \frac{\pi_\gamma^{(0)}}{j_2} - G = 0 \quad (2.47)$$

2.3 Generalized Shallow Water Equations

We now transform back to dimensional form and drop the perturbation index for convenience and find the equations given below. The mass conservation equation is derived from equation (2.44), the momentum equations from equations (2.46 and 2.47), the pressure from equation (2.45), and the vertical velocity from equation (2.43).

$$j_1(h)j_2(h)h_t + \frac{\partial}{\partial s_1} \left[\hat{u} \frac{\zeta_2}{\kappa_1} \left\{ \left(\frac{\kappa_2 - \kappa_1}{\kappa_1} \right) \log(1 - \kappa_1 h) + \kappa_2 h \right\} \right] \\ + \frac{\partial}{\partial s_2} \left[\hat{v} \frac{\zeta_1}{\kappa_2} \left\{ \left(\frac{\kappa_1 - \kappa_2}{\kappa_2} \right) \log(1 - \kappa_2 h) + \kappa_1 h \right\} \right] = 0 \quad (2.48)$$

$$u_t + \frac{u}{j_1} u_{s_1} + \frac{v}{j_2} u_{s_2} - \frac{v^2}{j_1 j_2} \frac{\partial j_2}{\partial s_1} + \frac{uv}{j_1 j_2} \frac{\partial j_1}{\partial s_2} + \frac{1}{j_1 \rho} P_{s_1} - g_1 = 0 \quad (2.49)$$

$$v_t + \frac{u}{j_1} v_{s_1} + \frac{v}{j_2} v_{s_2} - \frac{u^2}{j_1 j_2} \frac{\partial j_1}{\partial s_2} + \frac{uv}{j_1 j_2} \frac{\partial j_2}{\partial s_1} + \frac{1}{j_2 \rho} P_{s_2} - g_2 = 0 \quad (2.50)$$

$$w(s_3) = -\frac{1}{j_1 j_2} \left[\frac{\partial}{\partial s_1} \left\{ \frac{\hat{u} \zeta_2}{\kappa_1} \left(\left(\frac{\kappa_2 - \kappa_1}{\kappa_1} \right) \log(1 - \kappa_1 s_3) + \kappa_2 s_3 \right) \right\} \right. \\ \left. + \frac{\partial}{\partial s_2} \left\{ \frac{\hat{v} \zeta_1}{\kappa_2} \left(\left(\frac{\kappa_1 - \kappa_2}{\kappa_2} \right) \log(1 - \kappa_2 s_3) + \kappa_1 s_3 \right) \right\} \right] \quad (2.51)$$

$$P(s_3) = \frac{\rho}{2} \left[\hat{u}^2 \left\{ \left(\frac{1}{1 - \kappa_1 h} \right)^2 - \left(\frac{1}{1 - \kappa_1 s_3} \right)^2 \right\} \right. \\ \left. + \hat{v}^2 \left\{ \left(\frac{1}{1 - \kappa_2 h} \right)^2 - \left(\frac{1}{1 - \kappa_2 s_3} \right)^2 \right\} \right] + \rho g_3 (h - s_3) \quad (2.52)$$

$$u(s_3) = \frac{\hat{u}}{1 - \kappa_1 s_3} \quad (2.53)$$

$$v(s_3) = \frac{\hat{v}}{1 - \kappa_2 s_3} \quad (2.54)$$

$$j_1 = \zeta_1 (1 - \kappa_1 s_3) \quad (2.55)$$

$$j_2 = \zeta_2 (1 - \kappa_2 s_3) \quad (2.56)$$

$$j_1(h) = \zeta_1(1 - \kappa_1 h) \quad (2.57)$$

$$j_2(h) = \zeta_2(1 - \kappa_2 h) \quad (2.58)$$

This system of equations can be used to solve for h , u , v , and P and, from this information, w .

These equations represent the zero-order approximation for h , u , and v ; and as such are only accurate when the flow is shallow relative to longitudinal and lateral features. This means that the water surface reasonably parallels the bed. This is true of all shallow water equations. The bed-normal velocity (equation 2.52) is the first-order representation of w , (the zero-order is that the bed normal velocity is identically zero). This is the condition reflected in the solutions of h , u , and v . The first-order approximation for w results from inferences drawn using the mass conservation equation. Its effects are not "felt" in these shallow water equations. Higher-order expansion terms would be necessary. It is important to keep in mind the limitations on these generalized shallow water equations.

Chapter 3

One-Dimensional Problem and Exploratory Studies

3.1 Introduction

Shallow water theory has been extensively studied both analytically and numerically for a wide class of *free-surface flows*. However, there have been relatively fewer shallow water studies of *free-surface flows* over curved beds such as those encountered in spillway designs. The curved bed case presents certain difficulties both analytically and numerically when compared with the flows usually encountered in shallow water calculations, since the pressure distribution is now decidedly not hydrostatic. As an example, in flow over a spillway, the bed curvature produces an inertial acceleration and thereby an apparent force which is comparable in size to the hydrostatic pressure. The spillway capacity therefore is strongly influenced by these curvature effects. In this chapter we first study the properties of the one-dimensional problem and develop a corresponding finite element treatment. The associated numerical studies permit a preliminary study of the overall approach. This in turn is used to guide the development of the final two-dimensional model and analysis in the following chapters.

The main thrust of the present study is directed towards analysis and finite element approximation of this problem, including the influence of the curved bed. The analysis extends the approach of Dressler [20] by means of

a perturbation analysis leading to a new formulation of the problem (recall Chapter 2) and a generalized set of shallow water equations which includes bed curvature effects. In the limit of zero curvature the classical shallow water equations are recovered. The problem is complicated by the fact that there are possible transitions between subcritical and supercritical flows depending upon the local Froude number [27]. A further issue arises in the representation of the hydraulic jump which forms near the base of the spillway. This hydraulic jump enters as a discontinuity in the solution of the mathematical problem.

As with standard shallow water theory, certain simplifying assumptions also arise here implicitly from the perturbation analysis and the neglect of higher-order terms. The primary one is that accelerations normal to the bed are nonexistent and thus the dispersive character of shorter wavelengths (in which wave speed depends upon wavelength) will not be represented. The resulting flow variables can only comprehend longer wavelengths in which wave speed depends upon water depth and, in this particular set of equations, bed curvature. The overall features of the hydraulic jump can be captured as weak solutions containing a discontinuity. However, once again, vertical accelerations and short period waves are not produced. A discussion of the equations and details of the jump representation are included in Sections 3.2 and 3.3.

In the present treatment, an approximate formulation based on finite elements (Section 3.4) is constructed for the dominant perturbation terms in the solution to the curved bed problem. To accommodate the wave-like behavior and produce a stable method, a special artificial viscosity formulation is employed. This form is motivated by the eigenvalue properties of the system and the existence of subcritical and supercritical regions. The resulting scheme

introduces numerical dissipation in the discrete model. Partly as a consequence of this, the hydraulic jump is approximated over several elements but still does yield good agreement. Numerical experiments are conducted for a representative problem corresponding to shallow water flow over a "bump" (Section 3.5).

3.2 One-Dimensional Equations

The perturbation analysis implies for mass conservation (by depth integration of (2.49))

$$\frac{\partial h}{\partial t} - \frac{1}{j(h)} \frac{\partial}{\partial s} \left\{ \frac{p \log j(h)}{\kappa h} \right\} = 0 \quad (3.1)$$

and for conservation of momentum (depth-integrated (2.50))

$$\begin{aligned} \frac{\partial p}{\partial t} + \frac{\partial}{\partial s} \left\{ \frac{p^2}{hj(h)} + \frac{1}{2} \kappa \left[\frac{p}{j(h)} \right]^2 + \frac{1}{2} gh^2 \cos \theta \right\} \\ - \int_0^h \kappa u w ds_3 + j(h/2)gh \sin \theta + \frac{gn^2 |p| p}{C j(h/2) h^{7/3}} = 0 \end{aligned} \quad (3.2)$$

where the Manning equation is utilized to account for friction and turbulence losses. Here, for notational convenience, we have set j for j_1 and s for s_1 with $p = \hat{u}h$ where \hat{u} is the velocity at the bed surface, $s_3 = 0$. Further, θ is the angle between the bed and the horizontal direction (see Figure 1.2), n is Manning's bed friction coefficient, and C is a conversion factor needed since n is not dimensionless, (1.0 for metric units and 2.21 for English units).

Solution variables u and w now denote the zero-order and first-order perturbation contributions for the tangential and normal velocity components, respectively (the term w arises in the depth integration and can be written

in terms of zero-order h and u , this is simply a convenience). The integral in equation (3.2) can be evaluated directly by substituting the known relationship for u over depth and including the relationship (2.52) for the first-order contribution to w . We have

$$\int_0^h \kappa u w ds_3 = \left\{ \frac{\log j(h) + \kappa h}{\kappa j(h)} \right\} \left\{ \frac{p}{h^2} \frac{\partial p}{\partial s} - \frac{1}{\kappa} \frac{p^2}{h^2} \frac{\partial \kappa}{\partial s} \right\} - \frac{1}{2} \left[\frac{p}{j(h)} \right] \frac{\partial \kappa}{\partial s} \quad (3.3)$$

Since

$$\lim_{\kappa \rightarrow 0} \left\{ \frac{\log j(h)}{\kappa} \right\} = -h \quad (3.4)$$

$$\lim_{\kappa \rightarrow 0} \left\{ \frac{\log j(h) + \kappa h}{\kappa j(h)} \right\} = 0 \quad (3.5)$$

$$\lim_{\kappa \rightarrow 0} \frac{1}{\kappa} \left\{ \frac{\log j(h) + \kappa h}{\kappa h} \right\} = -\frac{1}{2}h \quad (3.6)$$

it follows that the terms involving curvature κ in the denominator of (3.3) must remain bounded in the limit as κ approaches zero.

3.3 Discussion

Observe that the pressure force is represented in equation (3.2) by

$$\frac{1}{2} \kappa \left[\frac{p}{j(h)} \right]^2 + \frac{1}{2} g h^2 \cos \theta$$

where the first term can be associated with the centrifugal effects and the second is due to the hydrostatic pressure. Thus the pressure distribution is indeed not hydrostatic.

Also note that if $\kappa = 0$, these flow perturbation equations (3.1) and (3.2) reduce to

$$\frac{\partial h}{\partial t} + \frac{\partial p}{\partial s} = 0 \quad (3.7)$$

$$\frac{\partial p}{\partial t} + \frac{\partial}{\partial s} \left\{ \frac{p^2}{h} + \frac{1}{2}gh^2 \cos \theta \right\} + gh \sin \theta + \frac{gn^2|p|p}{Ch^{7/3}} = 0 \quad (3.8)$$

which correspond to the shallow water equations in conservation form for the case where the channel slope is significant. If channel slope is not significant we recover the classical shallow water equations.

The characteristic differential equations for the hyperbolic system (3.1)–(3.2) are

$$\frac{ds}{dt} = \frac{\hat{u}}{[j(h)]^2} \pm D^{1/2} \quad (3.9)$$

with

$$D = -\frac{\log j(h)}{j(h)\kappa} \left(g \cos \theta + \frac{\kappa}{[j(h)]^3} \hat{u}^2 \right)$$

This implies that in this model wavespeed is independent of wavelength. That is, all wavelengths travel at the same speed, which depends on the depth, gravitational and centripetal acceleration. A region of flow is considered subcritical if $D^{1/2} < \frac{\hat{u}}{[j(h)]^2}$, and if $D^{1/2} > \frac{\hat{u}}{[j(h)]^2}$ it is supercritical. The set of equations describes flow in these regimes. However, the transition from supercritical to subcritical must occur through a hydraulic jump. This may be mathematically characterized by a weak solution of (3.1)–(3.2) containing a discontinuity. The flow variables will not allow the production of vertical acceleration and short period waves associated with a jump, but the overall flow features can be preserved.

The equations developed here model the total momentum flux through a cross-section whereas Dressler considers momentum flux per unit depth. In one dimension his approach corresponds to conserving mechanical energy. However, in reality steep gradients in water surface elevation arise in the form of

hydraulic jumps where (physically) mechanical energy is transformed to other forms of energy through flow turbulence, generation of short-waves, etc. [1]; this is apparent in Figure 1.1. Hence energy will not be conserved but momentum is conserved. In the mathematical treatment of the hydraulic jump the downstream (tailwater) elevation is prescribed and the preceding observations then imply that the differences in the present formulation to that of Dressler would be manifest through the location of the hydraulic jump. The new model should predict a hydraulic jump location that is closer to the physical situation. Since the hydraulic jump is an important feature of the flow from the standpoint of the engineering design problem, this distinction is important.

Introducing the weighted residual projection in (3.1) and (3.2) against test function ϕ and integrating by parts with respect to s , we obtain

$$\int_{\Omega} \left(j(h) \frac{\partial h}{\partial t} \phi + q \frac{\partial \phi}{\partial s} \right) ds - q \phi |_{\partial \Omega} = 0 \quad (3.10)$$

and

$$\int_{\Omega} \left(\frac{\partial p}{\partial t} \phi - r \frac{\partial \phi}{\partial s} + f(s, t, h, p) \phi - \phi \int_0^h \kappa u w ds_3 \right) ds + r \phi |_{\partial \Omega} = 0 \quad (3.11)$$

where Ω is the domain, $\partial \Omega$ is the boundary of Ω , and

$$\begin{aligned} q &= \frac{p \log j(h)}{\kappa h} \\ r &= \frac{p^2}{h j(h)} + \frac{1}{2} \kappa \left[\frac{p}{j(h)} \right]^2 + \frac{1}{2} g h^2 \cos \theta \\ f &= j \left(\frac{h}{2} \right) g h \sin \theta + \frac{g n^2 |p| p}{C j \left(\frac{h}{2} \right) h^{7/3}} \end{aligned} \quad (3.12)$$

The weak form of the transient problem (3.10) - (3.11) admits discontinuous solutions that model the actual hydraulic jump when the shallow water flow

encounters the deeper water in the "stilling basin" downstream. Mathematically this discontinuity arises from the "hard" downstream condition where the tailwater elevation is specified. Thus the solution to the weak problem may have a jump discontinuity in p and in h .

Since we are primarily interested in the steady flow situation, let us consider the steady form of (3.10) - (3.11) for an arbitrarily small region R containing discontinuity point \bar{s} with test function ϕ zero on the boundary of R and outside R . Then, for conservation of mass (3.10) implies, in the limit as $R \rightarrow 0$, $[q] = 0$ (where $[q]$ denotes the jump in mass flux q at \bar{s}). That is, mass is conserved through the hydraulic jump. For the transient problem a similar treatment applying the divergence theorem in (s, t) yields the relation $-j(h)[h]\frac{ds}{dt} = [q]$ for the speed of propagation of the discontinuity.

In the case of zero curvature, $\kappa \equiv 0$, the governing perturbation equations reduce to the familiar shallow water equations. A similar analysis to that given above can then be applied to the momentum equation to yield $[r] = 0$ for the steady-state problem and $[p]\frac{ds}{dt} = [r]$ for the transient problem. When $\kappa \neq 0$, the presence of the term $\int_0^h \kappa u w ds_3$ in (3.11) now provides a non-zero contribution for $[r]$ at \bar{s} . In typical spillway applications, the bed is curved but the hydraulic jump occurs downstream in a region of zero curvature.

3.4 Finite Element Approximation

3.4.1 Choice of Basis

Next, we consider approximate analysis of the weak statements in (3.10) and (3.11) on a discretization of finite elements. The underlying contin-

uous problem is comprised of a first-order hyperbolic system in elevation and velocity variables. Discretization may give rise to spurious oscillatory modes in the shallow water problem. The presence and nature of spurious modes of wavelength $2\Delta s$, where Δs is the mesh spacing, has been investigated previously [46, 59]. It has been shown for the linearized shallow water equations that piecewise-linear approximation of u with piecewise constant h does not generate an oscillatory mode. However, in the present analysis, the curvature terms preclude a piecewise-constant basis. A piecewise-quadratic basis for velocity with piecewise-linears for depth would be a logical choice but contain an oscillatory mode for velocity (not for depth). The nonlinear terms in many applications of the shallow water equations for rivers and estuaries are quite small. In our problem, however, the velocities are large and the gradients steep. Thus the nonlinearities are very important and selecting the basis to exclude spurious modes for the linear equations does not ensure oscillations will not be generated by the nonlinear convective terms.

The discontinuities in h and p at the hydraulic jump could be represented exactly by means of a discontinuous finite element basis. In a non-dissipative formulation with standard elements "Gibbs type" oscillations will be generated at the jump. However, dissipation is present in the physical problem and, as noted previously, this effect is significant in the neighborhood of the hydraulic jump. Accordingly, it is common practice to include an artificial dissipation in the governing equations or a numerical dissipation arising from the discretization method. This added dissipation is active at the hydraulic jump and effectively "smears" the jump over a few mesh intervals. The higher order dissipative term then implies that the upstream and downstream

boundary conditions can now be consistently treated and the solution h, p to the dissipative equations is continuous. In turn, this implies that we can use standard C° Lagrange basis functions in the finite element analysis.

3.4.2 Artificial Dissipation

The form for artificial dissipation was constructed based on one-dimensional convection diffusion models and such that, throughout the supercritical reach, the coefficient closely matches the analytic wavespeed. Accordingly, we add to (3.1) - (3.2) the dissipative operator

$$\frac{\partial}{\partial s} \left(\frac{\alpha |\hat{u}|}{[j(h)]^2} \frac{\partial}{\partial s} \right) \quad (3.13)$$

where $\alpha = \beta j(h) \Delta s$ in (3.1) and $\alpha = \beta \Delta s$ in (3.2), and β is a weighting parameter. Adding the dissipative term (3.13) to the perturbation equations (3.1), (3.2) and integrating by parts in the weighted residual condition the additional integrals in the weak statement (3.10) - (3.11) are, respectively,

$$\int_{\Omega} \left(\beta \Delta s \frac{|\hat{u}|}{[j(h)]} \frac{\partial h}{\partial s} \frac{\partial w}{\partial s} \right) ds - \beta \Delta s \frac{|\hat{u}|}{j(h)} \frac{\partial h}{\partial s} w |_{\partial \Omega}$$

and

$$\int_{\Omega} \beta \Delta s \frac{|\hat{u}|}{[j(h)]^2} \frac{\partial p}{\partial s} \frac{\partial w}{\partial s} ds - \beta \Delta s \frac{|\hat{u}|}{[j(h)]^2} \frac{\partial p}{\partial s} w |_{\partial \Omega} \quad (3.14)$$

This choice of dissipation is motivated by an analysis of the corresponding hyperbolic system for the one-dimensional spillway problem. The characteristic differential equations for the hyperbolic system (3.1) - (3.2) describing the one-dimensional spillway problem are given by (3.9). The characteristic coordinates are obtained as the two families of solutions $\xi(s, t) =$

constant and $\eta(s, t) = \text{constant}$ of these characteristic equations. In the special case of $\kappa = 0$ the linearized shallow water equations are obtained and the characteristic differential equations (3.9) reduce to

$$\frac{ds}{dt} = u_0 \pm \sqrt{gh_0} \quad (3.15)$$

The governing wave equation simplifies in the characteristic frame and, in the linear case (3.15), disturbances propagate unchanged along the respective straight-line characteristics. For the nonlinear problem of interest here the characteristics are curved. When characteristics of the same family intersect to form a caustic, discontinuities may be generated in the solution. This is precisely the situation in the present case: for supercritical flow "positive" characteristics intersect and the difference between the upstream disturbance (which is being convected downstream) and the downstream boundary condition is resolved through the hydraulic jump. That is, the specified tailwater in the stilling basin forces subcritical conditions downstream while supercritical flow exists upstream, and the hydraulic jump is formed as a result of this interaction.

If dissipation is introduced in the mathematical model, then the equations are second-order and change type. The upstream and downstream conditions then can be accommodated by a smooth solution to the governing (modified) equation. The result of adding moderate local dissipation is that numerical oscillations are suppressed in the subsequent approximate solution but the sharp jump is less well resolved. If the local dissipation is small there will be only slight "smearing". This dissipative behavior is, at least qualitatively, consistent with the real physical process. This issue notwithstanding, there are

several other difficulties that arise when the discrete model is considered. Of course, the discrete representation should reflect the qualitative behavior of the continuous mathematical problem. Moreover, the approximate solution should converge in the appropriate norms as mesh size and time step are reduced. Our concern here is to have realistic model results, even near the hydraulic jump where the effect of the "hard" downstream boundary condition tends to promote oscillations and spurious "modes".

To demonstrate the nature of the problem, let us turn to the frequently studied steady convection-diffusion problem. We intend to clarify the questions related to modes and oscillations associated with conflicting end conditions, such as those for the hydraulic jump in the spillway problem. The model equation is

$$u_0 \frac{dc}{ds} - \epsilon \frac{d^2c}{ds^2} = 0 \quad 0 < s < 1 \quad (3.16)$$

with $c(0) = 0$ and $c(1) = 1$. Here ϵ represents an artificial diffusivity with $0 < \epsilon \ll 1$. The solution to (3.16) is essentially zero in the upstream region and rises abruptly through a boundary layer to satisfy $c = 1$ at the downstream end.

Introducing a standard Galerkin finite element method with linear elements (or equivalently using central differencing), at interior node i we have

$$u_0 \left(\frac{c_{i+1} - c_{i-1}}{2\Delta s} \right) - \frac{\epsilon}{(\Delta s)^2} (c_{i+1} - 2c_i + c_{i-1}) = 0 \quad (3.17)$$

For the degenerate limiting case $\epsilon \rightarrow 0$ the differential equation (3.16) reduces to $dc/dx = 0$ so $c = \text{constant}$ is the solution. In the present case we have $c = 0$ if the left condition is to be satisfied and $c = 1$ if the right end condition is

chosen. This degenerate form of (3.16) is of lower order and clearly is over-specified. The corresponding degenerate form of the non-dissipative discrete problem (3.17) with $\epsilon = 0$ presents an entirely different situation. We then have simply $c_{i+1} - c_{i-1} = 0$. Setting $c_i = \rho^i$, the solution to this second order difference equation satisfies $\rho^{i+1} - \rho^{i-1} = 0$, that is, $\rho = \pm 1$. Hence the general solution to the discrete problem is $c_i = A + B(-1)^i$ where constants A, B are determined from the boundary conditions. If $B = 0$ then the discrete model corresponds to the first order continuous problem and A is given by the end conditions. Even if B is small, however, there will be a superposed inter-node oscillation of amplitude B . This internode oscillation of wavelength $2\Delta s$ then represents a spurious mode resulting from the second-order approximation of the first order operator. The amplitude B of the oscillation will evidently depend upon the "inconsistency" of the boundary conditions. In the present case, if $c(0) = c(1)$ then B is zero and the oscillation will not be forced; for $c(0) = 0, c(1) = 1$ we see that there is an oscillation of unit amplitude forced in the numerical solution.

Addition of artificial dissipation returns the forms in (3.16) and (3.17) with $\epsilon \neq 0$ and a standard Fourier analysis reveals that oscillations can be eliminated provided

$$\epsilon \geq \frac{1}{2}u_0\Delta s \quad , \quad u_0 > 0 \quad (3.18)$$

which yields the familiar cell Reynolds or Peclet condition.

The particular choice of artificial dissipation employed in the present work can be motivated or interpreted physically as follows. First note that the coefficient of the artificial viscosity is specified in (3.13) as the net transport

rate $\hat{u}/[j(h)]^2$. This reduces to u_0 for the standard shallow water equations which then become

$$\begin{aligned} \frac{\partial h}{\partial t} + \frac{\partial p}{\partial s} &= \alpha u_0 \frac{\partial^2 h}{\partial s^2} \\ \frac{\partial p}{\partial t} + (gh_0 - u_0^2) \frac{\partial h}{\partial s} + 2u_0 \frac{\partial p}{\partial s} &= \alpha u_0 \frac{\partial^2 p}{\partial s^2} \end{aligned} \quad (3.19)$$

Introducing a finite element approximation with a linear basis the roots of the "indicial" equation for the discrete difference form are

$$\rho = 1, \left\{ \frac{1 + \frac{\Delta s}{2} \left[\frac{u_0 - \sqrt{gh_0}}{\alpha u_0} \right]}{1 - \frac{\Delta s}{2} \left[\frac{u_0 - \sqrt{gh_0}}{\alpha u_0} \right]} \right\}, \left\{ \frac{1 + \frac{\Delta s}{2} \left[\frac{u_0 + \sqrt{gh_0}}{\alpha u_0} \right]}{1 - \frac{\Delta s}{2} \left[\frac{u_0 + \sqrt{gh_0}}{\alpha u_0} \right]} \right\} \quad (3.20)$$

All of these roots will remain positive if

$$\frac{\alpha}{\Delta s} \geq \frac{1}{2} \left(\frac{u_0 + \sqrt{gh_0}}{u_0} \right) \quad (3.21)$$

and numerical oscillations excited by the hydraulic jump will be damped. Moreover, if we choose α to be proportional to Δs , this condition will remain enforced as the mesh size Δs is reduced. The artificial dissipation will be reduced proportionally with Δs and the resolution of the jump will improve. Since the jump is a major source of oscillation, the local damping will improve the global behavior of the approximate solution.

While this analysis has focused upon the linear case, the nonlinear terms can also cause internode oscillations. Aliasing into lower wavelengths from these internode oscillations will also occur. Since the artificial diffusion terms will preferentially damp short wavelength oscillations the nonlinear induced oscillations should be moderated by this mechanism.

3.4.3 Finite Element Approximation

Introducing finite element expansions for h and p in the weak statements then yields the discretized equations

$$\begin{aligned} & \sum_e \int_{\Omega_e} \left\{ \frac{\phi_i j(\bar{h}^m) \sum_j \phi_j [\bar{h}_j^{m+1} - \bar{h}_j^m]}{\Delta t} + \frac{d\phi_i}{ds} \left[\frac{\log j(\bar{h}^m)}{\kappa(s) \sum_j \phi_j \bar{h}_j^m} \sum_k \phi_k \bar{p}_k^{m+1} \right] \right. \\ & \left. + \beta \Delta s \frac{|\hat{u}^m|}{j(\bar{h}^m)} \frac{d\phi_i}{ds} \sum_j \frac{d\phi_j}{ds} \bar{h}_j^{m+1} \right\} ds \\ & + \left[-\phi_i \frac{\log j(\bar{h}^m)}{\kappa(s) \sum_j \phi_j \bar{h}_j^m} \sum_k \phi_k \bar{p}_k^{m+1} - \phi_i \beta \Delta s \frac{|\hat{u}^m|}{j(\bar{h}^m)} \sum_j \frac{d\phi_j}{ds} \bar{h}_j^{m+1} \right] \Big|_{\partial\Omega_e \cap \partial\Omega} = 0 \end{aligned}$$

for the continuity equation, and

$$\begin{aligned} & \sum_e \int_{\Omega_e} \left\{ \phi_i \sum_j \phi_j [\bar{p}_j^{m+1} - \bar{p}_j^m] / \Delta t - \frac{d\phi_i}{ds} \left[\frac{\sum_j \phi_j \bar{p}_j^m}{j(\bar{h}^m) \sum_k \phi_k \bar{h}_k^m} \sum_\ell \phi_\ell \bar{p}_\ell^{m+1} \right] \right. \\ & \left. + \frac{\kappa(s)}{2[j(\bar{h}^m)]^2} \sum_j \phi_j \bar{p}_j^m \sum_k \phi_k \bar{p}_k^{m+1} + \frac{1}{2} g \cos(\theta(s)) \sum_j \phi_j \bar{h}_j^m \sum_k \phi_k \bar{h}_k^{m+1} \right\} \\ & + \beta \Delta s \frac{|\hat{u}^m|}{[j(\bar{h}^m)]^2} \frac{d\phi_i}{ds} \sum_j \frac{d\phi_j}{ds} \bar{p}_j^{m+1} + Q_1 + Q_2 + Q_3 \Big\} ds \\ & + \phi_i \left[\frac{\sum_j \phi_j \bar{p}_j^m}{j(\bar{h}^m) \sum_k \phi_k \bar{h}_k^m} \sum_\ell \phi_\ell \bar{p}_\ell^{m+1} + \frac{\kappa(s)}{2[j(\bar{h}^m)]^2} \sum_j \phi_j \bar{p}_j^m \sum_k \phi_k \bar{p}_k^{m+1} \right. \\ & \left. + \frac{1}{2} g \cos(\theta(s)) \sum_j \phi_j \bar{h}_j^m \sum_k \phi_k \bar{h}_k^{m+1} - \beta \Delta s \frac{|\hat{u}^m|}{[j(\bar{h}^m)]^2} \sum_j \frac{d\phi_j}{ds} \bar{p}_j^{m+1} \right] \Big|_{\partial\Omega_e \cap \partial\Omega} = 0 \end{aligned}$$

for the momentum equation, where

$$Q_1 = \phi_i \left\{ \frac{\log j(\bar{h}^m) + \kappa(s) \sum_j \phi_j \bar{h}_j^m}{\kappa(s) j(\bar{h}^m)} \right\}$$

$$\begin{aligned}
& \left\{ \frac{\sum_j \phi_j \bar{p}_j^m}{\left[\sum_k \phi_k \bar{h}_k^m \right]^2} \sum_\ell \frac{d\phi_\ell}{ds} \bar{p}_\ell^{m+1} - \frac{d\kappa(s)}{ds} \left[\frac{1}{\kappa(s)} \frac{\sum_j \phi_j \bar{p}_j^m}{\left[\sum_k \phi_k \bar{h}_k^m \right]^2} \right] \sum_\ell \phi_\ell \bar{p}_\ell^{m+1} \right\} \\
& - \frac{\phi_i}{2j(\bar{h}^m)} \frac{d\kappa(s)}{ds} \sum_\kappa \phi_\kappa \bar{F}_\kappa^{m+1} \\
Q_2 &= \phi_i \left\{ j(\bar{h}^m/2)g \sin(\theta(s)) \sum_j \phi_j \bar{h}_j^{m+1} \right\} \\
Q_3 &= \phi_i \frac{gn^2 \left| \sum_j \phi_j \bar{p}_j^m \right|}{Cj(\bar{h}^m/2) \left[\sum_k \phi_k \bar{h}_k^m \right]^{7/3}} \sum_\ell \phi_\ell \bar{p}_\ell^{m+1} \\
j(\bar{h}^m) &= 1 - \kappa(s) \sum_j \phi_j \bar{h}_j^m \\
j(\bar{h}^m/2) &= 1 - \frac{1}{2} \kappa(s) \sum_j \phi_j \bar{h}_j^m
\end{aligned}$$

3.5 Model Results

Model simulations were conducted using bed topography from the numerical and flume studies of Sivakumaran [51]. This bed form is given by $Z = .20e^{[-\frac{1}{2}(\frac{x}{\bar{h}})^2]}$ where x is the horizontal distance in meters from the center of the crest and Z is the elevation in meters. That is, this spillway bed geometry has the form of a normal distribution symmetric about $x = 0$, with a crest elevation of 0.20m. In the present numerical experiments, values of discharge are specified upstream and the tailwater elevation downstream. The flow capacity of the spillway, as indicated by the upstream water surface elevation is, therefore, calculated by the approximate model as a steady-state, from which the predicted flow capacity can be compared with Sivakumaran's flume

results. The same test is repeated with the curvature-related terms removed. This yields the shallow water model (with channel steepness included), which can be used for comparison purposes to determine the effect of curvature.

One should note that the flume data of Sivakumaran does not contain a noticeable jump since the tailwater elevation is too low. However, in the present test a higher tailwater is specified to evaluate the suitability of our numerical scheme to simulate the jump and control the associated oscillations. The location of the jump can vary widely for slight changes in velocity and depth. This sensitivity is reduced in real physical flows by the presence of friction which causes a steeper water surface slope. Friction in this model is included by Manning's expression with friction factor 0.016 corrected for curvature [21]. The results of test calculations are shown in Figures 3.1 - 3.3 for flows with an upstream discharge of $0.03599\text{m}^3/\text{s}/\text{m}$ and a downstream depth (tailwater) 0.1m, using a mesh with 46 linear elements. Higher grid resolution is required upstream of the spillway crest where there are steep variations in flow variables. Along the downstream side of the spillway the depth changes gradually and fewer elements are required. The semi-discrete system is integrated numerically to a steady-state with a fixed timestep $\Delta t = 0.05$ sec using an implicit scheme.

The depth-averaged velocity is given in Figure 3.1. Both the velocity and its spatial variation are relatively small upstream of the crest which confirms that the effect of the nonlinear terms is not significant here. Downstream of the crest, the velocity is large and a small perturbation in depth imposed upon this region will develop large velocity variations to conserve mass. If dissipation is not sufficiently large, the jump excites oscillations and a nonlin-

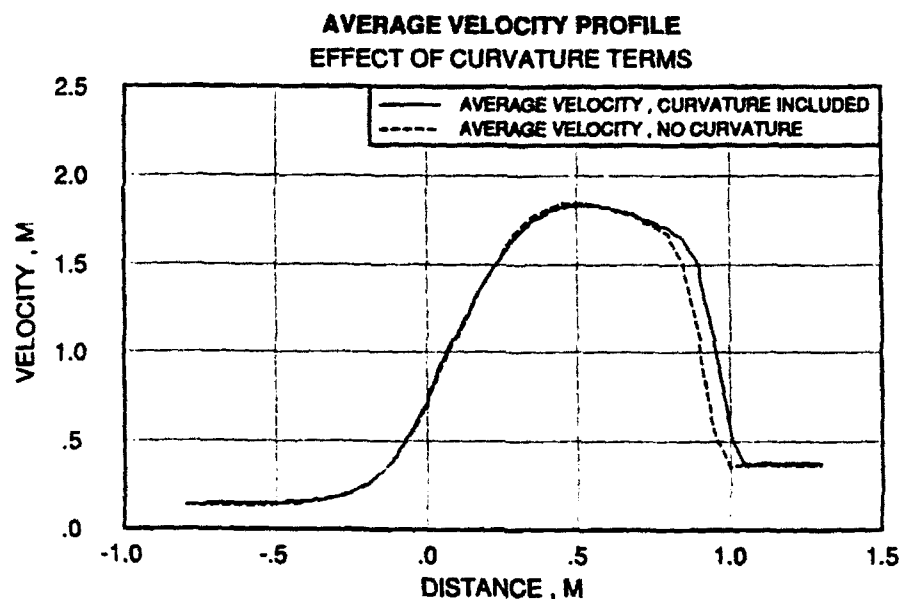


Figure 3.1: Average velocity profile — effect of curvature terms.

ear instability develops. In the calculations shown here, the coefficient β for dissipation was set at 0.5 downstream and 0.25 upstream.

The bed pressure ratio profile is shown in Figure 3.2. This is the ratio of the pressure associated with centrifugal effects to hydrostatic pressure alone. Throughout the region in which the bed is convex, $-0.24 < x < 0.24$, an uplift is evident, reaching a maximum of 0.36 a distance 0.10m downstream of the crest. In the concave portion of the downstream bed the pressure gradually increases and reaches 0.55 near the “toe” of the spillway. It is apparent that the pressure distribution is definitely not hydrostatic.

Included in Figures 3.1 and 3.3 are dashed lines indicating the model results when the curvature is set to be identically zero. This corresponds to the

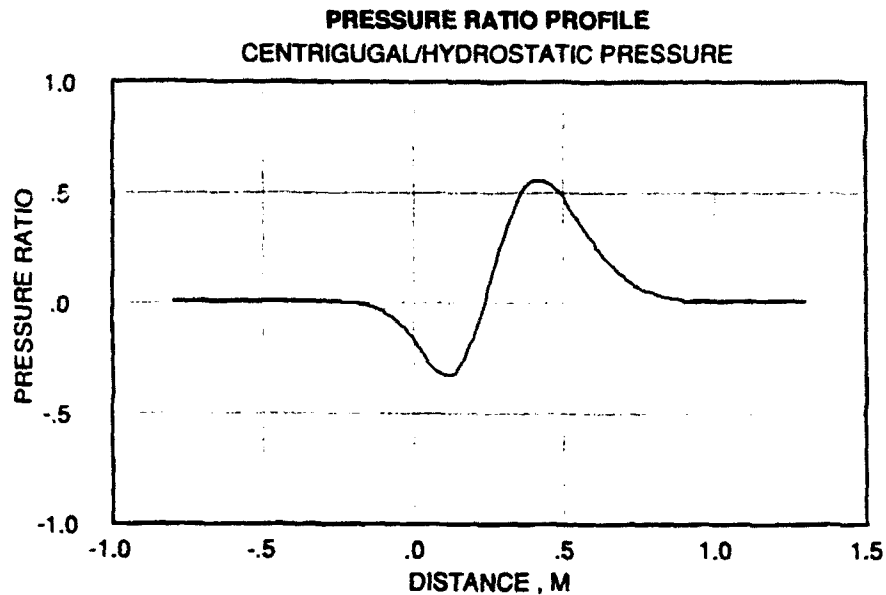


Figure 3.2: Pressure ratio profile — centrifugal/hydrostatic pressure.

standard shallow water result for a steep slope. Of particular importance is the observation that the shallow water equations predict a higher upstream water surface elevation to allow this discharge to pass over the spillway. That is, the shallow water equations predict a lower spillway capacity than the equations including curvature.

The capacity of the spillway is directly related to the energy required to pass a particular flow rate. The specific energy, defined by $E \equiv \frac{1}{2} \left(\frac{\dot{u}}{g(h)} \right)^2 + Z_{ws}$, is the mechanical energy from the Bernoulli expression referenced to the datum of the crest elevation. Here $\left(\frac{\dot{u}}{g(h)} \right)$ is the surface velocity and Z_{ws} is the water surface elevation above the crest. The specific energy indicated by the flume was 0.072m. The numerical model results were 0.083m for the steep-slope standard shallow water equation and 0.072m for the model including curvature.

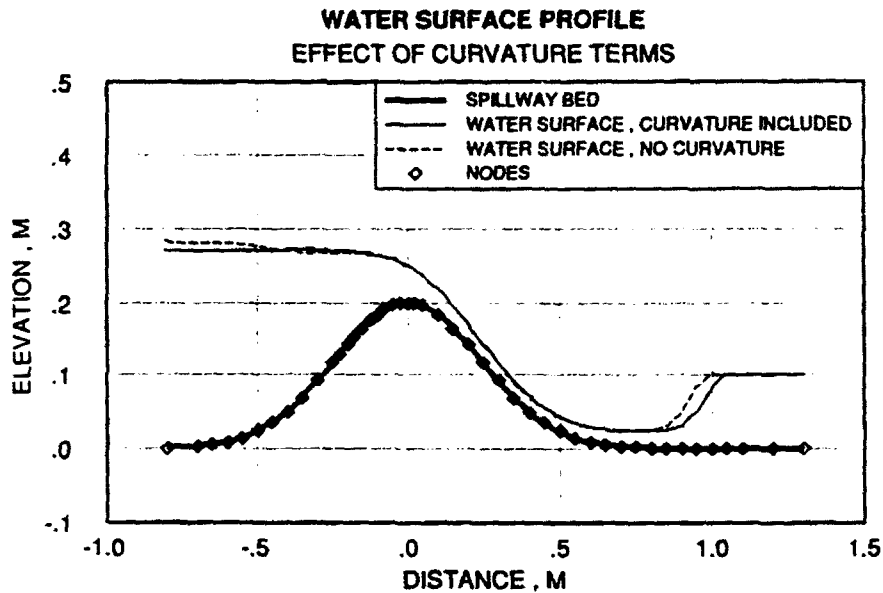


Figure 3.3: Water surface profile – effect of curvature terms.

Downstream of the crest, the calculated water surface for the shallow water equations is slightly steeper than the results with curvature included and the flow becomes progressively more shallow. This is more easily seen in the velocity plot, where excluding curvature produces velocities that are too large. In the concave region this effect is reversed and the velocity predicted by the steep-slope shallow water equation drops below that of the model with curvature effects included. More energy is needed to pass this discharge and the effective loss of energy downstream of the crest causes the predicted location of the jump to move upstream as compared to the results with curvature included.

The discrepancy in upstream results from the two models is not attributable to centrifugal effects as they are not significant. This behavior is due to the bed-normal measurement of depth. In a concave region the bed-normal

directions at the ends of differential segment converge as one moves away from the bed, so that the differential volume per unit width is smaller than would be calculated by simply multiplying the depth and length along the bed. The volume (volume per unit width) calculations will be too large in the concave regions and small in the convex regions. Thus in the concave regions the standard equations require a larger pressure variation for the flow acceleration. Downstream of the crest this effect is smaller as the depth is shallow and the water surface is nearly parallel to the bed. Here the centrifugal forces become more important. Results including curvature effects show a slightly less steep water surface slope as a result of the adverse centrifugal pressure gradient. Downstream of location 0.4m the centrifugal pressure gradient is positive, and the results with curvature included predict a flatter water surface slope. This in turn moves the jump downstream. Note that both of these model equations are written for bed-fitted coordinates. The St. Venant equations on the other hand are written for momentum and mass conservation horizontally and as such offer a much poorer comparison on the spillway section [21].

The capability of the model to treat the hydraulic jump is also revealed in these results. The effect of mesh refinement is examined in Figure 3.4. A graded mesh with elements of size 0.05m near the jump was halved and the computation repeated. Since the local artificial dissipation is proportional to mesh spacing the dissipation is reduced accordingly. In both instances, the jump occurs over three elements and, of course, the steepness of the approximation to the jump improves as the mesh is refined. There is little spatial oscillation.

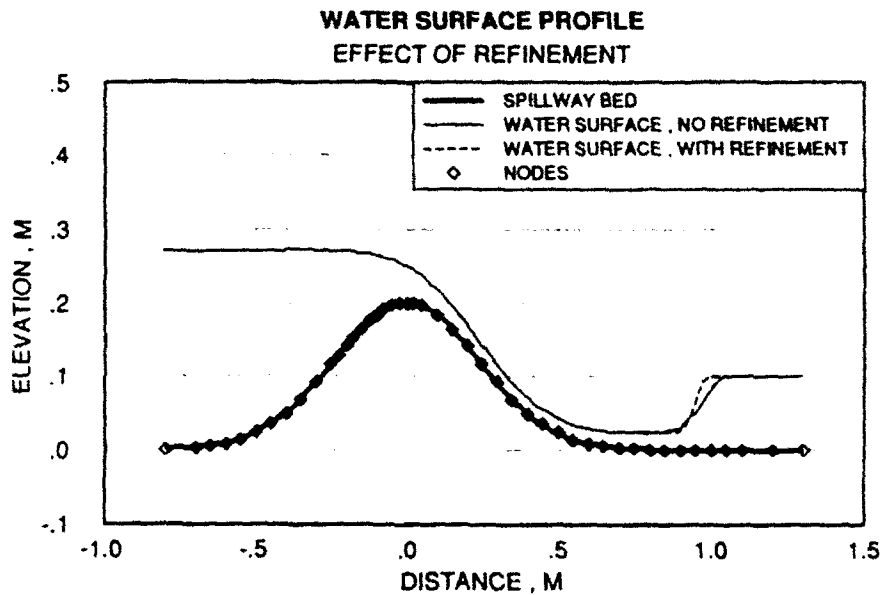


Figure 3.4: Water surface profile — effect of refinement.

3.6 Conclusions

The finite element model described here results from a shallow water perturbation analysis including bed curvature. In the event that the curvature is assumed to be identically zero, the model degenerates to the standard shallow water equations (without the mild-slope assumption). By computing the flow over a “bump” composed of a bed of continuous curvature for which flume results were available we observe that:

1. The full equation model yields an accurate prediction of the reservoir elevation (and thus spillway capacity) while the results excluding curvature effects are much poorer.

2. The results excluding curvature effects compare quite closely with the more complete model along the supercritical spillway face. However, subtle differences are sufficient to significantly shift the predicted location of the hydraulic jump.
3. The resolution of the jump in this model is spread over 2 or 3 elements. Thus the steepness of the jump can be improved by grid refinement (within the limits imposed by nonlinear effects).

In the next chapter we utilize these results to extend the formulation to a two-dimensional model.

Chapter 4

Model Extensions

4.1 Introduction

The complexity of the flow is more evident in two dimensions. The lateral distribution of flow and oblique standing waves can be reproduced. In the subcritical case a boundary disturbance propagates both downstream and upstream and so the shallow water equations cannot produce a standing wave here. In the supercritical region a boundary disturbance is swept downstream forming a standing wave or wake. The fluid velocity is greater than the speed of the free-surface wave celerity. Poor approach conditions result in standing waves within the spillway apron section. The concentration of flow in narrow regions can cause circulation and subsequent damage downstream. These problems can be relieved with improved flow training using well designed abutments. The flow features must be modeled to assess the design, requiring a model with both longitudinal and lateral resolution.

This chapter is concerned with the development of a finite element model that can reasonably address these conditions and the nonhydrostatic influences. Section 4.2 details the development of an improved convection scheme, 4.3 the depth-integrated equations, 4.4 is the application of the convection equation to these equations, and Sections 4.5 and 4.6 the viscous stresses and bed drag, respectively.

4.2 Finite Element Treatment – Convection Scheme

The focus of this investigation is on the curvilinear formulation, but an adequate system to address oscillation control is necessary to make this calculation. As discussed in the previous chapter on the finite element approximation of the one-dimensional problem, we must be concerned with possible oscillations resulting from both spurious modes and nonlinear effects. An artificial diffusion method was successfully introduced in Section 3.4.2, where the added dissipation was developed based on physical arguments. This system, while sufficient for of the one-dimensional equations in preliminary tests, is too simplistic for the eventual two-dimensional model. We now present a more complex form for two-dimensional analysis.

Some recent finite element approaches for the shallow water equations include the Taylor weak form (Baker and Iannelli [4]) and the Petrov Galerkin scheme (Katopodes [33]) which, in actual application, are almost identical (see also [5, 3, 34]). We will illustrate the basic ideas for the Taylor weak form and demonstrate a further improvement for our problem class.

Baker's model is based upon the work of Donea [19], Raymond and Garder [47] as well as Lohner, Morgan and Zienkiewicz [42]. The derivation can be clearly demonstrated using the one-dimensional model transport equation

$$\frac{\partial c}{\partial t} + \frac{\partial f}{\partial s} = 0 \quad (4.1)$$

The nonconservative form is given by

$$\frac{\partial c}{\partial t} + A \frac{\partial c}{\partial s} = 0 \quad (4.2)$$

where, $A = \frac{\partial f}{\partial c}$. Expanding c in a Taylor series in time we obtain

$$c^{m+1} = c^m + \Delta t \frac{\partial c^m}{\partial t} + \frac{\Delta t^2}{2} \frac{\partial^2 c^m}{\partial t^2} + \dots \quad (4.3)$$

where, the superscript indicates the time step, i.e., $t = m\Delta t$. Motivated by the well known Lax-Wendroff approach in finite differences, we may utilize relationships derived from (4.1)

$$\frac{\partial c}{\partial t} = -\frac{\partial f}{\partial s} \quad (4.4)$$

and

$$\frac{\partial^2 c}{\partial t^2} = -\alpha_1 \frac{\partial}{\partial s} \left(A \frac{\partial c}{\partial t} \right) - \alpha_2 \frac{\partial}{\partial s} \left(A^2 \frac{\partial c}{\partial s} \right) \quad (4.5)$$

with α_1, α_2 parameters. Following the Raymond and Garder scheme Baker and Ianneli [4] choose a combination of (4.5) and (4.6) with $\alpha_1 = \alpha_2 = \alpha$. The associated modified equation is

$$\frac{\partial c}{\partial t} + \frac{\partial f}{\partial s} - \frac{\alpha \Delta t}{2} \frac{\partial}{\partial s} \left(A \frac{\partial c}{\partial t} + A^2 \frac{\partial c}{\partial s} \right) = 0 \quad (4.6)$$

Katopodes [33] arrives at essentially the same result via the Petrov Galerkin approach. The test function is modified to include derivatives of the Galerkin test function ϕ as

$$\psi = \phi + \alpha A \frac{\partial \phi}{\partial s} \quad (4.7)$$

where, ψ is the new test function and α is a parameter with unit of 1/time.

Using (4.7) in the weighted residual statement for (4.1),

$$\int_{\Omega} \left(\phi \frac{\partial c}{\partial t} - \frac{\partial \phi}{\partial s} f + \alpha A \frac{\partial \phi}{\partial s} \left(\frac{\partial c}{\partial t} + A \frac{\partial c}{\partial s} \right) \right) ds + \int_{\partial \Omega} \phi f dl = 0 \quad (4.8)$$

where, Ω is the domain and $\partial\Omega$ is the boundary. This is similar to the form proposed by Dendy [18] and is based upon the Streamline Upwind Petrov Galerkin (SUPG) scheme of Hughes and Brooks [29].

In actual application of this method to the shallow water equations some deficiencies are apparent. The primary problem, for the hydrodynamic conditions we wish to simulate, is that the dissipative mechanism incorporated in this method is nonexistent near critical flow conditions; i.e., where the flow undergoes transition from subcritical to supercritical flow, or vice versa. This allows oscillations to gather at the spillway crest or near a jump. The standard one-dimensional shallow water equations illustrate this point.

These shallow water equations in nonconservative form may be written

$$\frac{\partial \mathbf{Q}}{\partial t} + \mathbf{A} \frac{\partial \mathbf{Q}}{\partial s} = 0 \quad (4.9)$$

where,

$$\begin{aligned} \mathbf{Q} &= \begin{Bmatrix} h \\ p \end{Bmatrix} \\ \mathbf{A} &= \begin{bmatrix} 0 & 1 \\ c^2 - u^2 & 2u \end{bmatrix} \\ p &= uh \\ c &= (gh)^{\frac{1}{2}} \end{aligned}$$

Now, applying the Petrov Galerkin approach to (4.9) and discretizing we obtain the corresponding finite element problem. It is instructive to examine the linearized steady problem for $\mathbf{A} = \text{constant}$, $\tilde{\mathbf{A}}$. Then the discrete system on a patch at node j becomes

$$\frac{1}{2} \tilde{\mathbf{A}} \delta \mathbf{Q}_j - \alpha \tilde{\mathbf{A}} \tilde{\mathbf{A}} \delta^2 \mathbf{Q}_j = 0 \quad (4.10)$$

where,

$$\delta Q_j \equiv (\rho^{j+1} - \rho^{j-1}) \begin{Bmatrix} \hat{h} \\ \hat{p} \end{Bmatrix}$$

$$\delta^2 Q_j \equiv \frac{1}{\Delta s} (\rho^{j+1} - 2\rho^j + \rho^{j-1}) \begin{Bmatrix} \hat{h} \\ \hat{p} \end{Bmatrix}$$

where we assume the numerical solution

$$h_j = \hat{h} \rho^j \quad (4.11)$$

$$p_j = \hat{p} \rho^j \quad (4.12)$$

j is a nodal index and ($\hat{\quad}$) above a variable indicates the amplitude. (These operators are similar to centered difference operators for first and second derivatives.) We may simplify the system by defining \mathbf{P} such that

$$\mathbf{P} \bar{\mathbf{A}} \mathbf{P}^{-1} = \mathbf{A} \quad (4.13)$$

where,

$$\mathbf{A} = \begin{bmatrix} \lambda_1 & 0 \\ 0 & \lambda_2 \end{bmatrix}$$

$$\lambda_1 = \bar{u} + \bar{c}$$

$$\lambda_2 = \bar{u} - \bar{c}$$

Here λ_1 and λ_2 are the eigenvalues of $\bar{\mathbf{A}}$, \bar{u} and \bar{c} are the constant values of velocity and celerity that form $\bar{\mathbf{A}}$, and \mathbf{P} and \mathbf{P}^{-1} are made up of the right and left eigenvectors of $\bar{\mathbf{A}}$. We find

$$\mathbf{P} = \frac{1}{\bar{c}} \begin{bmatrix} \lambda_2 & -1 \\ \lambda_1 & -1 \end{bmatrix} \quad (4.14)$$

$$\mathbf{P}^{-1} = \frac{1}{2} \begin{bmatrix} -1 & 1 \\ -\lambda_1 & \lambda_2 \end{bmatrix} \quad (4.15)$$

Equation (4.10) may be written as

$$-\frac{1}{2}P^{-1}\Lambda P\delta Q - \alpha P^{-1}\Lambda P P^{-1}\Lambda P\delta^2 Q = 0$$

or after simplification

$$\frac{1}{2}P\delta Q - \alpha\Lambda P\delta^2 Q = 0 \quad (4.16)$$

The equation set for each patch will then be

$$\left\{ \frac{1}{2} \begin{bmatrix} \lambda_2 & -1 \\ \lambda_1 & -1 \end{bmatrix} \delta - \alpha \begin{bmatrix} \lambda_1 \lambda_2 & -\lambda_1 \\ \lambda_1 \lambda_2 & -\lambda_2 \end{bmatrix} \delta^2 \right\} \begin{Bmatrix} \hat{h} \\ \hat{p} \end{Bmatrix} = 0 \quad (4.17)$$

For nontrivial solutions of \hat{h} and \hat{p} to exist, the determinant of the coefficient matrix must equal zero

$$\begin{vmatrix} \lambda_2 \left(\frac{1}{2}\delta - \alpha\lambda_1\delta^2 \right) & -\frac{1}{2}\delta + \alpha\lambda_1\delta^2 \\ \lambda_2 \left(\frac{1}{2}\delta - \alpha\lambda_2\delta^2 \right) & -\frac{1}{2}\delta + \alpha\lambda_2\delta^2 \end{vmatrix} = 0 \quad (4.18)$$

from which we have the roots

$$\rho = 1, 1, \frac{\alpha\lambda_1 + \frac{1}{2}}{\alpha\lambda_1 - \frac{1}{2}}, \frac{\alpha\lambda_2 + \frac{1}{2}}{\alpha\lambda_2 - \frac{1}{2}} \quad (4.19)$$

The value 1 is a multiple root and is the correct solution; i.e., the correct solution for a single boundary condition is that the velocity and depth are constants; the other values of ρ are spurious numerical roots. If these spurious roots are negative, a node-to-node oscillation may develop. The value of α that eliminates negative roots is

$$\alpha > \frac{\Delta s}{2|\lambda_1|}, \frac{\Delta s}{2|\lambda_2|} \quad (4.20)$$

If $|\lambda_2|$ is very small, as one would expect near a spillway crest (assuming $u > 0$), α would have to be quite large. This is indeed what happens when applying this method. The term α has units of 1/velocity. Katopodes suggests $\alpha = \epsilon \frac{\Delta s}{2|\lambda_1|}$,

where ϵ is a nondimensional coefficient [33]. This again does not scale the weighting of the Petrov Galerkin test function properly for each characteristic and oscillations can occur in this linearized example.

Instead we propose that the test function be modified so that it is scaled by each characteristic magnitude. We define the new test function as

$$\psi = \phi \mathbf{I} + \alpha \hat{\mathbf{A}} \frac{\partial \phi}{\partial s} \quad (4.21)$$

where,

$$\hat{\mathbf{A}} = \mathbf{P}^{-1} \hat{\Lambda} \mathbf{P}$$

$$\hat{\Lambda} \equiv \begin{bmatrix} \frac{\lambda_1}{|\lambda_1|} & 0 \\ 0 & \frac{\lambda_2}{|\lambda_2|} \end{bmatrix}$$

The result for the discrete model on a patch then is approximately

$$\frac{1}{2} \mathbf{P}^{-1} \mathbf{A} \mathbf{P} \delta \mathbf{Q} - \alpha \mathbf{P}^{-1} \hat{\Lambda} \mathbf{P} \mathbf{P}^{-1} \mathbf{A} \mathbf{P} \delta^2 \mathbf{Q} = 0$$

and to prevent oscillations

$$\alpha > \frac{\Delta s}{2} \quad (4.22)$$

This method provides an upwinded Petrov Galerkin test function that is scaled for each characteristic and can provide oscillation control at all Froude numbers. We will substitute $\alpha = \epsilon \Delta s$, where ϵ is a nondimensional parameter, in the model so that we need not input values dependent on element lengths. This method is a variation on the theme proposed by Courant, Isaacson, and Rees [15] for one-sided finite differences. These ideas were expanded to more general problems by Moretti [45], Chakravarthy [11], and Gabutti [25] as split-coefficient matrix methods and by the generalized flux vector splitting proposed

by Steger and Warming [55]. These one-sided differences based upon characteristic directions provide dissipation and therefore stability. The incorporation here is more subtle using a modification of the test function; also the degree to which the dissipation is apparent is controlled via the parameter ϵ instead of a totally one-side difference.

This approach is now extended to the two-dimensional case. We will use the condition of zero curvature in deriving our test function. This is significantly simpler than including curvature and can be justified on physical grounds. The shallow water equations (with ζ_1 and ζ_2 not identically equal to 1) are

$$\frac{\partial \mathbf{Q}}{\partial t} + \mathbf{A} \frac{\partial \mathbf{Q}}{\partial s_1} + \mathbf{B} \frac{\partial \mathbf{Q}}{\partial s_2} = \mathbf{H} \quad (4.23)$$

where,

$$\mathbf{Q} = \begin{Bmatrix} h \\ p \\ q \end{Bmatrix}$$

$$p = uh \quad , \quad q = vh$$

$$\mathbf{A} = \frac{1}{\zeta_1} \begin{bmatrix} 0 & 1 & 0 \\ (c^2 - u^2) & 2u & 0 \\ -uv & v & u \end{bmatrix}$$

$$\mathbf{B} = \frac{1}{\zeta_2} \begin{bmatrix} 0 & 0 & 1 \\ -uv & v & u \\ (c^2 - v^2) & 0 & 2v \end{bmatrix}$$

$$c = (g_3 h)^{\frac{1}{2}}$$

\mathbf{H} represents the additional terms which are not associated with the material derivative or pressure, and g_3 is the gravitational component in the bed-normal direction.

The test function we propose is

$$\psi = \phi \mathbf{I} + \varphi \quad (4.24)$$

where,

$$\begin{aligned} \varphi &= \epsilon \left(\Delta s_1 \frac{\partial \phi}{\partial s_1} \hat{\mathbf{A}} + \Delta s_2 \frac{\partial \phi}{\partial s_2} \hat{\mathbf{B}} \right) \\ \hat{\mathbf{A}} &= \mathbf{P}^{-1} \hat{\Lambda} \mathbf{P} \\ \mathbf{A} &= \begin{bmatrix} \lambda_1 & 0 & 0 \\ 0 & \lambda_2 & 0 \\ 0 & 0 & \lambda_3 \end{bmatrix} \\ \lambda_1 &= \frac{u}{\zeta_1} \\ \lambda_2 &= \frac{u+c}{\zeta_1} \\ \lambda_3 &= \frac{u-c}{\zeta_1} \\ \hat{\Lambda} &= \begin{bmatrix} \frac{\lambda_1}{|\lambda_1|} & 0 & 0 \\ 0 & \frac{\lambda_2}{|\lambda_2|} & 0 \\ 0 & 0 & \frac{\lambda_3}{|\lambda_3|} \end{bmatrix} \\ \mathbf{P} &\equiv \begin{bmatrix} -v & 0 & 1 \\ -\zeta_1 \lambda_3 & 1 & 0 \\ -\zeta_1 \lambda_2 & 1 & 0 \end{bmatrix} \\ \mathbf{P}^{-1} &= \frac{1}{2c} \begin{bmatrix} 0 & 1 & -1 \\ 0 & \zeta_1 \lambda_2 & -\zeta_1 \lambda_3 \\ 2c & v & -v \end{bmatrix} \end{aligned}$$

As in the one-dimensional case, $\lambda_1, \lambda_2,$ and λ_3 are the eigenvalues of \mathbf{A} , and \mathbf{P} and \mathbf{P}^{-1} are made up of the right and left eigenvectors.

Similarly, in the s_2 direction we have:

$$\begin{aligned} \hat{\mathbf{B}} &= \mathbf{R}^{-1} \hat{\Gamma} \mathbf{R} \\ \mathbf{R} &= \begin{bmatrix} \gamma_1 & 0 & 0 \\ 0 & \gamma_2 & 0 \\ 0 & 0 & \gamma_3 \end{bmatrix} \end{aligned}$$

$$\begin{aligned}
 \gamma_1 &= \frac{v}{\zeta_2} \\
 \gamma_2 &= \frac{v+c}{\zeta_2} \\
 \gamma_3 &= \frac{v-c}{\zeta_2} \\
 \hat{\Gamma} &= \begin{bmatrix} \frac{\gamma_1}{|\gamma_1|} & 0 & 0 \\ 0 & \frac{\gamma_2}{|\gamma_2|} & 0 \\ 0 & 0 & \frac{\gamma_3}{|\gamma_3|} \end{bmatrix} \\
 \mathbf{R} &\equiv \begin{bmatrix} -u & 1 & 0 \\ -\zeta_2\gamma_3 & 0 & 1 \\ -\zeta_2\gamma_2 & 0 & 1 \end{bmatrix} \\
 \mathbf{R}^{-1} &= \frac{1}{2c} \begin{bmatrix} 0 & 1 & -1 \\ 2c & u & -u \\ 0 & \zeta_2\gamma_2 & -\zeta_2\gamma_3 \end{bmatrix}
 \end{aligned}$$

The terms Γ , \mathbf{R} , and \mathbf{R}^{-1} in the s_2 direction are analogous to the relationship of \mathbf{A} , \mathbf{P} , and \mathbf{P}^{-1} in the s_1 direction.

4.3 Model Equations

The depth-integrated version of the momentum equations (2.58) is of some advantage in handling non-smooth conditions. The weak form solution for the no-curvature condition that one would encounter downstream of the spillway can be made to properly conserve momentum and mass through the jump. Other forms of the equations will not. In the case in which there is bed curvature, as we discussed in Section 3.3, these equations will contain additional terms due to the bed curvature which while finite through the jump will make an additional contribution that can cause an error in the jump location. Therefore in the vicinity of the jump these equations, which properly conserve mass and momentum for the no-curvature case, will only precisely conserve mass in the

curved bed state. Generally, in practical cases the strong jump is restricted to the region downstream of the spillway face where the bed contains no curvature.

These equations then are

$$L(Q) = M_t + \frac{1}{\zeta_1 \zeta_2} \left[\frac{\partial(\zeta_2 N_a)}{\partial s_1} + \frac{\partial(\zeta_1 N_b)}{\partial s_2} \right] + \frac{1}{\zeta_1 \zeta_2} \mathbf{H} = 0 \quad (4.25)$$

where,

$$Q = \begin{Bmatrix} h \\ p \\ q \end{Bmatrix}$$

$$p = \hat{u}h$$

$$q = \hat{v}h$$

$$f_1(s_3) = 1 - \kappa_1 s_3$$

$$f_2(s_3) = 1 - \kappa_2 s_3$$

$$M = \begin{Bmatrix} f_1(h) f_2(h) h \\ f_2\left(\frac{h}{2}\right) p \\ f_1\left(\frac{h}{2}\right) q \end{Bmatrix}$$

$$N_a = \left\{ \begin{array}{l} p c_1 \\ \frac{p^2}{h^2} a_2 + \frac{1}{2} \frac{p^2}{h^2} \left[\frac{a_1}{(f_1(h))^2} - a_2 \right] + \frac{1}{2} \frac{q^2}{h^2} \left[\frac{a_1}{(f_2(h))^2} - a_3 \right] + g_3 [h a_1 - a_4] \\ \frac{p q}{h^2} b_3 \end{array} \right\}$$

$$N_b = \left\{ \begin{array}{l} q c_2 \\ \frac{p q}{h^2} a_3 \\ \frac{q^2}{h^2} b_2 + \frac{1}{2} \frac{q^2}{h^2} \left[\frac{b_1}{(f_2(h))^2} - b_2 \right] + \frac{1}{2} \frac{p^2}{h^2} \left[\frac{b_1}{(f_1(h))^2} - b_3 \right] + g_3 [h b_1 - b_4] \end{array} \right\}$$

and the nonhomogeneous term

$$\mathbf{H} = \begin{Bmatrix} H_1 \\ H_2 \\ H_2 \end{Bmatrix}$$

where.

$$\begin{aligned}
H_1 &= 0 \\
H_2 &= \frac{1}{2} \frac{p^2}{h^2} \left\{ -\frac{\partial \zeta_2}{\partial s_1} \left[\frac{a_1}{(f_1(h))^2} - a_2 \right] + \zeta_2 \frac{\partial \kappa_2}{\partial s_1} \left[\frac{1}{2} \left(\frac{h}{f_1(h)} \right)^2 - a_5 \right] \right\} \\
&+ \frac{1}{2} \frac{q^2}{h^2} \left\{ -\frac{\partial \zeta_2}{\partial s_1} \left[\frac{a_1}{(f_2(h))^2} - a_3 \right] + \zeta_2 \frac{\partial \kappa_2}{\partial s_1} \left[\frac{1}{2} \left(\frac{h}{f_2(h)} \right)^2 - a_6 \right] \right\} \\
&+ \frac{q^2}{h^2} \left\{ -\frac{\partial \zeta_2}{\partial s_1} a_3 + \zeta_2 \frac{\partial \kappa_2}{\partial s_1} a_6 \right\} + \frac{pq}{h^2} \left\{ \frac{\partial \zeta_1}{\partial s_2} a_3 - \zeta_1 \frac{\partial \kappa_1}{\partial s_2} a_8 \right\} \\
&+ \kappa_1 \frac{p}{h} \left\{ \left[\frac{\partial}{\partial s_1} \left(\frac{\zeta_2 p}{h} \right) \right] a_9 - \frac{\zeta_2 p}{h} \frac{\partial \kappa_2}{\partial s_1} a_{10} + 2 \zeta_2 \frac{p}{h} \frac{\partial \kappa_1}{\partial s_1} a_{11} \right. \\
&+ \left. \frac{\partial}{\partial s_2} \left(\frac{\zeta_1 q}{h} \right) a_{12} - \frac{\zeta_1 q}{h} \frac{\partial \kappa_1}{\partial s_2} a_{13} + 2 \frac{\zeta_1 q}{h} \frac{\partial \kappa_2}{\partial s_2} a_{14} \right\} \\
&+ g_3 \left\{ -\frac{\partial \zeta_2}{\partial s_1} [h a_1 - a_4] + \frac{\zeta_2 h^3}{6} \frac{\partial \kappa_2}{\partial s_1} \right\} + \zeta_1 \zeta_2 g_1 a_7 \\
H_3 &= \frac{1}{2} \frac{q^2}{h^2} \left\{ -\frac{\partial \zeta_1}{\partial s_2} \left[\frac{b_1}{(f_2(h))^2} - b_2 \right] + \zeta_1 \frac{\partial \kappa_1}{\partial s_2} \left[\frac{1}{2} \left(\frac{h}{f_2(h)} \right)^2 - b_5 \right] \right\} \\
&+ \frac{1}{2} \frac{p^2}{h^2} \left\{ -\frac{\partial \zeta_1}{\partial s_2} \left[\frac{b_1}{(f_1(h))^2} - b_3 \right] + \zeta_1 \frac{\partial \kappa_1}{\partial s_2} \left[\frac{1}{2} \left(\frac{h}{f_1(h)} \right)^2 - b_6 \right] \right\} \\
&+ \frac{p^2}{h^2} \left\{ -\frac{\partial \zeta_1}{\partial s_2} b_3 + \zeta_1 \frac{\partial \kappa_1}{\partial s_2} b_6 \right\} + \frac{pq}{h^2} \left\{ \frac{\partial \zeta_2}{\partial s_1} b_3 - \zeta_2 \frac{\partial \kappa_2}{\partial s_1} b_8 \right\} \\
&+ \kappa_2 \frac{q}{h} \left\{ \left[\frac{\partial}{\partial s_2} \left(\frac{\zeta_1 q}{h} \right) \right] b_9 - \frac{\zeta_1 q}{h} \frac{\partial \kappa_1}{\partial s_2} b_{10} + 2 \zeta_1 \frac{q}{h} \frac{\partial \kappa_2}{\partial s_2} b_{11} \right. \\
&+ \left. \frac{\partial}{\partial s_1} \left(\frac{\zeta_2 p}{h} \right) b_{12} - \frac{\zeta_2 p}{h} \frac{\partial \kappa_2}{\partial s_1} b_{13} + 2 \frac{\zeta_2 p}{h} \frac{\partial \kappa_1}{\partial s_1} b_{14} \right\} \\
&+ g_3 \left\{ -\frac{\partial \zeta_1}{\partial s_2} [h b_1 - b_4] + \frac{\zeta_1 h^3}{6} \frac{\partial \kappa_1}{\partial s_2} \right\} + \zeta_1 \zeta_2 g_2 b_7
\end{aligned}$$

With the coefficients a_i , b_i , and c_i resulting from depth integration:

$$\begin{aligned}
a_1 &= \int_0^h f_2(s_3) ds_3 \\
a_2 &= \int_0^h \frac{f_2(s_3)}{(f_1(s_3))^2} ds_3 \\
a_3 &= \int_0^h \frac{1}{f_2(s_3)} ds_3 \\
a_4 &= \int_0^h s_3 f_2(s_3) ds_3 \\
a_5 &= \int_0^h \frac{s_3}{(f_1(s_3))^2} ds_3 \\
a_6 &= \int_0^h \frac{s_3}{(f_2(s_3))^2} ds_3 \\
a_7 &= \int_0^h f_1(s_3) f_2(s_3) ds_3
\end{aligned}$$

$$\begin{aligned}
a_8 &= \int_0^h \frac{s_3}{f_1(s_3) f_2(s_3)} ds_3 \\
a_9 &= \int_0^h \frac{1}{(f_1(s_3))^2} \int_0^{s_3} \frac{f_2(\xi)}{f_1(\xi)} d\xi ds_3 \\
a_{10} &= \int_0^h \frac{1}{(f_1(s_3))^2} \int_0^{s_3} \frac{\xi}{f_1(\xi)} d\xi ds_3 \\
a_{11} &= \int_0^h \frac{1}{(f_1(s_3))^2} \int_0^{s_3} \frac{\xi f_2(\xi)}{(f_1(\xi))^2} d\xi ds_3 \\
a_{12} &= \int_0^h \frac{1}{(f_1(s_3))^2} \int_0^{s_3} \frac{f_1(\xi)}{f_2(\xi)} d\xi ds_3 \\
a_{13} &= \int_0^h \frac{1}{(f_1(s_3))^2} \int_0^{s_3} \frac{\xi}{f_2(\xi)} d\xi ds_3 \\
a_{14} &= \int_0^h \frac{1}{(f_1(s_3))^2} \int_0^{s_3} \frac{\xi f_1(\xi)}{(f_2(\xi))^2} d\xi ds_3 \\
c_1 &= \frac{1}{\kappa_1 h} \left[\left(\frac{\kappa_2 - \kappa_1}{\kappa_1} \right) \log f_1(h) + \kappa_2 h \right] \\
c_2 &= \frac{1}{\kappa_2 h} \left[\left(\frac{\kappa_1 - \kappa_2}{\kappa_2} \right) \log f_2(h) + \kappa_1 h \right]
\end{aligned}$$

For the coefficients b_i simply swap the subscripts 1 and 2 in the κ_1 and κ_2 and f_1 and f_2 terms of a_i .

4.4 Application to Generalized Equations

The Petrov Galerkin formulation incorporates a combination of the Galerkin test function and a non-Galerkin component to control oscillations due to convection. The test function is that of equation (4.24) for the zero-curvature case, and involves bed velocities \hat{u} and \hat{v} .

The weighted residual statement becomes:

$$\int_{\Omega} \left(\phi M_t - \frac{1}{\zeta_1} \frac{\partial \phi}{\partial s_1} N_a - \frac{1}{\zeta_2} \frac{\partial \phi}{\partial s_2} N_b + \frac{\phi}{\zeta_1 \zeta_2} \mathbf{H} + \varphi \mathbf{L} \right) d\Omega$$

$$+ \oint_{\partial\Omega} (N_a n_1 + N_b n_2) dl = 0 \quad (4.26)$$

where, n_1 and n_2 are the components of the outward normal vector to the boundary.

The perturbation partial differential system defines a hyperbolic initial boundary value problem. We determine the appropriate boundary conditions relying upon the approach of Daubert and Graffe [17] and the discussions of Drolet and Gray [23] and Verboom et. al. [58]. Daubert and Graffe use the method of characteristics for this determination. The theory shows that the number of boundary conditions is equal to the number of characteristic half planes that originate exterior to the domain and which enter it. There are two families of characteristic surfaces at a point (s_{10}, s_{20}, t_0) . The first is a cone which slopes in the direction of flow and has a radius of the wave celerity multiplied by time. This generates the ring formed on the free-surface by a disturbance. The second is a plane which intersects the axis of the cone and represents the flow velocity. If a characteristic plane outside our domain intersects the boundary then the flow field inside the domain is influenced by the outside information which we must provide as a boundary condition. On the other hand, if the characteristic plane intersects the boundary from inside the domain, this is information leaving the domain and no boundary condition is needed. Physically, the first family is tracking a free-surface disturbance and the second is tracking a fluid element. Table 4.1 relates the number of boundary conditions to the direction of flow for sub- or supercritical flow conditions. u_n is the velocity component normal to the boundary.

The boundary conditions we implement in this model are:

Table 4.1: Number of boundary conditions required.

Flow direction	Subcritical Flow	Supercritical Flow
$u_n < 0$ (inward flow)	2	3
$u_n > 0$ (outward flow)	1	0
$u_n = 0$ (no flow)	1	1

- A slip flow boundary at a solid wall is common in shallow water applications. This corresponds to the condition $u_n = 0$ in Table 4.1. The boundary condition in the model is imposed through the weak statement. The implementation is as follows:

Mass Conservation Equation

$$\int_{\partial\Omega} \phi(p c_1 n_1 + q c_2 n_2) dl = 0 \quad (4.27)$$

s_1 Momentum Equation

$$\int_{\partial\Omega} \phi\left(\frac{p^2}{h^2} a_2 n_1 + \frac{pq}{h^2} a_3 n_2\right) dl = 0 \quad (4.28)$$

s_2 Momentum Equation

$$\int_{\partial\Omega} \phi\left(\frac{pq}{h^2} b_3 n_1 + \frac{q^2}{h^2} b_2 n_2\right) dl = 0 \quad (4.29)$$

- The upstream boundary condition is an essential boundary. If the flow here is subcritical then the flow components are specified as either \hat{u} and \hat{v} or p and q . If the flow is supercritical the depth is also specified.
- The downstream boundary condition is unspecified if the flow is supercritical there. If the flow is subcritical the depth is specified by substituting the specified depth in the boundary integral terms of the momentum equations.

4.5 Viscous Stress

The viscous stress is of less importance in the calculation of the free-surface except as the flow passes through the hydraulic jump. The contribution is small when the flow is smooth. We base our stress calculation upon the velocity and metric gradients at the bed, in this way we do not produce a lateral or longitudinal stress by our assumed vertical velocity profile. The stresses (see Boreisi and Chong [8]) then are:

$$\sigma_{11} = 2\nu\rho \left(\frac{1}{\zeta_1} \frac{\partial \hat{u}}{\partial s_1} + \frac{\hat{v}}{\zeta_1 \zeta_2} \frac{\partial \zeta_1}{\partial s_2} \right) \quad (4.30)$$

$$\sigma_{21}, \sigma_{12} = \nu\rho \left(\frac{1}{\zeta_2} \frac{\partial \hat{u}}{\partial s_2} + \frac{1}{\zeta_1} \frac{\partial \hat{v}}{\partial s_1} - \frac{\hat{v}}{\zeta_1 \zeta_2} \frac{\partial \zeta_2}{\partial s_1} - \frac{\hat{u}}{\zeta_1 \zeta_2} \frac{\partial \zeta_1}{\partial s_2} \right) \quad (4.31)$$

$$\sigma_{22} = 2\nu\rho \left(\frac{1}{\zeta_2} \frac{\partial \hat{v}}{\partial s_2} + \frac{\hat{u}}{\zeta_1 \zeta_2} \frac{\partial \zeta_2}{\partial s_1} \right) \quad (4.32)$$

The first subscript indicates the face upon which the stress acts and the second is its direction. When applied to our numerical system we obtain the following additional contributions:

s_1 Momentum Equation Contribution:

$$ST_1 = \int_{\Omega} \frac{a_7}{\rho} \left(\frac{1}{\zeta_1} \frac{\partial \phi}{\partial s_1} \sigma_{11} + \frac{1}{\zeta_2} \frac{\partial \phi}{\partial s_2} \sigma_{21} \right) d\Omega \quad (4.33)$$

s_2 Momentum Equation Contribution:

$$ST_2 = \int_{\Omega} \frac{b_7}{\rho} \left(\frac{1}{\zeta_1} \frac{\partial \phi}{\partial s_1} \sigma_{12} + \frac{1}{\zeta_2} \frac{\partial \phi}{\partial s_2} \sigma_{22} \right) d\Omega \quad (4.34)$$

These contributions are made to the left hand side of equation (4.26). The stress jump across interelement boundaries is set to zero and along the domain edge a stress-free boundary is assumed.

As an estimate of these turbulent eddy viscosities generated by the bottom friction, we use an empirical formula [49, 12]

$$\nu_t = C_B h f^{\frac{1}{2}} |u| \quad (4.35)$$

where, ν_t is the turbulent viscosity, C_B is a coefficient that varies between 0.1 and 1.0, and f is the Darcy-Weisbach friction coefficient (see e.g. King and Brater [36]). The turbulent contribution to viscosity is generally much larger than the molecular viscosity.

4.6 Bed Drag

We adopt the common practise in hydraulic engineering of using an empirical relationship developed by Manning and extended to curved beds in one dimension by Dressler and Yevjevich [21]. We shall extend this to two dimensions. The original approach uses the Chezy coefficient, C_h , defined for steady flow and for determination of the average flow over a cross section. In the "fully rough" regime, the bed stress may be defined by $\sigma_{bed} = -\Lambda \rho u^2$, where Λ and C_h are functions of the size of the flow channel and the bed roughness and independent of Reynolds number and so the Manning's relationship is applicable. The term σ_{bed} will be the bed drag force addition to equation (4.26). Here we apply Manning's relationship of $\Lambda = \frac{gn^2}{R^3}$, where R is the hydraulic radius (ratio of cross-sectional area to wetted perimeter) and n is Manning's coefficient.

We shall demonstrate the derivation of the force terms for the s_1 momentum equation. Consider the infinitesimal volume in Figure 4.1. The

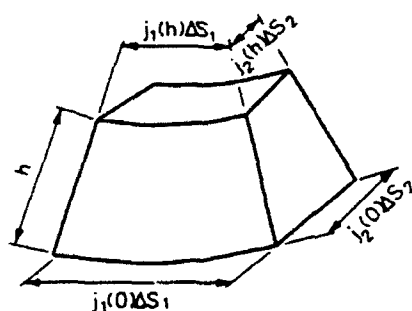


Figure 4.1: Infinitesimal volume for calculation of bed drag force.

bed surface area is

$$A = \zeta_1 \zeta_2 \Delta s_1 \Delta s_2 \quad (4.36)$$

so the total bed drag force is given by

$$f_{s1} = -\rho \frac{gn^2}{R^{\frac{1}{3}}} \hat{u} (\hat{u}^2 + \hat{v}^2)^{\frac{1}{2}} \zeta_1 \zeta_2 \Delta s_1 \Delta s_2 \quad (4.37)$$

The corresponding volume is

$$V = \int_0^h j_1(s_3) j_2(s_3) ds_3 \zeta_1 \zeta_2 \Delta s_1 \Delta s_2 = a_7 \zeta_1 \zeta_2 \Delta s_1 \Delta s_2 \quad (4.38)$$

and the force per unit volume then is

$$\frac{f_{s1}}{V} = -\rho \frac{gn^2}{R^{\frac{1}{3}}} \hat{u} (\hat{u}^2 + \hat{v}^2)^{\frac{1}{2}} \quad (4.39)$$

The hydraulic radius may be approximated by

$$R \approx \frac{V}{A} = a_7 \quad (4.40)$$

Therefore, the force per unit mass as it appears on the right hand side of the s_1 momentum equation becomes:

$$Fb_1 = -\frac{gn^2p((p^2 + q^2)^{\frac{1}{2}})}{ha_7^{\frac{4}{3}}} \quad (4.41)$$

and similarly for the s_2 momentum equation:

$$Fb_2 = -\frac{gn^2q((p^2 + q^2)^{\frac{1}{2}})}{hb_7^{\frac{4}{3}}} \quad (4.42)$$

Once again, these terms will appear as additions in (4.26) for the bed drag force.

4.7 Model Description

The finite element approximation for equation (4.26) becomes:

$$\sum_c \left[\int_{\Omega_c} \left(\phi_i \tilde{M}_i - \frac{1}{\tilde{\zeta}_1} \frac{\partial \phi_i}{\partial s_1} \tilde{N}_a - \frac{1}{\tilde{\zeta}_2} \frac{\partial \phi_i}{\partial s_2} \tilde{N}_b + \frac{\phi_i}{\tilde{\zeta}_1 \tilde{\zeta}_2} \tilde{H} + \varphi_i \tilde{L} \right) d\Omega_c \right. \\ \left. + \oint_{\partial\Omega_c \cap \partial\Omega} (\tilde{N}_a n_1 + \tilde{N}_b n_2) dl \right] = 0 \quad (4.43)$$

where, the symbol $\tilde{}$ indicates the discrete value of the quantity and the subscript indicates a particular test function. The geometry and flow variables are represented using the finite element basis; e.g.,

$$\tilde{Q} = \sum_j \phi_j Q_j$$

and the function φ_i is defined as

$$\varphi_i = \epsilon \left(\Delta s_1 \frac{\partial \phi_i}{\partial s_1} \tilde{\mathbf{A}} + \Delta s_2 \frac{\partial \phi_i}{\partial s_2} \tilde{\mathbf{B}} \right)$$

We use quadrilateral bilinear elements with nodes at the element corners, the local element coordinates are shown (see e.g. [6]) in Figure 4.2. The

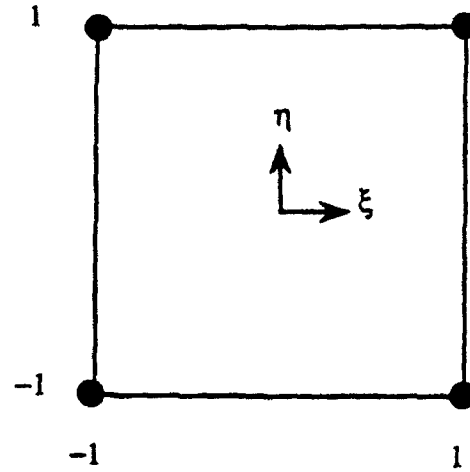


Figure 4.2: Local bilinear element.

grid intervals Δs_1 and Δs_2 in the physical domain are chosen in the same manner as Katopodes [33]:

$$\Delta s_1 = 2 \left[\left(\frac{\partial s_1}{\partial \xi} \right)^2 + \left(\frac{\partial s_1}{\partial \eta} \right)^2 \right]^{\frac{1}{2}} \quad (4.44)$$

$$\Delta s_2 = 2 \left[\left(\frac{\partial s_2}{\partial \xi} \right)^2 + \left(\frac{\partial s_2}{\partial \eta} \right)^2 \right]^{\frac{1}{2}} \quad (4.45)$$

From Taylor series arguments, the temporal derivative may be represented as

$$\gamma \frac{Q_j^{n+1} - Q_j^n}{\Delta t} + (1 - \gamma) \frac{Q_j^n - Q_j^{n-1}}{\Delta t} = \frac{\partial Q_j^{n+1}}{\partial t} + \tau_j \quad (4.46)$$

where, the subscript j indicates a particular node location, the superscript indicates the time step, and τ_j indicates the truncation error,

$$\tau_j = \left(\gamma - \frac{3}{2} \right) \frac{\partial^2 Q}{\partial t^2} \Delta t - \left(\gamma - \frac{7}{6} \right) \frac{\partial^3 Q}{\partial t^3} (\Delta t)^2 + O(\Delta t)^3 \quad (4.47)$$

If $\gamma = \frac{3}{2}$ this defines a second-order backward difference in time; if $\gamma = 1$ the standard first-order backward difference is obtained (both schemes are unconditionally stable for the linear problem).

We address the nonlinearities in equation (4.44) by using the Newton Raphson technique (see [9]). The residual \mathbf{R}_i for a particular test function ϕ_i in each set of equations is forced toward zero by the iteration: for $k = 1, 2, \dots$ solve the Jacobian system

$$\frac{\partial \mathbf{R}_i^k}{\partial \mathbf{Q}_j^k} \Delta \mathbf{Q}_j^k = -\mathbf{R}_i^k \quad (4.48)$$

$$\mathbf{Q}_j^{k+1} = \mathbf{Q}_j^k + \Delta \mathbf{Q}_j^k \quad (4.49)$$

where k indicates the iteration, i is the test function index and j is the nodal index.

Equation (4.48) represents a system of linear algebraic equations that must be solved for each iteration and time step. A "Profile" solver incorporates efficient coefficient matrix storage and is implemented in the present study. In this method the upper triangular portion of the coefficient matrix is stored by columns and the lower by rows. The zeros outside the profile are not stored or involved in computation. The necessary arrays are then a vector comprised of the columns of the upper triangular portion of the coefficient matrix, another for the rows of the lower portion, and a pointer vector to locate the diagonal entries. Triangular decomposition of the coefficient matrix is used in a direct solution. The program to construct the triangular decomposition of the coefficient matrix uses a compact Crout variation of Gauss elimination.

Chapter 5

Validation and Practical Simulation

Numerical tests are conducted in two stages. In Section 5.1 we make validation tests against several standard benchmark cases. Then in Section 5.2 we demonstrate the model's capability to predict actual flow conditions. Here we make comparisons to flume results and compare these results to those predicted using other shallow water equation models of approximately the same computational complexity.

5.1 Model Validation

Several simple cases with analytic solutions are first considered to validate the scheme and program. The basis of these is the Bernoulli Equation written along the water surface. For smooth solutions with no dissipation, energy along a streamline should be constant. The Bernoulli equation along the water surface may be written:

$$\frac{v_s^2}{2g} + z_s = E_m \quad (5.1)$$

where,

E_m = mechanical energy (in units of length, e.g. ft-lbs per lb of water)

z_s = water surface elevation

v_s = velocity magnitude at the water surface

In testing the precision of the model we define the error in terms of deviation from a constant mechanical energy as follows:

$$\bar{E}_m = \frac{\int_{\Omega} E_m j_1(h) j_2(h) ds_1 ds_2}{\int_{\Omega} j_1(h) j_2(h) ds_1 ds_2} \quad (5.2)$$

$$\|\varepsilon_m\| = \left[\frac{\int_{\Omega} (E_m - \bar{E}_m)^2 j_1(h) j_2(h) ds_1 ds_2}{\int_{\Omega} j_1(h) j_2(h) ds_1 ds_2} \right]^{\frac{1}{2}} \quad (5.3)$$

So that \bar{E}_m is the average mechanical energy and $\|\varepsilon_m\|$ represents an error in terms of mechanical energy.

5.1.1 Constant Curvature.

The first test is for a constant curvature. These tests are conducted for constant curvature in the s_1 direction with no curvature in the s_2 direction, and then for constant curvature in the s_2 direction with no curvature in the s_1 direction. All tests are with straight walls for both supercritical and subcritical conditions.

The radius of curvature chosen is 30m, and the channel length is 20m divided into elements of length 1m. The width is 4m divided into 1m wide elements. In addition to the error in mechanical energy, we plot the depth and bed velocity along the channel centerline compared to the analytic solution for the calculated average energy. We show these plots for flow in the s_1 direction; the s_2 plots were indistinguishable from the s_1 results.

The subcritical test conditions are shown in Table 5.1. For subcritical flow two upstream boundary conditions and one downstream boundary condition are specified. Typically p and q are given upstream and water surface

Table 5.1: Circular channel, subcritical flow.

Input Parameters	
g	9.80 m/sec ²
n	0
ν_t	0
Δt	2sec
Simulation Time	100sec
Iterations	2
ϵ	0.01
Boundary Conditions	
Upstream	
p	1.048 m ³ /s/m
q	0
Downstream	
Tailwater Elevation	1.0439m

Table 5.2: Circular channel subcritical flow results.

	E_m	$\ \epsilon_m\ $
s_1	1.046120	4.024×10^{-4}
s_2	1.046122	4.084×10^{-4}

elevation downstream. The results of the model run at the end of the simulation are shown in Table 5.2. The mechanical energy in the model is very close to a constant. For subcritical flow the energy should be close to the variation in elevation, so it is apparent that the error in elevation is less than 0.001m. A plot of the centerline profiles of bed velocity and water surface is shown in Figure 5.1. The water surface dips over the crest as one would expect for subcritical flow and, of course, the velocity is a maximum there. A comparison

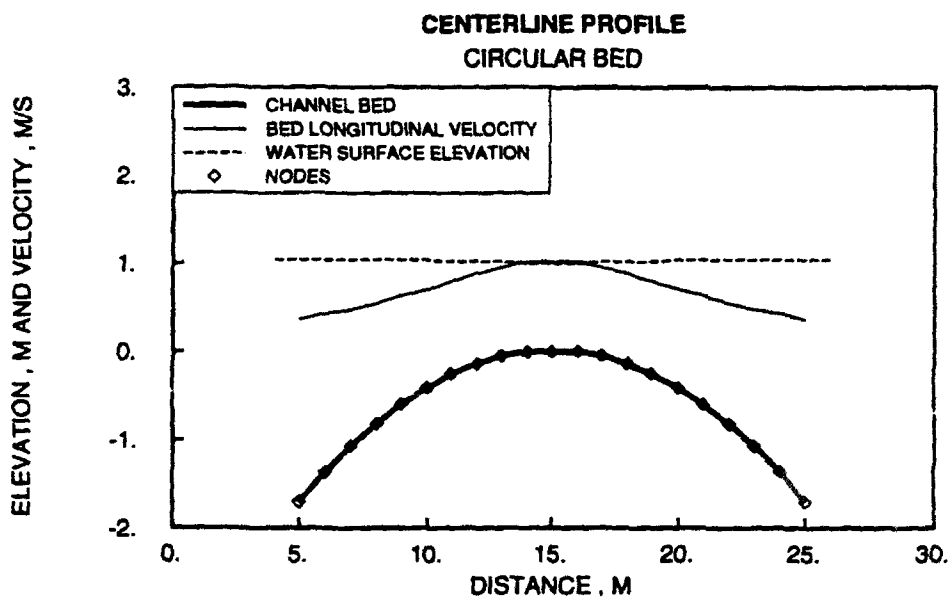


Figure 5.1: Circular channel, subcritical flow: bed velocity and water surface elevation.

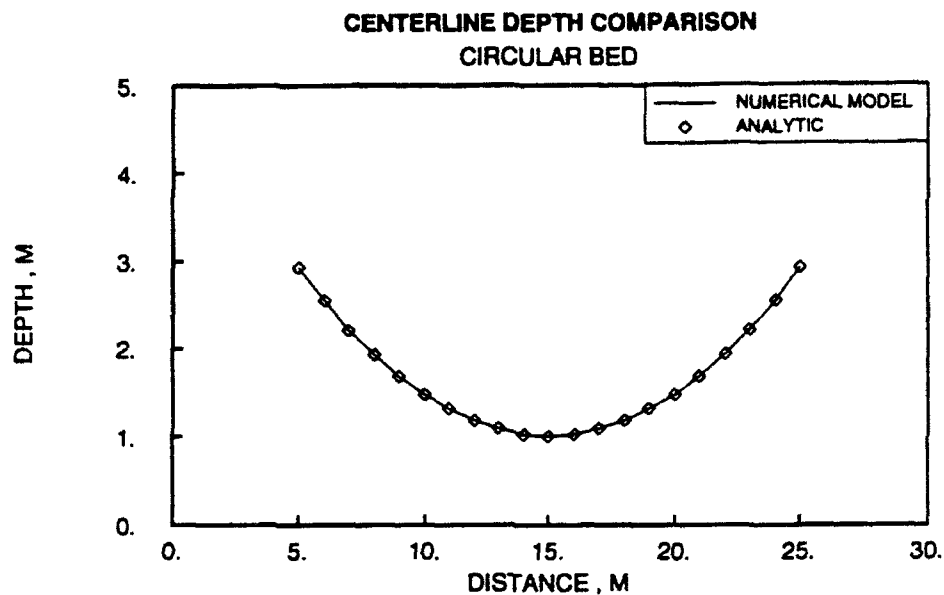


Figure 5.2: Circular channel, subcritical flow: comparison of depth from model with analytic solution.

between the numerical model and analytic results is shown in the two subsequent figures. Figure 5.2 provides a comparison of depths and Figure 5.3 is for bed velocity. The comparison is extremely close, and since the energy error is small we know the comparison over width is also good.

The test for supercritical flow considers the treatment and effect of the downstream boundary. Since the flow is supercritical at this boundary no condition is specified. The upper portion is subcritical so that only p and q must be specified upstream. The flow changes to supercritical near the crest. The water surface rises or falls from initial data to the level at which the steady-state discharge can be maintained.

The downstream depth is calculated by the model and as a result is

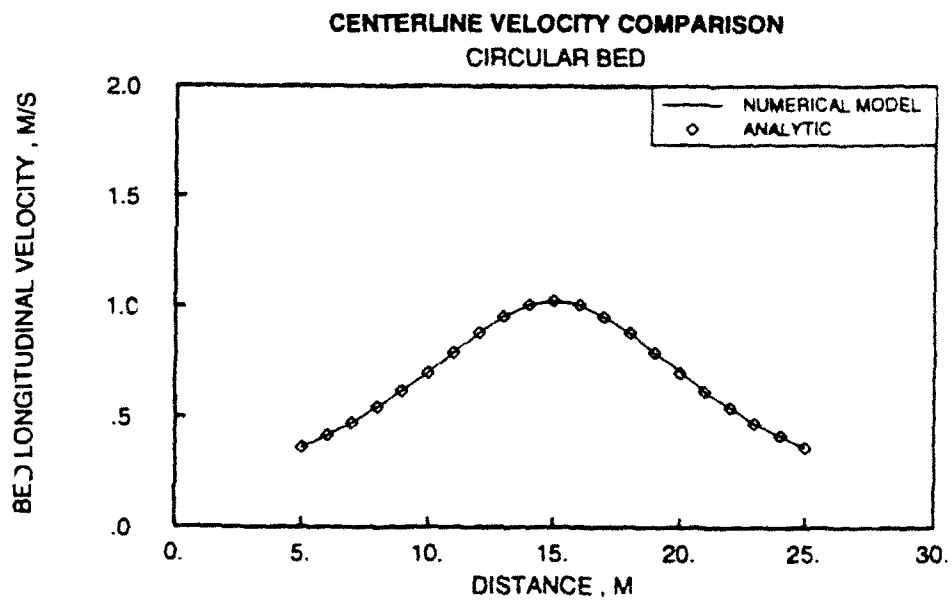


Figure 5.3: Circular channel, subcritical flow: comparison of the bed velocity from the model with analytic solution.

Table 5.3: Circular channel, supercritical flow.

Input Parameters	
g	9.80m/sec ²
n	0
ν_t	0
Δt	1sec
Simulation Time	100sec
Iterations	2
ϵ	0.01
Boundary Conditions	
Upstream	
p	1.048m ³ /s/m
q	0

Table 5.4: Circular channel supercritical flow results.

	E_m	$\ \epsilon_m\ $
s_1	0.6973918	1.911x10 ⁻³
s_2	0.6973964	1.912x10 ⁻³

somewhat less stable so the time step is reduced accordingly. Table 5.3 shows the input parameters for the calculation.

The error compared with Bernoulli's equation is shown in Table 5.4. As expected the error is greater than for the subcritical case but it is still relatively small.

The actual flow centerline profiles are shown in Figure 5.4. The water depth decreases until it becomes supercritical near the crest. The bed velocity is nearly 7m/s at the downstream boundary. The comparison to the analytic

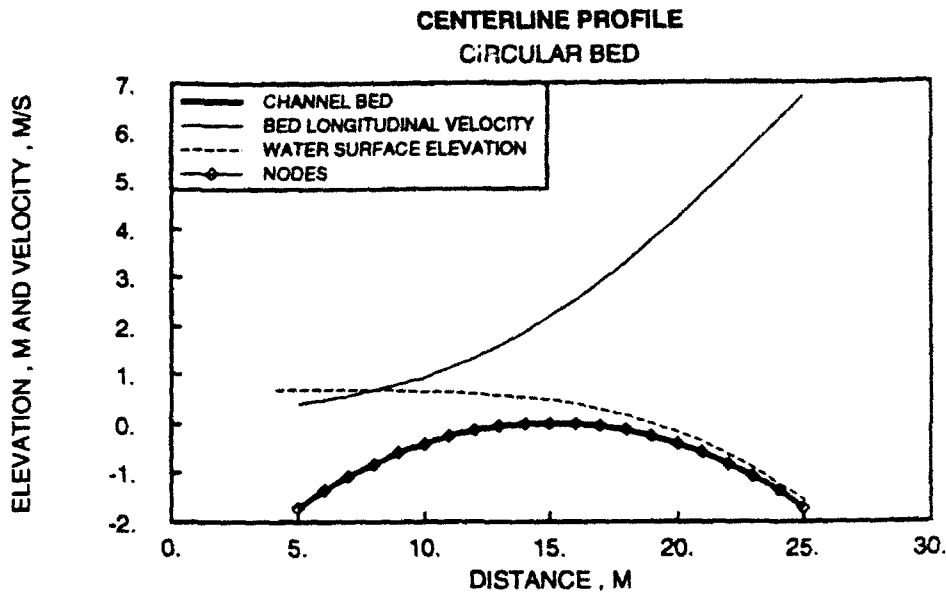


Figure 5.4: Circular channel, supercritical flow: bed velocity and water surface elevation profiles.

result is shown in Figures 5.5-5.6. Once again, the model yields results very close to the analytic solution.

5.1.2 Variable Curvature.

For a more general test we consider a variable curvature case. Specifically, we return to the flume geometry of Sivakumaran [51, 52, 53] given by $Z = 0.20e^{[-\frac{1}{2}(\frac{x}{30})^2]}$, where x is the horizontal distance and Z is the elevation. The test input parameters are shown in Table 5.5. The simulated flume contains 245 nodes and 192 elements. The lateral resolution consists of 4 elements of width 0.05m. Longitudinally, the resolution is concentrated just upstream of the crest, where the greatest variation in depth occurs. The minimum element

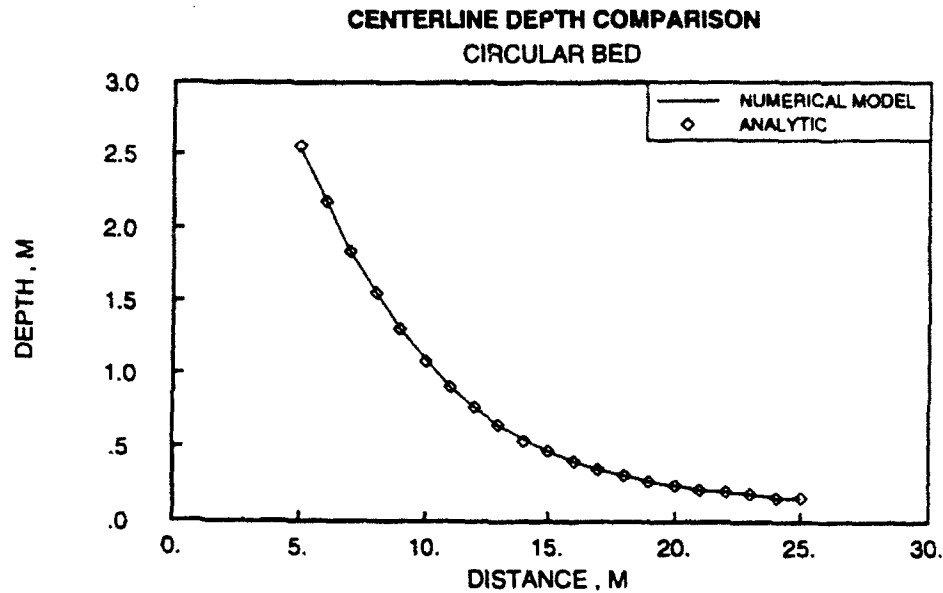


Figure 5.5: Circular channel, supercritical flow: comparison of depth from model with analytic solution.

Table 5.5: Variable curvature flume.

Input Parameters	
g	9.80m/sec ²
n	0
ν_t	0
Δt	0.05sec
Simulation Time	20sec
Iterations	3
ϵ	0.02
Boundary Conditions	
Upstream	
p	0.03599m ³ /s/m
q	0

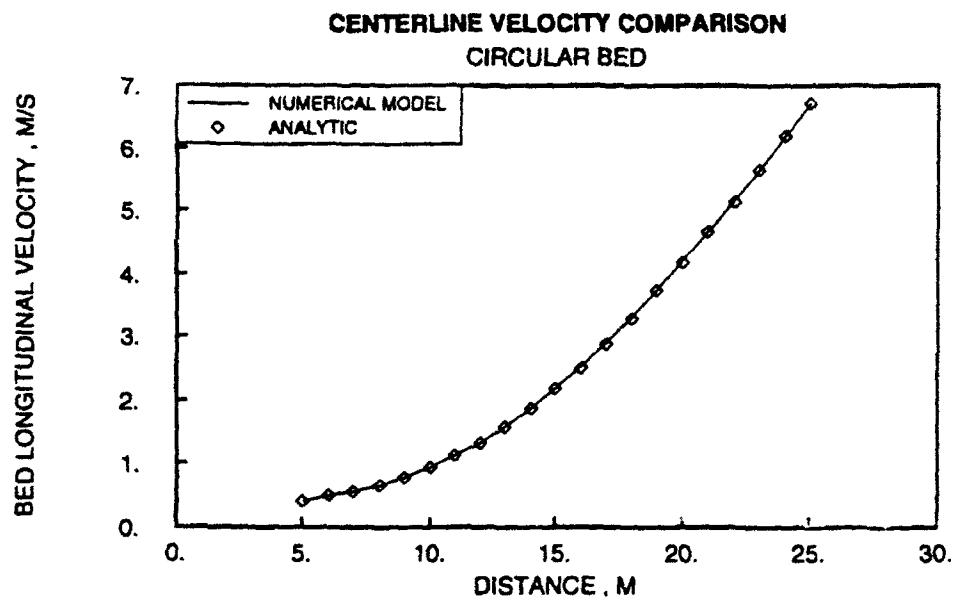


Figure 5.6: Circular channel, supercritical flow: comparison of the bed velocity from the model with analytic solution.

Table 5.6: Variable curvature flow results.

	E_m	$\ \epsilon_m\ $
s_1	0.273170	2.959×10^{-4}
s_2	0.273090	3.990×10^{-4}

length is 0.02m and the maximum is 0.05m. With a 0.05 second timestep a free-surface wave can traverse about 3 or 4 of the smallest elements in a single timestep; i.e., the equivalent CFL number [14] is about 3 or 4. Our initial solution is a fairly poor description of the steady solution so the starting timestep is 0.02 seconds. After 2 seconds of simulation it was increased to 0.05. The results of the simulation are shown in Table 5.6.

The ratio $\|\epsilon_m\|/\bar{E}_m$ for the variable curvature case is between 0.00108 and 0.00146 compared to the supercritical constant curvature result of about 0.00274 and subcritical result of 0.000390. Thus, the variable curvature is no worse than for supercritical flow over a constant curvature. The significant difference is in comparison to subcritical flow. Supercritical flow by nature is less regular and the results with the model reflect this. These validation studies confirm that the model accurately approximates the stated differential equations. We now apply the model to more realistic practical flow studies.

5.2 Comparison to Physical Measurements in Flumes

The first test contains no bed curvature, but is a supercritical transition in which the disturbances at the wall propagate across the flume. This is a good test of the numerical scheme and boundary condition implementation.

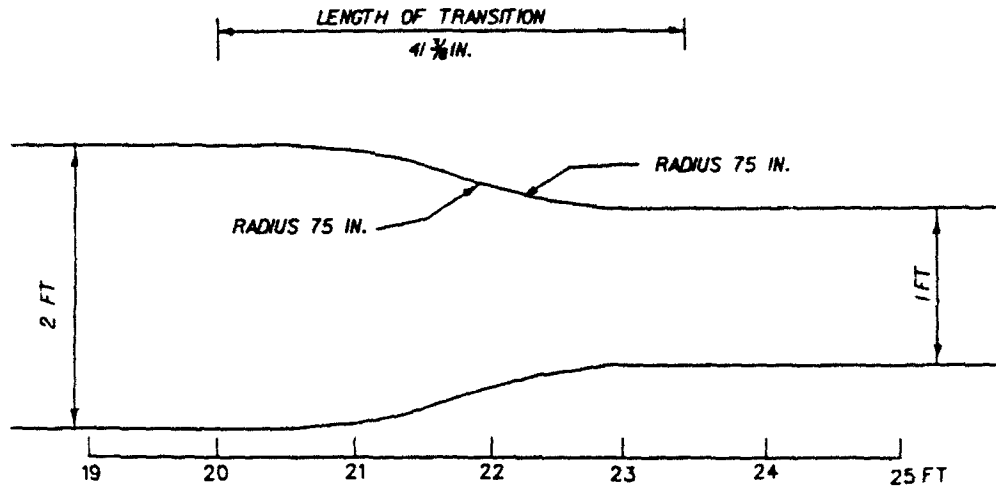


Figure 5.7: Flume geometry: supercritical transition.

We next compare results for our generalized set of shallow water equations, the standard steep-slope shallow water equations, and the St. Venant equations of a spillway form against data collected by Sivakumaran [51]. These methods are all of about the same computational effort. The data set includes bed pressures and water surface elevations. The final test is of an outletworks flume that is supercritical throughout containing bed curvature and lateral transitions. This is the most general case that we will test. In all comparisons, model resolution is refined until no significant change results from additional refinement.

5.2.1 Supercritical Transition.

The flume data, for this test, are reported in Ippen and Dawson [31]. The flume narrows from 2ft to 1ft wide using two equal radius circular arcs as shown in Figure 5.7. The numerical representation of this flume extends

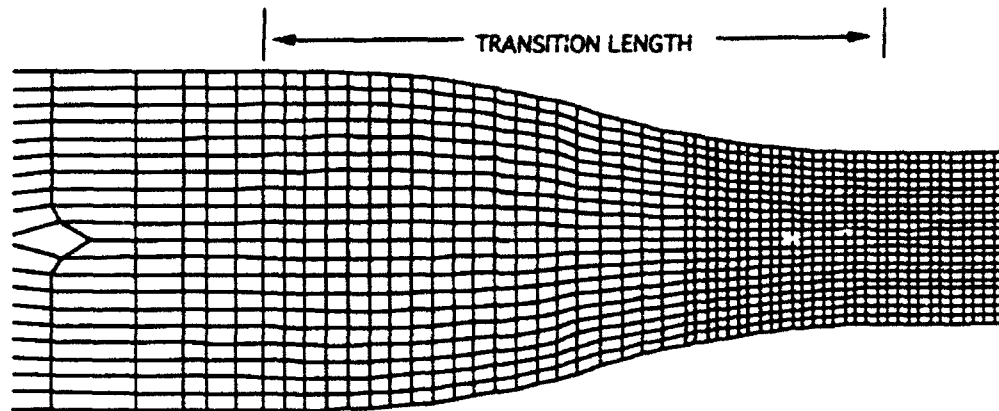


Figure 5.8: Computational grid, supercritical transition.

upstream 20ft from the start of the curve and downstream below the transition by about 30ft. The extension upstream is to allow the model to reach uniform flow before the transition and downstream to make sure the boundary condition does not influence the calculations in the area of interest. These long extensions are actually overly cautious. The numerical grid is composed of 4585 nodes and 4314 elements with a maximum length of 1ft and a minimum of 0.06ft. Laterally the channel is broken into 20 elements in the area of interest and near the upstream and downstream boundaries only 6 elements. The numerical grid in the transition area is shown in Figure 5.8. Other model input parameters are shown in Table 5.7. The bed slope and roughness are chosen to provide uniform flow approaching the transition. The flow conditions are more difficult than in the previous test and the value of ϵ was increased to 0.10 to maintain stability. The value of ν_t is chosen to correspond to $C_B = 0.4$, see equation

Table 5.7: Supercritical transition.

Input Parameters	
g	32.208ft/sec ²
n	0.005
ν_t	0.02ft ² /sec
Δt	0.03sec
Simulation Time	500sec
Iterations	2
ϵ	0.10
bed slope	0.0125
Boundary Conditions	
Upstream	
p	0.7161ft ³ /s/ft
q	0
h	0.0998ft

(4.35). The amplitude of the standing wave predicted by the numerical model is fairly sensitive to C_B as one might expect.

A perspective view of the computed water surface is shown in Figure 5.9. The transition causes a disturbance that reflects down the channel forming a diamond-shaped wave pattern. A comparison of computed and experimental water surface contours is shown in Figure 5.10. The numerical model certainly captures the overall features of the flume. Not surprisingly it is symmetric unlike the flume (since it is difficult to control the inflow into a physical flume). The numerical model predicts the location of the initial peak upstream of the flume's peak by about 0.5ft (about 15 % of the transition length) and each subsequent peak is increasingly off. The distance between the first two peaks is 3.5ft but the model produces only 2.8ft separation. Further down the channel

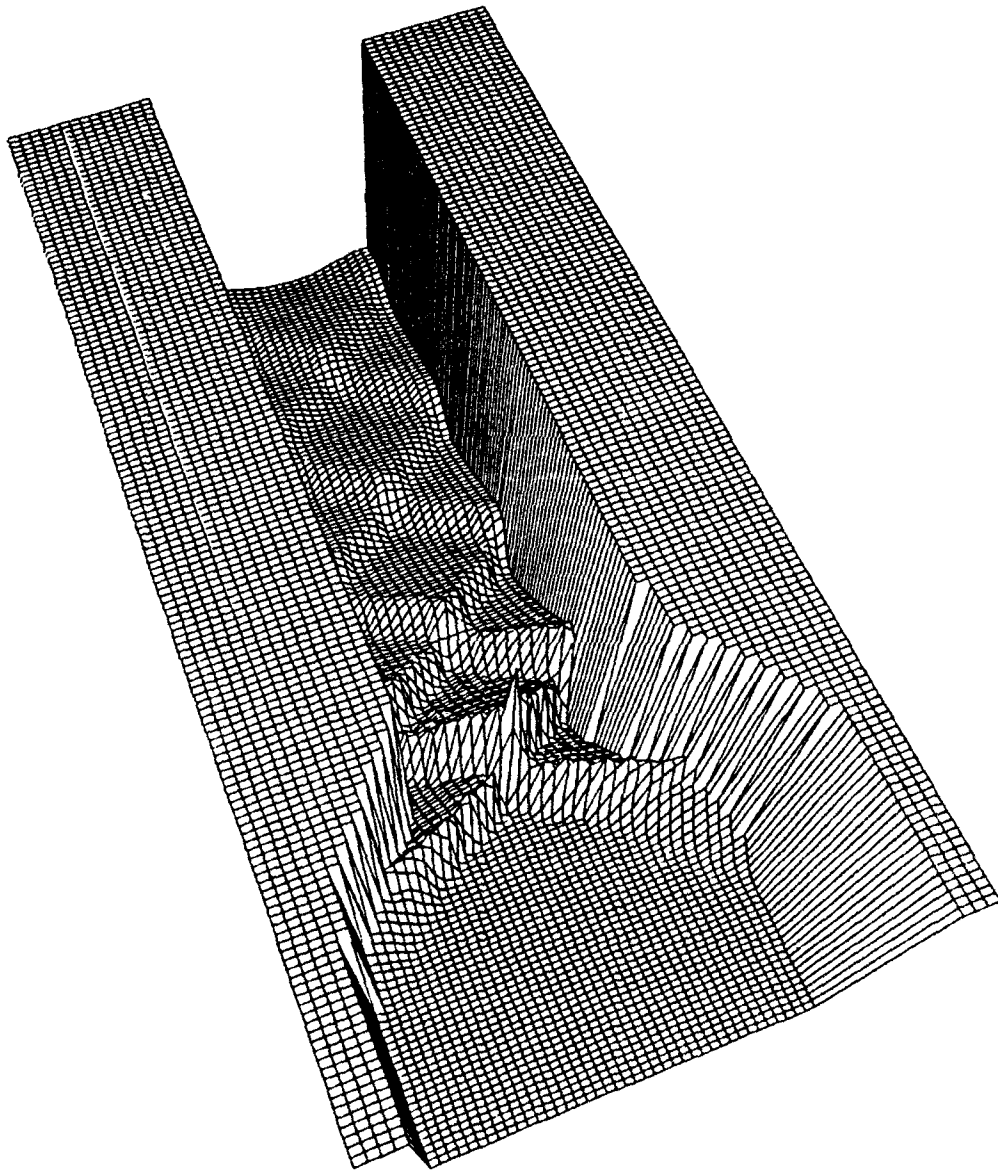


Figure 5.9: Supercritical transition: water surface, 3-d perspective view.

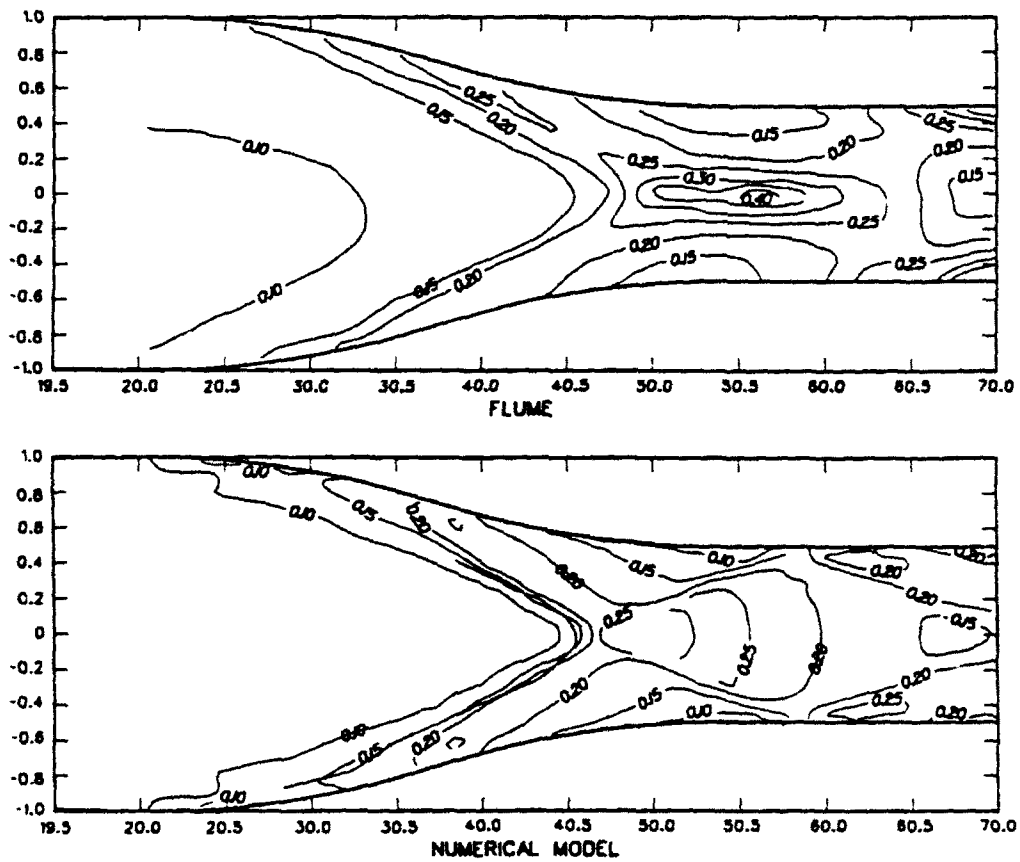


Figure 5.10: Supercritical transition: comparison of water surface contours, all units ft.

the wavelength in the flume is 3.3ft and the numerical model gives 3.0ft. This is a direct result of the shallow water assumption. The various wavelengths actually should travel at different speeds with the shorter ones traveling more slowly. In the shallow water model all waves travel at the speed of an infinitely long wave. For example, from equation (1.1) we see that the long wave celerity for a depth of 0.3ft is 3.10ft/sec. For the longest wavelength in the flume, 3.3ft, the celerity is 2.95ft/sec; the shorter wavelengths are even more significantly reduced. This higher wave celerity means that the waves which originate at a sidewall boundary will form a standing wave that is swept less backwards by the current. Overall though, within the limitations of the shallow water assumptions, the comparison is reasonable with symmetry preserved and the shapes of the oblique standing waves demonstrated.

5.2.2 Spillway Form

At this point we revisit questions concerning the generalized shallow water equations as differentiated from the more frequently applied St. Venant equations and the generalized shallow water equations with curvature set to zero (the standard steep-slope shallow water equations). We do this by reconsidering Sivakumaran's flume results with the improved model, continuing the preliminary study reported in Chapter 3. Here we first address longitudinal issues since the flume is essentially one-dimensional, leaving lateral and more general two-dimensional issues to the next section.

While the generalized shallow water equations are much more complicated than the St. Venant equations, we are using bilinear elements with the

identical number of gauss points for each approach. Hence the models are of approximately the same computational effort. If one moved to a higher-order perturbation expansion, much more computational effort would be necessary. Previous studies by Dressler and Yevjevich [22] compare Dressler's model with the St. Venant equations. Since the "Dressler" equations gave markedly better results, they concluded that "curvature" is quite important. However, the St. Venant equations enforce another simplification that may contribute to the difference - the implementation of the mild-slope assumption. We shall investigate the nature of the discrepancies between the generalized shallow water equations and the St. Venant equations. The standard steep-slope shallow water equations will serve as a means of evaluating this additional assumption in the St. Venant form.

Throughout we will refer to the generalized shallow water equations as with "curvature"; when curvature is set to zero it is termed "no curvature", and imposing the St. Venant equations as "St. Venant." The test input is shown in Table 5.8. The model has the same geometry and node layout as reported in Section 3.5. The flow rate is the highest tested by Sivakumaran. Figure 5.11 shows a comparison of water surface results for each equation set and the flume data. The "curvature" case matches the flume water surface quite well. As in Chapter 3, the "no curvature" case is close to the generalized shallow water equations and the flume data in the supercritical region downstream of the crest, but shows the bulge due to the kinematic inconsistency we have previously discussed.

The water surface solution for the St. Venant equations starts high and drops too quickly. This difference is not due to the hydrostatic assumption

Table 5.8: Spillway form.

Input Parameters	
g	9.81m/sec ²
n	0.0
ν_t	0.0
Δt	0.05sec
Simulation Time	10sec
Iterations	3
ϵ	0.02
Boundary Conditions	
Upstream	
p	0.11197m ³ /s/m
q	0

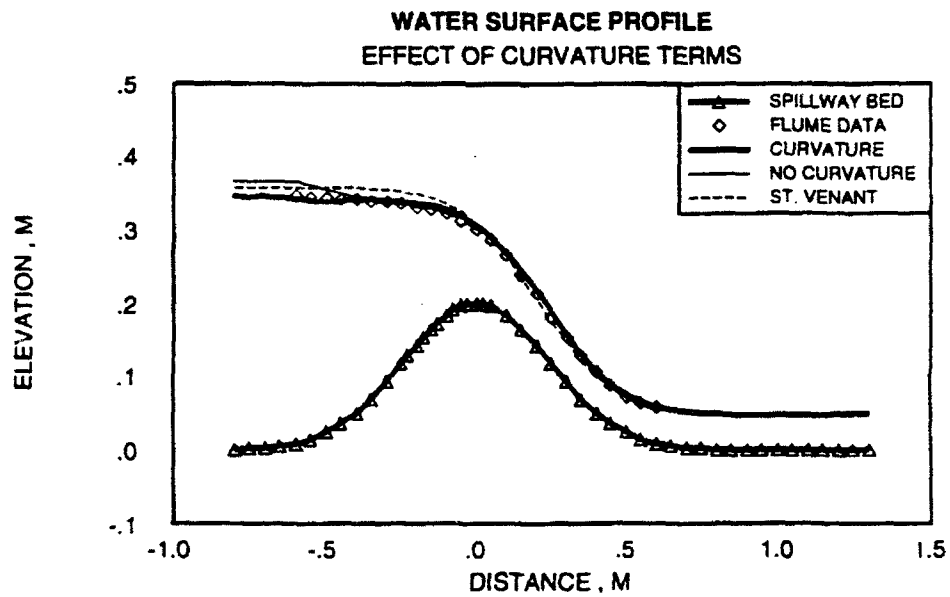


Figure 5.11: Spillway form: comparison of water surface results.

since the "no curvature" case is also hydrostatic. Upstream, the St. Venant equations predict a higher water surface to maintain this flow rate but without the upstream bulge obtained by simply setting curvature to zero in the generalized shallow water equations. The "no curvature" case bulge in a concave region is due to an overestimate of the differential volume. This in turn requires a greater pressure gradient to accelerate the flow. In the St. Venant equations, the depth is measured vertically and this problem is relieved. The St. Venant mild-slope assumption means that depth is measured vertically and we are essentially solving the horizontal equations with a modified gravitational force to account for bed slope.

To examine this mild-slope assumption and its effects upon the solution, we utilize a simple comparison of the St. Venant equations (with the mild-slope assumption) and a steep-slope formulation. The steady-state, one-dimensional, steep-slope shallow water equations may be written:

$$\frac{\partial Q}{\partial s} = 0 \quad (5.4)$$

$$\frac{\partial \left[Q^2/d + \frac{1}{2}gd^2 \cos \theta \right]}{\partial s} + gd \sin \theta = 0 \quad (5.5)$$

and the corresponding St. Venant mild-slope formulation is:

$$\frac{\partial P}{\partial x} = 0 \quad (5.6)$$

$$\frac{\partial \left[P^2/h + \frac{1}{2}gh^2 \right]}{\partial x} + gh \frac{\partial b}{\partial x} = 0 \quad (5.7)$$

where, $Q = vd$ and $P = uh$. All other geometric terms are defined in Figure 5.12. Assuming θ to be a constant, the steep-slope formulation can be written in terms of the variables of the mild-slope formulation and, after solving for

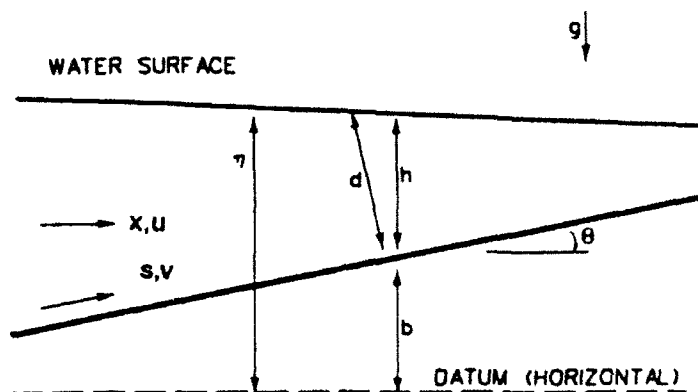


Figure 5.12: Geometry for mild-slope evaluation.

water surface slope $\frac{\partial \eta}{\partial x}$,

$$\frac{\partial \eta}{\partial x} = - \left\{ \frac{P^2 \cos^2 \theta}{gh_o^3 - P^2 \cos^2 \theta} \right\} \frac{\partial b}{\partial x} \quad (5.8)$$

We wish to compare the water surface slope for this steep-slope formulation to that of the St. Venant equations near $h = h_o$. The mild-slope result is obtained by setting $\theta = 0$. There is a slight ambiguity here in that, $\frac{\partial b}{\partial x} = \tan \theta$, but, $\frac{\partial b}{\partial x}$ is actually measured and is not among the terms that are dropped when θ is assumed to be small.

First we consider subcritical flow. For this case the denominator is positive and we rewrite (5.8)

$$\frac{\partial \eta}{\partial x} = - \left\{ \frac{P^2 \cos^2 \theta}{|gh_o^3 - P^2 \cos^2 \theta|} \right\} \frac{\partial b}{\partial x} \quad (5.9)$$

A comparison between the two forms can be made by setting $\theta = 0$ in the above equation for the mild-slope form. Both have water surface slopes that are in the opposite direction of the bed slope. It is also apparent that the

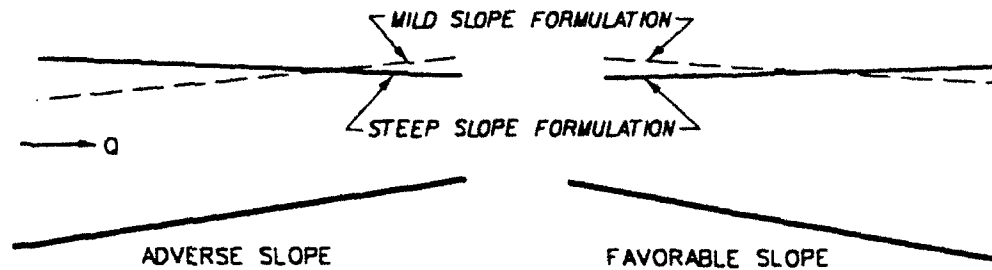


Figure 5.13: Subcritical flow: water surface slope comparison.

magnitude of $\frac{\partial \eta}{\partial x}$ is larger for the mild-slope form. Figure 5.13 shows examples with adverse and favorable bed slopes, and illustrates the relationship between the water surface slope predicted by the two formulations.

For supercritical flow the water surface slope is found to be

$$\frac{\partial \eta}{\partial x} = \left\{ \frac{P^2 \cos^2 \theta}{|gh_o^3 - P^2 \cos^2 \theta|} \right\} \frac{\partial b}{\partial x} \quad (5.10)$$

Here the mild-slope assumption again exaggerates the water surface slope but in the same direction as the bed slope. The same two examples under supercritical conditions are shown in Figure 5.14. The mild-slope assumption used in the St. Venant equations tends to exaggerate water surface slope if the bed slope is steep. The amplification is roughly related to $1/\cos^2 \theta$ times the bed slope. Hence the mild-slope assumption is responsible for the differences on the downstream spillway face in this example, not curvature effects.

A comparison of bed pressures is shown in Figure 5.15. The generalized shallow water equations (curvature case) do a very good job of modeling these pressures as expected, although their result is slightly high near $x = -0.5\text{m}$. This is where the shallowness parameter, (curvature multiplied by

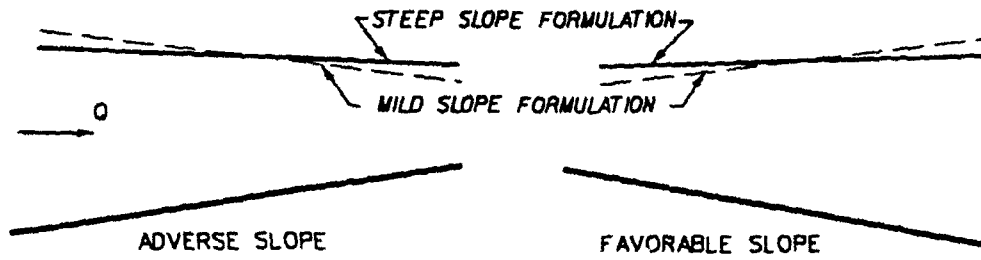


Figure 5.14: Supercritical flow: water surface slope comparison.

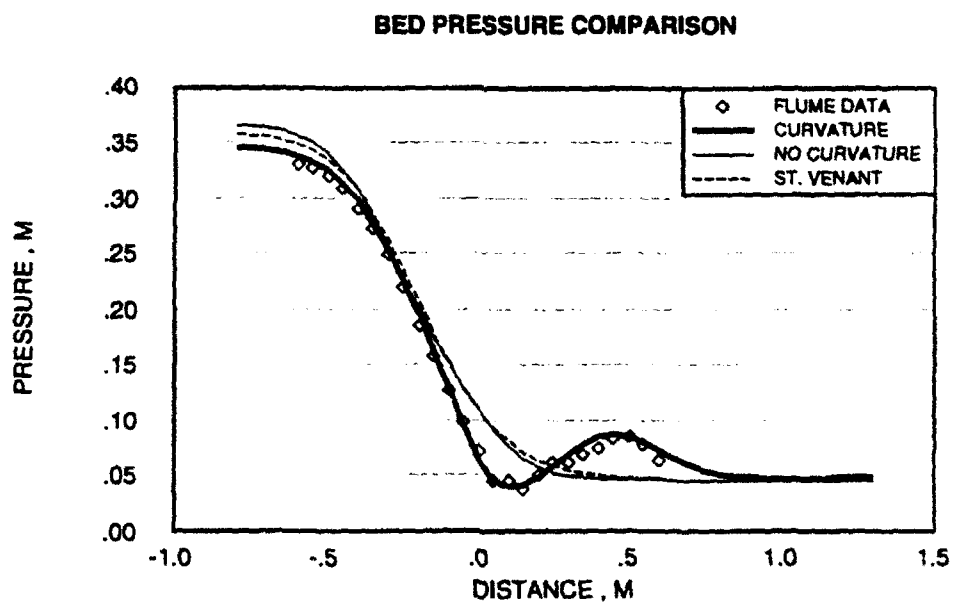


Figure 5.15: Spillway form: comparison of bed pressure results.

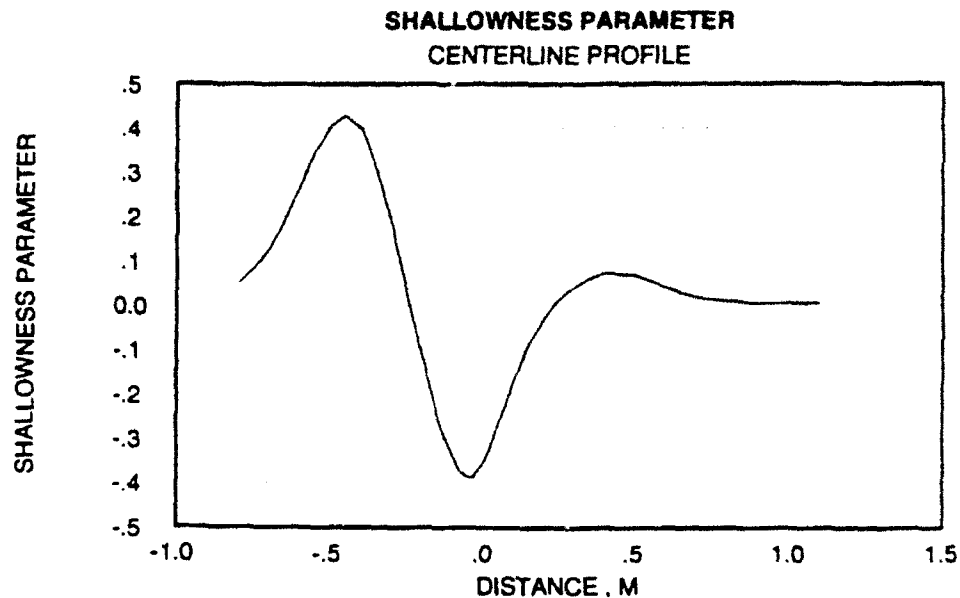


Figure 5.16: Spillway form: shallowness parameter.

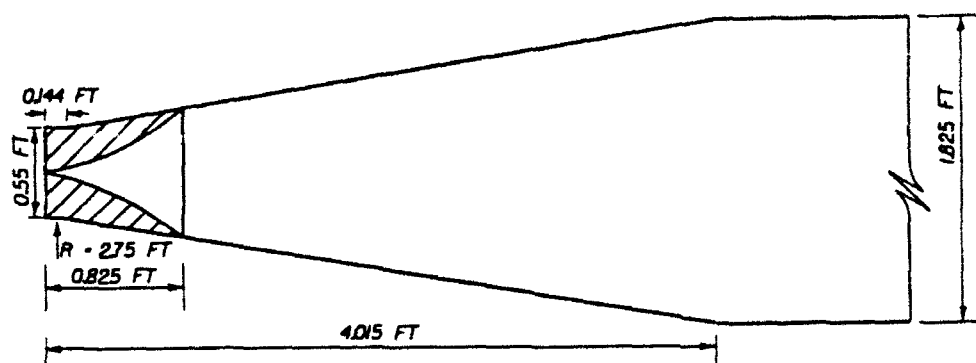
depth), is the greatest. (It reaches a value of about 0.42, see Figure 5.16.) The limit given by Sivakumaran on the applicability of these equations is $-2 \leq \kappa h \leq 0.54$. While 0.42 is certainly within these limits, we must note that the perturbation analysis implies that the water surface “looks” like the bed; i.e., the flow is essentially parallel to the bed. The bed-normal accelerations become more important as this is relaxed. These effects can be accommodated better by going to higher-order terms in the perturbation analysis as long as the shallowness parameter is not too large. This is a serious limitation to applicability of the model to a large class of spillways which typically have a steep upstream face. Downstream, the slight discrepancy near the toe of the spillway has been attributed by Sivakumaran to the irrotational flow assumption (over depth). This is based upon the research of Henderson and Tierney

[28]. Overall, the comparison is quite remarkable. On the other hand, the St. Venant and the "no curvature" cases are poor. This is not surprising since both are hydrostatic and the St. Venant model measures pressure based on depth measured vertically.

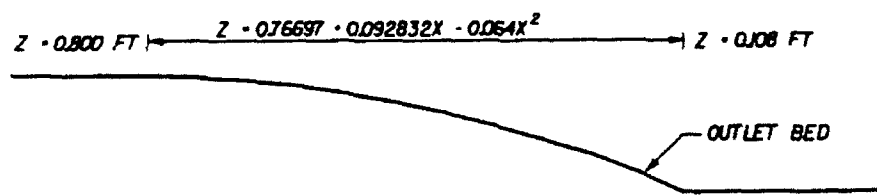
These results indicate that the longitudinal profile of water surface and bed pressure are modeled fairly well with the generalized shallow water equations. The new model is limited in handling some common spillways in which the upstream face is steep. Downstream of the crest, where the flow is supercritical, the water surface more closely parallels the bed and thus the perturbation analysis is more accurate. The "no curvature" case of the generalized shallow water equations also compares well with the flume water surface. This implies that the hydrostatic pressure assumption is reasonable in the downstream supercritical reach. The overall poor comparison with the St. Venant model can be attributed to the mild-slope assumption. The poor spillway capacity prediction is a result of the hydrostatic assumption in the steep-slope and the St. Venant models.

5.2.3 Outletworks Flume.

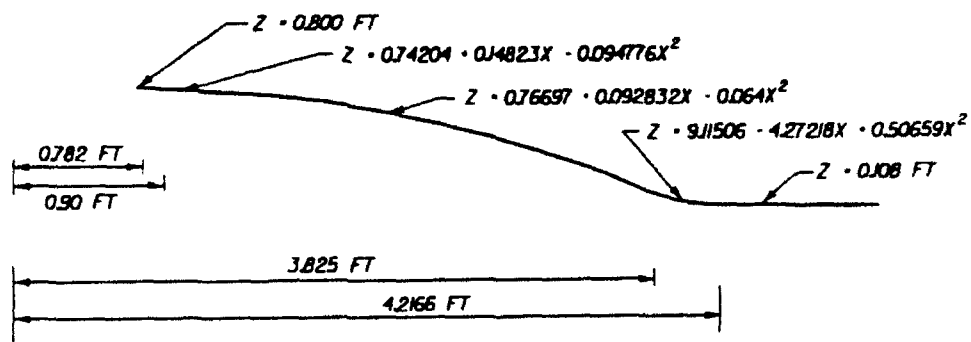
The final test is the most general we shall undertake. We compare the previous sets of model equations to an outletworks physical model at the Waterways Experiment Station, WES. Here our primary concern is the lateral behavior predicted by the mathematical models for more realistic structures. A diagram of the flume, as tested, is shown in Figure 5.17. The plan view geometry for the flume and the model are identical but the numerical approx-



FLUME PLAN VIEW



FLUME ELEVATION VIEW



NUMERICAL MODEL ELEVATION VIEW

Figure 5.17: Outletworks flume: flume and numerical model geometry.

imation to bed elevation has smooth transitions to provide a continuous slope. The dimensions of the flume were chosen such that typical operating conditions place the flow regime within the fully turbulent region. For our test, the Reynolds number is about $R \equiv \frac{uh}{\nu} \approx 200000$, which indicates that scale-effects are small. For even relatively smooth bed and wall conditions the flume will be in the fully turbulent regime (see [48, 13]). Therefore, we might reasonably expect the flume results to exhibit behavior similar to large-scale structures of this type.

The bed elevation of the flume is purposely laid out longitudinally as a parabolic function to minimize flow separation. The actual dimensions in Figure 5.17 are "as measured" and vary slightly from the construction specifications, primarily as a result of settling. The transition from the circular conduit to the apron is fairly complicated. The walls have a slight flair with a radius of 2.75ft and the bed has fillets to move smoothly from the round conduit to the rectangular section of the apron. The apron wall has an outward slope of approximately $\frac{1}{6}$. A level stilling basin which contains baffles and an end sill is located 4.015ft from the conduit exit. These stilling basin features are not numerically modeled here; since these effects far downstream are of lesser importance to the spillway flow. The actual bed elevation numerically modeled (as shown in Figure 5.17) contains no discontinuities in slope so that the curvature exists throughout. The bed is flat in the lateral direction, i.e., all slope and curvature variations are in the longitudinal direction.

The flume water surface is recorded every 0.05ft laterally and every 0.10ft longitudinally. An additional reading is made near the sidewalls (typically within 0.02ft). The measurements are recorded with a point gage capable

of measuring to a precision of 0.001ft (it is graduated in 0.01 ft units and with a vernier one can detect 0.001 changes). In reality the water surface is quite rough and time varying, so that readings are approximately accurate to about 0.02ft. The flow rate is measured using a 12 by 6 inch venturi meter with a differential manometer. The inflow pressure is maintained by a constant head tank. The manometer calibration is checked using direct measurements of volume change in a specific time period. The discharge is estimated [57] to be accurate within 3 %.

The flume water surface results are shown in Figure 5.18 as a three-dimensional perspective for a flow rate of 2.56 cfs (cubic feet per second). The view shows the lateral hump in the water surface as the flow exits the outlet conduit. This eventually spreads to a relatively uniform depth as intended in the design. If, however, flow becomes focussed the result will be circulation in the stilling basin with possible damage there. The nonuniform velocity field would also cause more downstream erosion. The drag of the apron sidewalls causes the sharp rise in water surface. The buildup in water depth along the sides of the stilling basin is a result of the change in side slopes.

The numerical model is constructed of 408 nodes and 368 elements (see Figure 5.19). It extends longitudinally from $x = 0.75\text{ft}$ to $x = 6.0\text{ft}$. The upstream boundary is therefore below the complex geometry of the fillets near the conduit exit and the vertical velocity profile should be closer to an open-channel flow distribution. The flow is supercritical throughout the study reach, and at the upstream boundary the velocity and depths are specified. The depths are the flume results interpolated from the 0.70ft and 0.80ft ranges. The x component velocity distribution is assumed to be uniform across

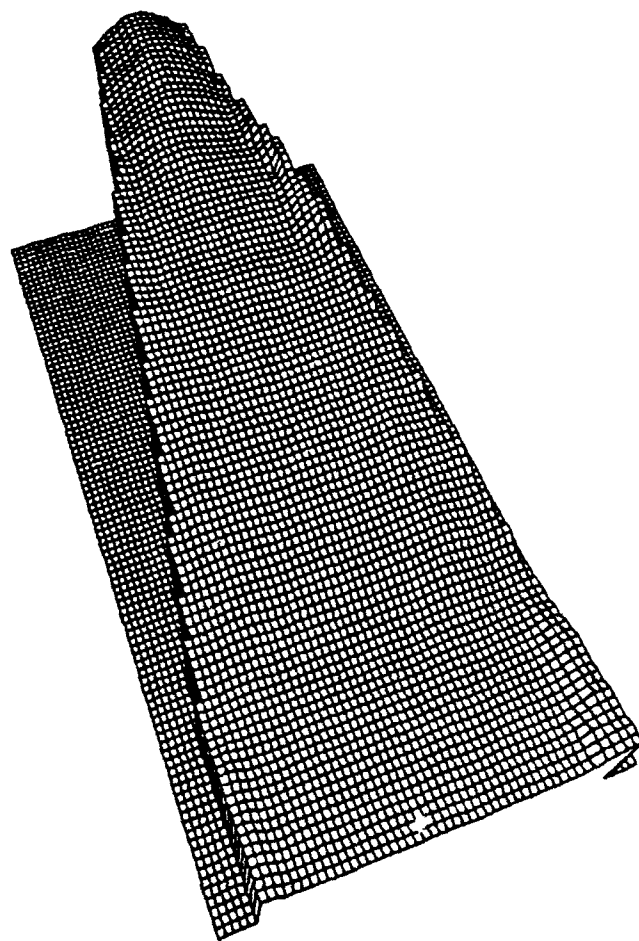


Figure 5.18: Outletworks flume: water surface results, perspective view.

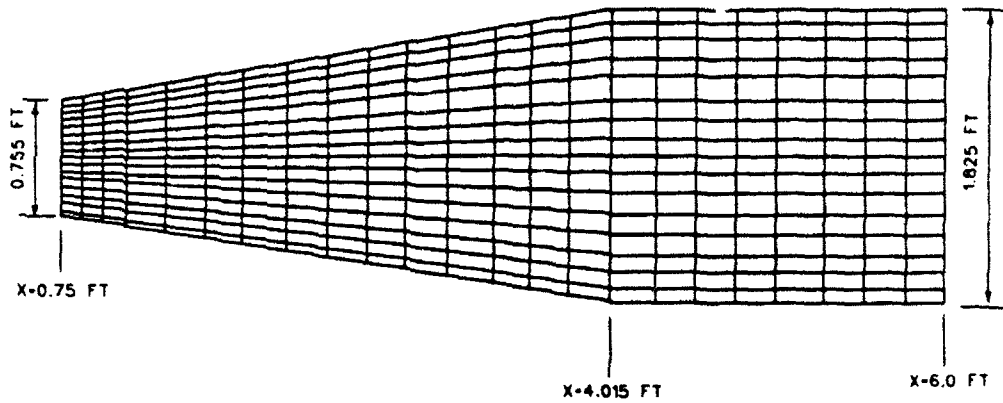


Figure 5.19: Outletworks model: computational mesh.

the upstream boundary. The lateral velocity component at the inlet is specified so that the flow is tangent to the sidewalls and zero in the channel center with linear variation between these stations. These are the simplest reasonable boundary conditions and should be suitable for a comparison of model equations. Furthermore, this is as much information as a modeler typically has to make a site-specific study. Other model conditions are shown in Table 5.9. The

Table 5.9: Outletworks model.

Input Parameters	
g	32.208ft/sec ²
n	0.012
ν_t	0.05ft ² /sec
Δt	0.05sec
Simulation Time	15sec
Iterations	3
ϵ	0.03

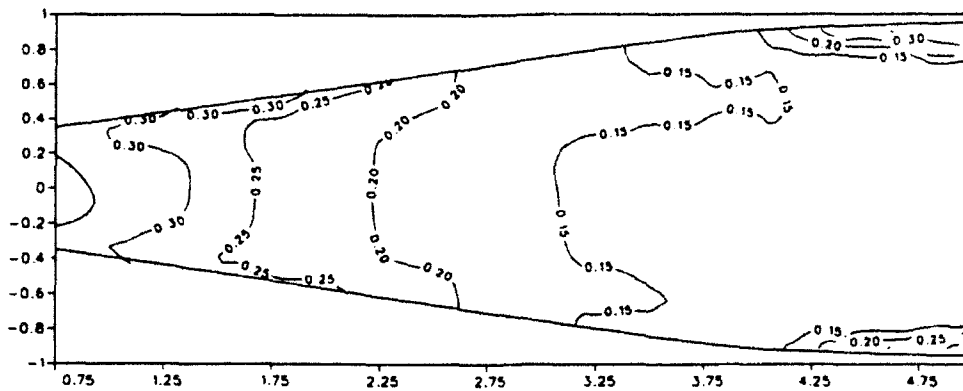


Figure 5.20: Outletworks flume: depth contours.

turbulent viscosity corresponds to a value of C_B of about 0.1.

Figures 5.20 - 5.23 show the depth contours for the flume; the generalized shallow water equations, the standard steep-slope shallow water equations, and the St. Venant equations. The flume and St. Venant measurements are made vertically as water surface elevations which we have converted to depths normal to the bed. The flume data in the upper region reveal a continuation of the conduit shape, i.e., a hump in the water surface with the centerline being a relative maximum. This form ends near $x = 1.75\text{ft}$. From there on the centerline is a relative minimum or the surface is nearly flat. This is the desired pattern for a good hydraulic design. At the channel edges the wall drag causes a substantial buildup of water depth.

A most important result of the generalized shallow water equations is the more gradual lateral spread of the flow tube. As an illustration, within the portion of the flume modeled here, the flume shows the centerline to be a relative maximum for about 1.0ft. The model including curvature gave a

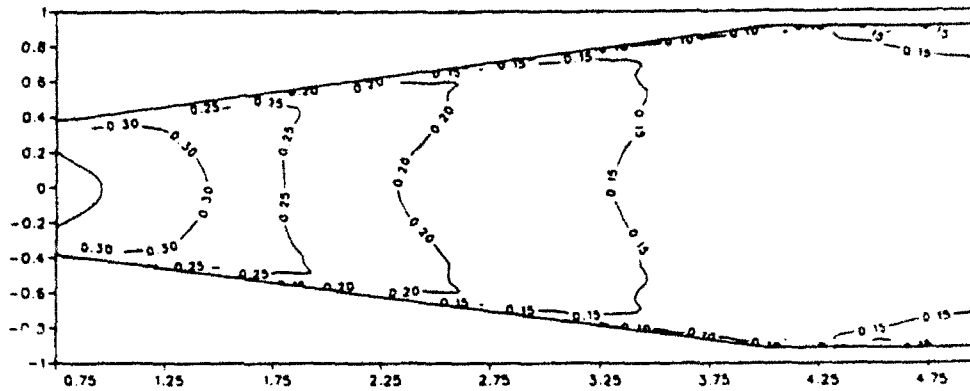


Figure 5.21: Outletworks model: generalized shallow water equations. depth contours.

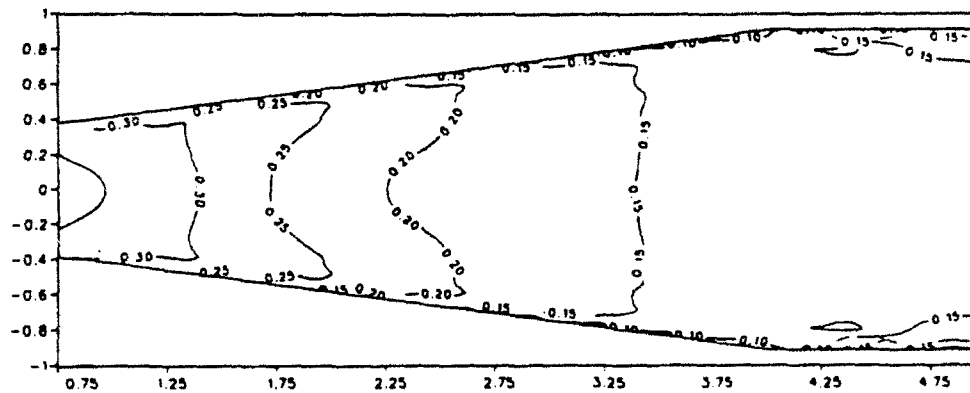


Figure 5.22: Outletworks model: standard steep-slope shallow water equations. depth contours.

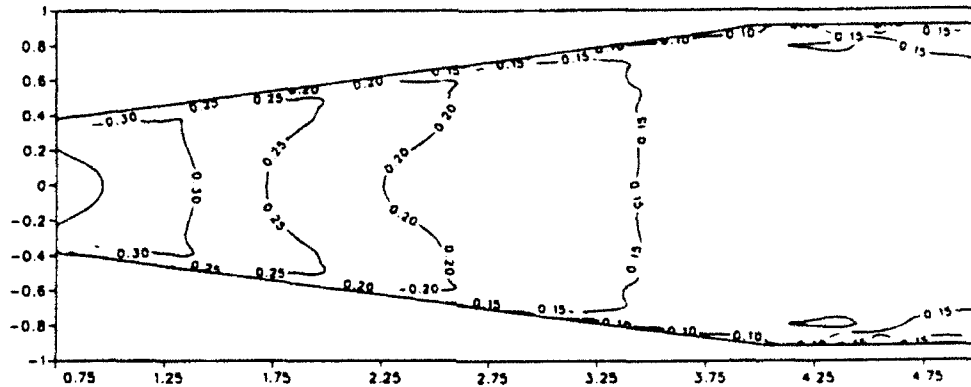


Figure 5.23: Outletworks model: St. Venant equations, depth contours.

similar length. The steep-slope shallow water model (no curvature) and the St. Venant equations are nearly identical throughout the domain. The length for which the centerline is a maximum as predicted by these models is only about 0.7ft. Hence, the nonhydrostatic component has a definite effect upon the wave speed here. This is a region in which the flow is entirely supercritical and for which our one-dimensional test showed little improvement by including the nonhydrostatic pressure component in the generalized shallow water equations. However, now the lateral variation is strongly dependent upon the nonhydrostatic contribution. The predicted wave celerity for a similar case in which the curvature and dominant flow direction are along the x axis can be shown (see [20]) to be

$$c_{gswc} = \left\{ -\frac{\log(1 - \kappa_1 h)}{(1 - \kappa_1 h) \kappa_1} \left[g_3 + \frac{\kappa_1 \hat{u}^2}{(1 - \kappa_1 h)^3} \right] \right\}^{\frac{1}{2}} \quad (5.11)$$

On the other hand the celerity without curvature included is simply

$$c_{sswc} = (g_3 h)^{\frac{1}{2}} \quad (5.12)$$

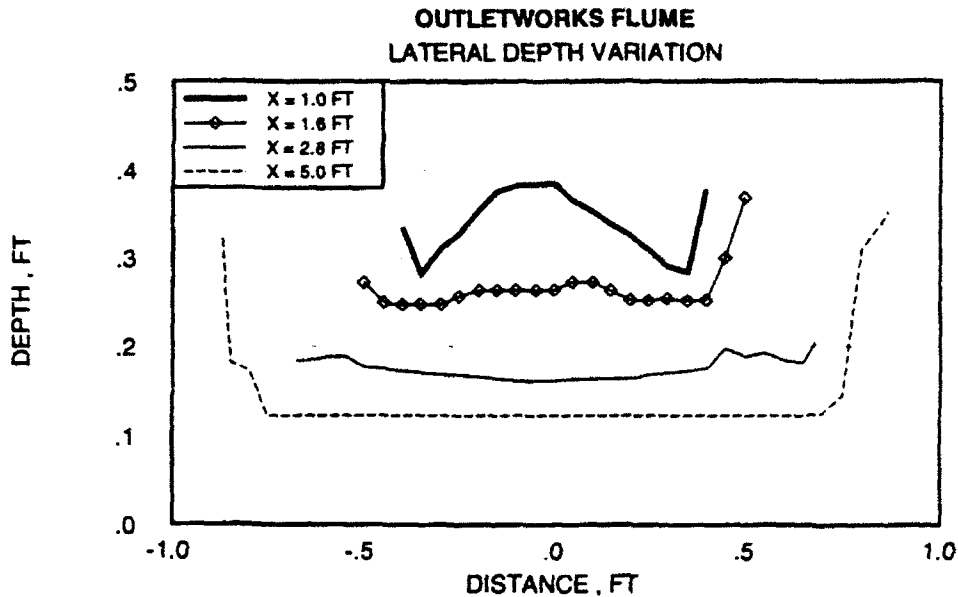


Figure 5.24: Outletworks flume: lateral depth profiles.

A convex curvature (κ_1 negative) produces a lower celerity in the generalized equations which is not captured in the standard shallow water equations. The true solution, which includes nonhydrostatic pressure contributions as a result of short wavelengths in addition to bed curvature effects, has a wave celerity that is even smaller than the generalized equations predict. In a concave region (positive curvature) the wave celerity predicted by the generalized shallow water equations will be greater than from the standard shallow water equations.

Lateral profiles of depth are shown in Figures 5.24-5.26. The figures include flume, generalized shallow water, and standard steep-slope shallow water results. The St. Venant results are nearly identical to the standard steep-slope results. The lateral profiles are at distances downstream of the conduit of 1.0, 1.6, 2.8, and 5.0ft. These results provide an additional view of the infor-

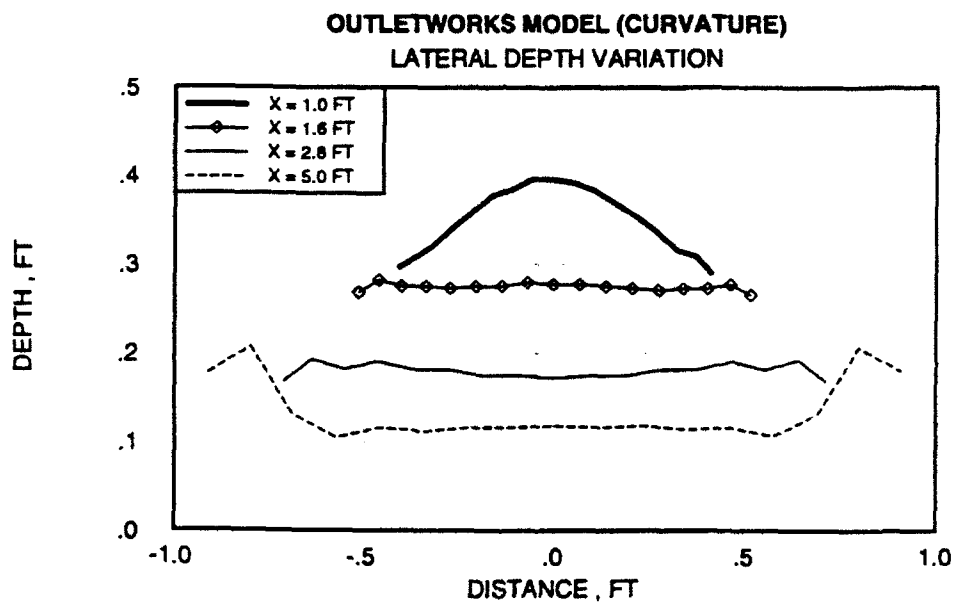


Figure 5.25: Outletworks model: generalized shallow water equations, lateral depth profiles.

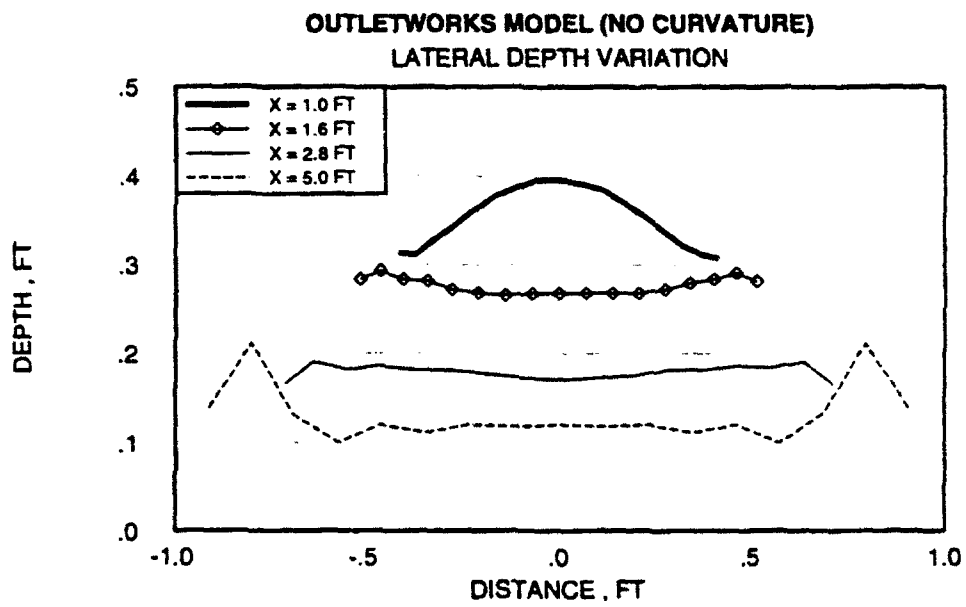


Figure 5.26: Outletworks model: standard steep-slope shallow water equations, lateral depth profiles.

mation contained in the contour plots. Between 1.0ft and 1.6ft the flume and model including curvature effects show a gradual collapse of the wave. With no curvature effects the wave has propagated out to the edges leaving a trough in the center. Downstream, the distinction between the results from the two model equation sets is very small. The model in both cases only captures the behavior of the flume in a qualitative sense. One reason is that we use actual flume measurements for the water surface upstream boundary condition, but rely upon a uniform velocity profile. A second reason is that the wavelength of the hump in the channel center is only about 1ft while the the depth is nearly 0.4ft. This collapse rate is really a short-wave phenomenon not capable of being accurately represented by a long-wave model. However, the effects of the bed curvature are captured and do improve the comparison in the generalized shallow water model.

The lateral velocity profile comparisons between the generalized shallow water equations and the standard steep-slope shallow water equations are shown in Figures 5.27-5.30. The distinctive differences in these figures occur at $x = 1.0\text{ft}$ and $x = 2.8\text{ft}$. At $x = 1.0\text{ft}$ the pressure is lower for the case with curvature, and since velocity is dependent upon the pressure gradient, the lateral velocity is lower. At $x = 2.8\text{ft}$, the model with curvature produces generally higher lateral velocities. The outward propagation of the lateral wave is quicker in the "no curvature" case and the peak has propagated out to the wall, whereas, for the case including curvature, the outer depth has not reached its peak. The result is a reduced adverse gradient at this point in the generalized equations, and thus slightly larger outward velocity.

The mild-slope assumption made little difference for this case; i.e., the

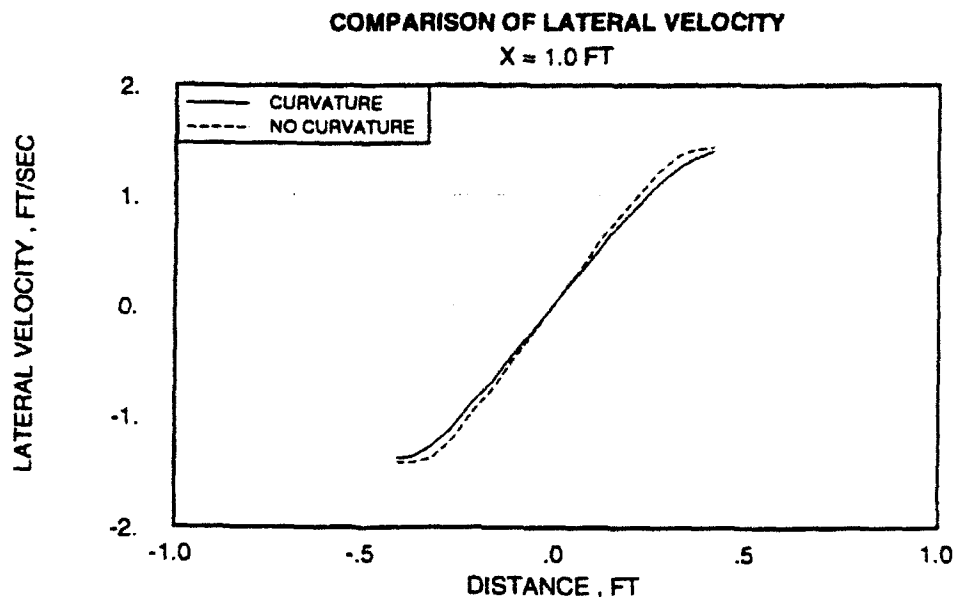


Figure 5.27: Outletworks flume: lateral velocity profiles, $x = 1.0$ ft.

St. Venant equations yielded results quite close to those of the standard steep-slope equations. On the other hand the bed curvature effects are important and the generalized shallow water equations did give better results for the water surface distribution. However, the primary concerns around an outletworks are related to the spread of the flow tube which is a short-wave phenomena and none of the models performed well in this regard.

5.3 Discussion

The most striking contrast between results of the generalized shallow water equations and the other formulations is in the predictions of spillway capacity. This is indeed a result of the hydrostatic pressure distribution used

in the standard equations. In reality the negative curvature near the crest of the spillway reduces the pressure and so allows more flow for a given water level. We shall develop an understanding of this by considering a linearization of the generalized shallow water equations that will allow us to estimate spillway capacity for the standard methods and the change expected by implementation of the generalized shallow water equations.

Consider the discharge per unit width (for a one-dimensional flume) as defined in the generalized shallow water equations to be given by

$$q_w = \int_0^h u(s_3) ds_3 \quad (5.13)$$

or,

$$q_w = -u_h f(h) \frac{\log f(h)}{\kappa} \quad (5.14)$$

where, u_h is the velocity at the surface and as before $f(h) = 1 - \kappa h$. The specific energy is given by

$$E_s = \frac{u_h^2}{2g} + h \quad (5.15)$$

This is the energy at the surface with the datum at the spillway crest. We wish to compare the spillway capacity as determined by the specific energy with curvature and for no curvature. The "no curvature" case corresponds to the St. Venant model and the standard steep-slope shallow water equations. For a given discharge the specific energy is a minimum at the spillway crest. We can see this by considering an idealized flow in a subcritical channel. Across the channel is a "bump" that is originally of very small height. Now as we gradually raise the height of the bump a choke point is eventually reached where any further increase in the "bump" height will cause the upstream water surface to

rise. Additional energy is required to pass this flow for any additional increase in height. Also, downstream of the bump the flow is no longer subcritical. So at the crest of the bump the flow is termed critical and the specific energy is a minimum.

Now using equations 5.14 and 5.15 for $\chi = \kappa h_o$ and $|\chi| \ll 1$, where h_o is a nominal value of h , an approximation for specific energy is

$$E_s \approx \frac{q_w^2}{2gh^2} (1 + \chi) + h \quad (5.16)$$

Minimizing, we find h_c , the critical depth

$$h_c \approx \left[\frac{q_w^2}{g} (1 + \chi) \right]^{\frac{1}{3}} \quad (5.17)$$

or in terms of specific energy

$$E_s \approx \frac{3}{2} \left[\frac{q_w^2}{g} (1 + \chi) \right]^{\frac{1}{3}} \quad (5.18)$$

This demonstrates that if $\chi < 0$, as it would be near the crest the specific energy is less than for the no curvature case, $\chi = 0$. Therefore, we would expect the St. Venant model and other models not including bed curvature to underestimate spillway capacity.

If we solve for the discharge in terms of the required specific energy we obtain the spillway capacity. The ratio q_r of discharge without curvature terms to that with curvature included is approximated by

$$q_r \approx (1 + \chi)^{\frac{1}{2}} \quad (5.19)$$

as demonstrated in Figure 5.31.

Hence we see that near the crest the curvature terms are very important. Models not including this nonhydrostatic effect will overestimate critical depth and underestimate spillway capacity. As shown in Figure 5.31 this can be significant. The two-dimensional model can treat this along with the side constrictions to capture the spillway capacity more accurately.

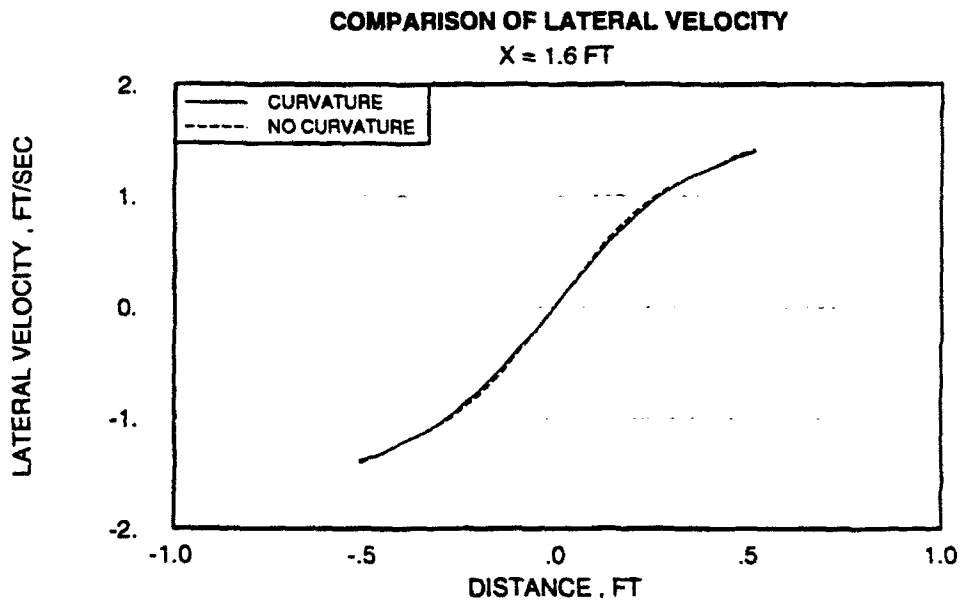


Figure 5.28: Outletworks flume: lateral velocity profiles, $x = 1.6\text{ft}$.

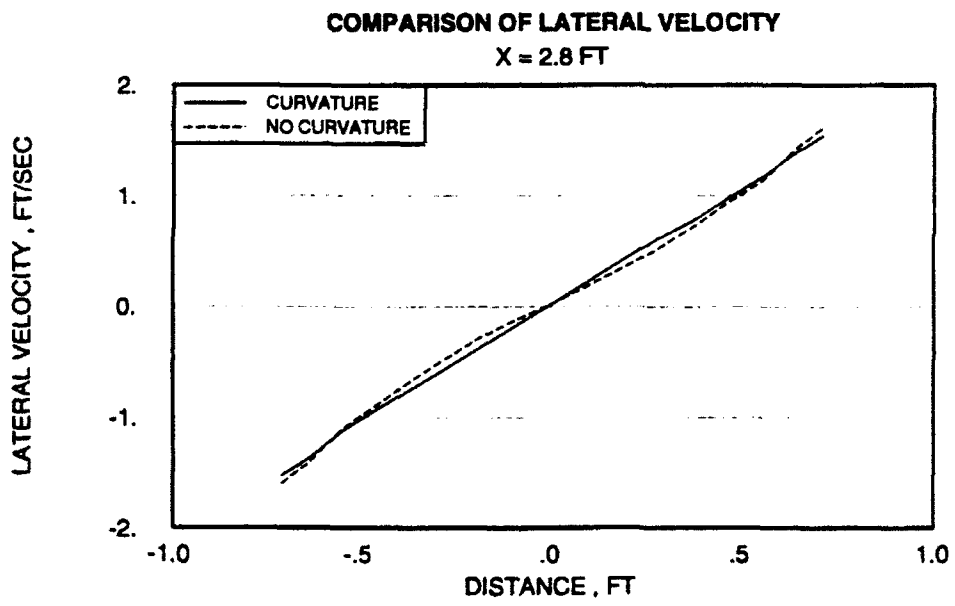


Figure 5.29: Outletworks flume: lateral velocity profiles, $x = 2.8$ ft.

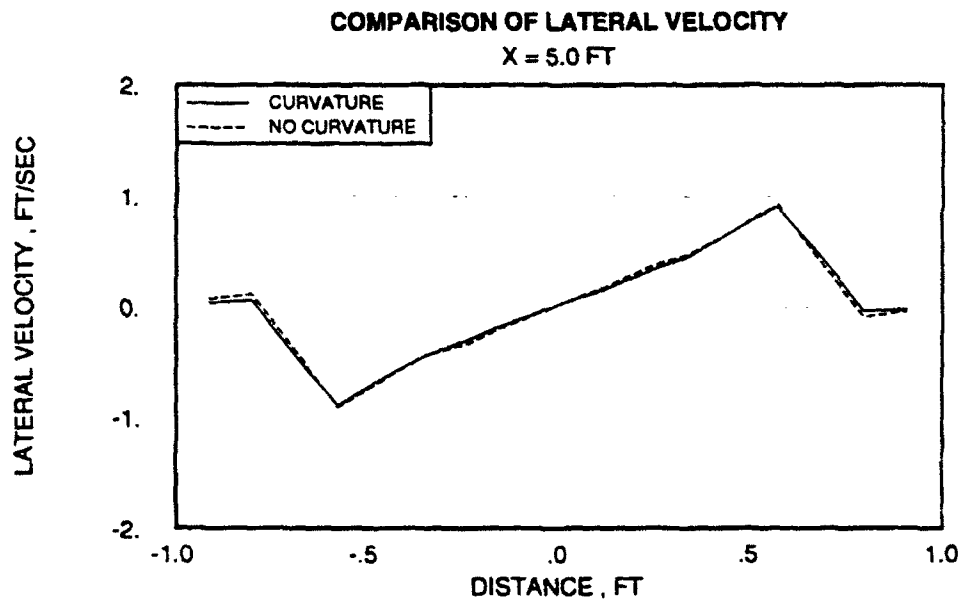


Figure 5.30: Outletworks flume: lateral velocity profiles, $x = 5.0$ ft.

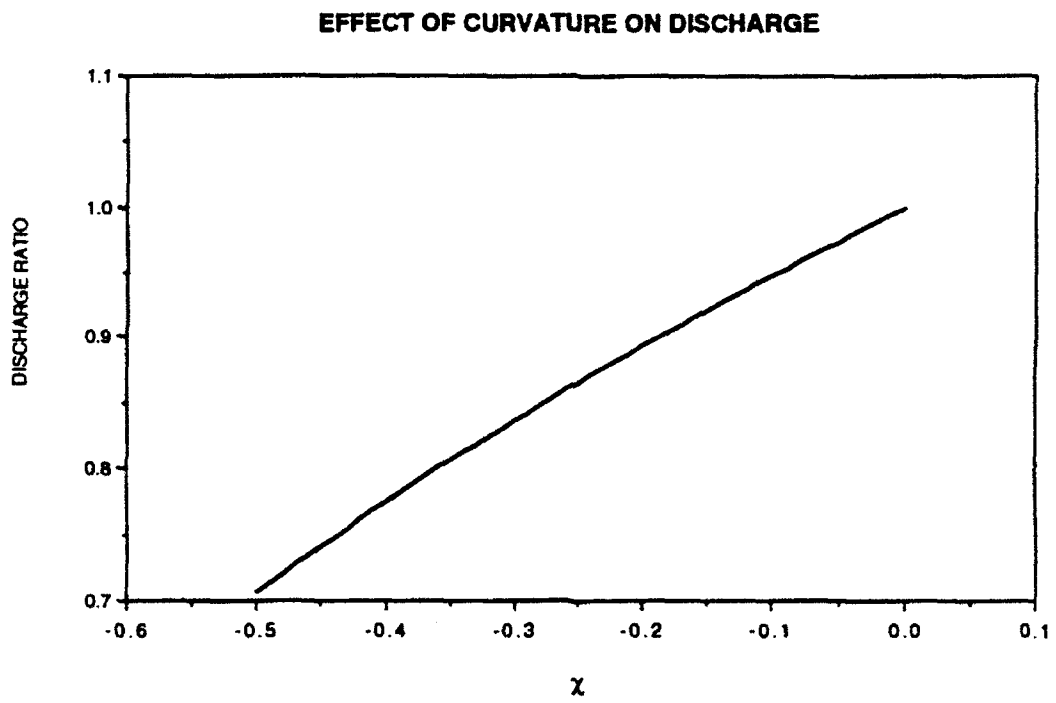


Figure 5.31: Spillway capacity ratio.

Chapter 6

Conclusion

In this investigation we have developed a generalized shallow water equation set to reproduce free-surface flow over curved beds and applied the model to spillway flows. These generalized shallow water equations include bed curvature effects, are nonhydrostatic, and are two-dimensional. The equations are derived via a perturbation expansion in a shallowness parameter. A significant assumption made in this derivation is that the flow is irrotational about axes parallel to the plane of the bed. However, there is no limitation on vorticity about axes normal to the bed.

A one-dimensional model was constructed to assess numerical problems and determine additional needs for the final two-dimensional investigation. This finite element model was straightforward and employed time-lagging of nonlinear terms. We considered available flume data for a simple curved bed profile. In comparing the one-dimensional equations with and without curvature the principal differences occurred upstream of the spillway crest. This is important since this is the spillway capacity.

The numerical handling of the convection terms used a method of artificial viscosity weighted by the convection velocity. At first a Taylor Weak Form approach was attempted but was shown to have some difficulty near points of transition from supercritical to subcritical regimes and vice versa.

The artificial viscosity avoided these problems but also has some detractions and was replaced in the final two-dimensional model. (One obvious problem with the viscosity approach is adding diffusion terms to the mass conservation equation.)

The final development involved a two-dimensional model in which the nonlinear terms were addressed via a Newton Raphson technique, iterating at each time step. This allows larger time steps. We introduced a Petrov Galerkin scheme based on the SUPG idea and λ -schemes in which the test function is weighted using the eigenvalues of the convection matrices.

A two stage testing program was conducted. The first stage validated the discrete model against analytic benchmark cases and the second stage compared the model results to flume data. The first stage was accomplished by several one-dimensional tests performed along the s_1 and then along s_2 directions. These tests were for both constant and variable curvature. The Bernoulli equation served as the standard for comparison. This validated the discrete model for the derived equations.

Tests of the suitability of the equations were then undertaken by comparison to actual flume data. The first study was a comparison to a supercritical transition in which there was no bed curvature. This was primarily a test of the numerical scheme and boundary condition implementation. The model performed well within the limitations of the shallow water equations.

The next set of tests was made for a curved bottom flume with straight walls. Results from the generalized shallow water equations compared remarkably well to the flume water surface data. The spillway capacity was accurately

captured and a comparison of bed pressure was quite good. The St. Venant and the standard steep-slope shallow water equations missed the spillway capacity, both predicting a greater water surface elevation to attain the steady discharge. (The hydrostatic pressure assumption misses the reduction in pressure caused by the uplift of the flow over the curved crest. This is responsible for the error in spillway capacity.)

Along the downstream face the standard steep-slope formulation compared fairly well with the generalized shallow water equations and flume data. The St. Venant equations predicted too steep a water surface slope. This was shown to be a result of the mild-slope assumption, and not curvature related. The principal improvement of the new equations over the "no curvature case" is in the neighborhood of the spillway crest.

We collected experimental data on a flume at the Waterways Experiment Station designed to study outlet works. Here the emphasis was upon lateral variations in water surface. The improvement offered by the new equations was subtle showing slower (and more realistic) spread of the flow conduit over negative curvature regions. Overall, however, the representation of what is essentially a short wave phenomena was weak. However, the results did provide a qualitative picture of the flow that is beneficial for designers.

A list of the conclusions then is as follows:

1. These equations are a significant improvement over standard steep-slope shallow water equations in the vicinity of the spillway crest. Within the stated restrictions on the size of curvature and depth, these equations can provide a good representation of spillway capacity.

2. These equations do show an improvement in the lateral depth distribution though they are shallow water equations and suffer in predicting phenomena associated with short wavelengths.
3. Along the downstream face of the spillway or outlet channel the flow is supercritical and the difference in water surface attributable to curvature is small, generally on the order of precision used in physical model flumes.
4. The St. Venant equations proved to be much worse than the generalized or the standard steep-slope shallow water equations along the downstream face. The difference, however, is attributable to the mild-slope assumption and not to the hydrostatic pressure assumption or other curvature manifestations.

Recommendations for Future Work

The equations are most important in the region around the spillway crest and for evaluation of contraction effects near the ends of the spillway. This is where the nonhydrostatic pressure distribution is most critical. Future research should concentrate on this issue. Furthermore:

1. Many spillways have steep faces and abrupt curvature that violate the limits imposed by the shallowness condition in this perturbation expansion. This significantly reduces the pressure at the crest and so increases spillway capacity. To be a practical tool, the model needs to be extended to this more general case, perhaps by the calculation of a flow line representing the bed.

2. Higher-order terms in the expansion for the steep-slope shallow water equations can also be constructed for this region. In particular, do these equations represent this region as well as the generalized shallow water equations? Of course, these Boussinesq equations include third-order spatial derivatives and so will require additional computational effort and some improved convection scheme.
3. The unsteady behavior of the equations could be quite interesting. In fact, even for steady boundary conditions the highly nonlinear flow near and along the spillway face is unsteady.

Appendix

Integration of Coefficients

The integration of the coefficients used in the generalized shallow water equations was accomplished using the software *Mathematica* [43] and are as follows:

$$\begin{aligned} a_1 &= \int_0^h f_2(s_3) ds_3 \\ &= hf_2(h/2) \\ a_2 &= \int_0^h \frac{f_2(s_3)}{(f_1(s_3))^2} ds_3 \\ &= \frac{(\kappa_1 - \kappa_2)h}{\kappa_1 f_1(h)} - \frac{\kappa_2 \log f_1(h)}{\kappa_1^2} \\ a_3 &= \int_0^h \frac{1}{f_2(s_3)} ds_3 \\ &= -\frac{\log f_2(h)}{\kappa_2} \\ a_4 &= \int_0^h s_3 f_2(s_3) ds_3 \\ &= \frac{1}{2} h^2 f_2(2h/3) \\ a_5 &= \int_0^h \frac{s_3}{(f_1(s_3))^2} ds_3 \\ &= \frac{1}{\kappa_1^2} \left[\frac{\kappa_1 h}{f_1(h)} + \log f_1(h) \right] \\ a_6 &= \int_0^h \frac{s_3}{(f_2(s_3))^2} ds_3 \\ &= \frac{1}{\kappa_2^2} \left[\frac{\kappa_2 h}{f_2(h)} + \log f_2(h) \right] \end{aligned}$$

$$\begin{aligned}
a_7 &= \int_0^h f_1(s_3) f_2(s_3) ds_3 \\
&= h - \frac{1}{2}(\kappa_1 + \kappa_2)h^2 + \frac{1}{3}\kappa_1\kappa_2h^3 \\
a_8 &= \int_0^h \frac{s_3}{f_1(s_3) f_2(s_3)} ds_3 \\
&= \frac{1}{\kappa_1 - \kappa_2} \left[\frac{\log f_1(h)}{\kappa_1} - \frac{\log f_2(h)}{\kappa_2} \right] \\
a_9 &= \int_0^h \frac{1}{(f_1(s_3))^2} \int_0^{s_3} \frac{f_2(\xi)}{f_1(\xi)} d\xi ds_3 \\
&= \frac{1}{\kappa_1^2 f_1(h)} \left[-\kappa_1 h - \log f_1(h) + \frac{2\kappa_2}{\kappa_1} (\kappa_1 h + f_1(h/2) \log f_1(h)) \right] \\
a_{10} &= \int_0^h \frac{1}{(f_1(s_3))^2} \int_0^{s_3} \frac{\xi}{f_1(\xi)} d\xi ds_3 \\
&= \frac{2(\kappa_1 h + f_1(h/2) \log f_1(h))}{\kappa_1^3 f_1(h)} \\
a_{11} &= \int_0^h \frac{1}{(f_1(s_3))^2} \int_0^{s_3} \frac{\xi f_2(\xi)}{(f_1(\xi))^2} d\xi ds_3 \\
&= \frac{h^2}{2\kappa_1 f_1(h)^2} + \frac{\kappa_1 h + \log f_1(h)}{\kappa_1^3 f_1(h)} \\
&\quad - \frac{\kappa_2}{\kappa_1^3} \left[\frac{2h}{f_1(h)} + \frac{(2h - \kappa_1 h^2)}{2f_1(h)^2} + \frac{\log f_1(h)}{\kappa_1} + \frac{2 \log f_1(h)}{\kappa_1 f_1(h)} \right] \\
a_{12} &= \int_0^h \frac{1}{(f_1(s_3))^2} \int_0^{s_3} \frac{f_1(\xi)}{f_2(\xi)} d\xi ds_3 \\
&= \frac{1}{\kappa_1 \kappa_2 f_1(h)} \left[\kappa_1 h + f_1(h) \log f_1(h) \right. \\
&\quad \left. + \frac{\kappa_1}{\kappa_2} f_2(h) \log f_2(h) - f_1(h) \log f_1(h) \right] \\
a_{13} &= \int_0^h \frac{1}{(f_1(s_3))^2} \int_0^{s_3} \frac{\xi}{f_2(\xi)} d\xi ds_3 \\
&= \frac{1}{\kappa_1 \kappa_2 f_1(h)} \left[\frac{\kappa_1 h + f_1(h) \log f_1(h)}{\kappa_1} \right. \\
&\quad \left. + \frac{(-\kappa_2 f_1(h) \log f_1(h) + \kappa_1 f_2(h) \log f_2(h))}{\kappa_2 (\kappa_1 - \kappa_2)} \right]
\end{aligned}$$

$$\begin{aligned}
a_{14} &= \int_0^h \frac{1}{(f_1(s_3))^2} \int_0^{s_3} \frac{\xi f_1(\xi)}{(f_2(\xi))^2} d\xi ds_3 \\
&= \left[\frac{h}{(\kappa_1 - \kappa_2) f_1(h)} + \frac{\log f_1(h) - \log f_2(h)}{(\kappa_1 - \kappa_2)^2} \right] \left[\frac{1}{\kappa_2} - \frac{\kappa_1}{\kappa_2^2} \right] \\
&\quad - \frac{\kappa_1}{\kappa_2^2} \left[\frac{h}{\kappa_1 f_1(h)} + \frac{\log f_1(h)}{\kappa_1^2} \right] \\
&\quad - \left[\frac{\kappa_2 - 2\kappa_1}{\kappa_1 \kappa_2^3} \right] \left[\frac{\kappa_2 (\log f_1(h) - \log f_2(h))}{(\kappa_1 - \kappa_2)} - \frac{\log f_2(h)}{f_1(h)} \right]
\end{aligned}$$

$$\begin{aligned}
b_1 &= \int_0^h f_1(s_3) ds_3 \\
&= h f_1(h/2)
\end{aligned}$$

$$\begin{aligned}
b_2 &= \int_0^h \frac{f_1(s_3)}{(f_2(s_3))^2} ds_3 \\
&= \frac{(\kappa_2 - \kappa_1) h}{\kappa_2 f_2(h)} - \frac{\kappa_1 \log f_2(h)}{\kappa_2^2}
\end{aligned}$$

$$\begin{aligned}
b_3 &= \int_0^h \frac{1}{f_1(s_3)} ds_3 \\
&= \frac{\log f_1(h)}{\kappa_1}
\end{aligned}$$

$$\begin{aligned}
b_4 &= \int_0^h s_3 f_1(s_3) ds_3 \\
&= \frac{1}{2} h^2 f_1(2h/3)
\end{aligned}$$

$$\begin{aligned}
b_5 &= \int_0^h \frac{s_3}{(f_2(s_3))^2} ds_3 \\
&= a_6
\end{aligned}$$

$$\begin{aligned}
b_6 &= \int_0^h \frac{s_3}{(f_1(s_3))^2} ds_3 \\
&= a_5
\end{aligned}$$

$$\begin{aligned}
b_7 &= \int_0^h f_1(s_3) f_2(s_3) ds_3 \\
&= a_7
\end{aligned}$$

$$b_8 = \int_0^h \frac{s_3}{f_1(s_3) f_2(s_3)} ds_3$$

$$\begin{aligned}
&= a_8 \\
b_9 &= \int_0^h \frac{1}{(f_2(s_3))^2} \int_0^{s_3} \frac{f_1(\xi)}{f_2(\xi)} d\xi ds_3 \\
&= \frac{1}{\kappa_2^2 f_2(h)} \left[-\kappa_2 h - \log f_2(h) + \frac{2\kappa_1}{\kappa_2} (\kappa_2 h + f_2(h/2) \log f_2(h)) \right] \\
b_{10} &= \int_0^h \frac{1}{(f_2(s_3))^2} \int_0^{s_3} \frac{\xi}{f_2(\xi)} d\xi ds_3 \\
&= \frac{2(\kappa_2 h + f_2(h/2) \log f_2(h))}{\kappa_2^3 f_2(h)} \\
b_{11} &= \int_0^h \frac{1}{(f_2(s_3))^2} \int_0^{s_3} \frac{\xi f_1(\xi)}{(f_2(\xi))^2} d\xi ds_3 \\
&= \frac{h^2}{2\kappa_2 f_2(h)^2} + \frac{\kappa_2 h + \log f_2(h)}{\kappa_2^3 f_2(h)} \\
&\quad - \frac{\kappa_1}{\kappa_2^3} \left[\frac{2h}{f_2(h)} + \frac{(2h - \kappa_2 h^2)}{2f_2(h)^2} + \frac{\log f_2(h)}{\kappa_2} + \frac{2 \log f_2(h)}{\kappa_2 f_2(h)} \right] \\
b_{12} &= \int_0^h \frac{1}{(f_2(s_3))^2} \int_0^{s_3} \frac{f_2(\xi)}{f_1(\xi)} d\xi ds_3 \\
&= \frac{1}{\kappa_2 \kappa_1 f_2(h)} [\kappa_2 h + f_2(h) \log f_2(h) \\
&\quad + \frac{\kappa_2}{\kappa_1} f_1(h) \log f_1(h) - f_2(h) \log f_2(h)] \\
b_{13} &= \int_0^h \frac{1}{(f_2(s_3))^2} \int_0^{s_3} \frac{\xi}{f_1(\xi)} d\xi ds_3 \\
&= \frac{1}{\kappa_2 \kappa_1 f_2(h)} \left[\frac{\kappa_2 h + f_2(h) \log f_2(h)}{\kappa_2} \right. \\
&\quad \left. + \frac{(-\kappa_1 f_2(h) \log f_2(h) + \kappa_2 f_1(h) \log f_1(h))}{\kappa_1 (\kappa_2 - \kappa_1)} \right] \\
b_{14} &= \int_0^h \frac{1}{(f_2(s_3))^2} \int_0^{s_3} \frac{\xi f_2(\xi)}{(f_1(\xi))^2} d\xi ds_3 \\
&= \left[\frac{h}{(\kappa_2 - \kappa_1) f_2(h)} + \frac{\log f_2(h) - \log f_1(h)}{(\kappa_2 - \kappa_1)^2} \right] \left[\frac{1}{\kappa_1} - \frac{\kappa_2}{\kappa_1^2} \right] \\
&\quad - \frac{\kappa_2}{\kappa_1^2} \left[\frac{h}{\kappa_2 f_2(h)} + \frac{\log f_2(h)}{\kappa_2^2} \right]
\end{aligned}$$

$$\begin{aligned}
& - \left[\frac{\kappa_1 - 2\kappa_2}{\kappa_2 \kappa_1^3} \right] \left[\frac{\kappa_1 (\log f_2(h) - \log f_1(h))}{(\kappa_2 - \kappa_1)} - \frac{\log f_1(h)}{f_2(h)} \right] \\
c_1 &= \frac{1}{\kappa_1 h} \left[\left(\frac{\kappa_2 - \kappa_1}{\kappa_1} \right) \log f_1(h) + \kappa_2 h \right] \\
c_2 &= \frac{1}{\kappa_2 h} \left[\left(\frac{\kappa_1 - \kappa_2}{\kappa_2} \right) \log f_2(h) + \kappa_1 h \right]
\end{aligned}$$

The coefficients which must be evaluated in the limit when $\kappa_1 \rightarrow 0$, $\kappa_2 \rightarrow 0$, $\kappa_1 \rightarrow \kappa_2$, and $\kappa_1, \kappa_2 \rightarrow 0$ are as follows:

$$\kappa_1 \rightarrow 0$$

$$\begin{aligned}
a_2 &= h f_2(h/2) \\
a_5 &= \frac{1}{2} h^2 \\
a_8 &= \frac{1}{\kappa_2} \left[h + \frac{\log f_2(h)}{\kappa_2} \right] \\
a_9 &= \frac{1}{2} h^2 - \frac{1}{6} \kappa_2 h^3 \\
a_{11} &= \frac{1}{6} h^3 - \frac{1}{12} \kappa_2 h^4 \\
a_{12} &= \frac{\kappa_2 h + f_2(h) \log f_2(h)}{\kappa_2^2} \\
a_{13} &= \frac{h f_2(h/2)}{\kappa_2^2} + \frac{f_2(h) \log f_2(h)}{\kappa_2^3} \\
a_{14} &= -2 \frac{\kappa_2 h + f_2(h/2) \log f_2(h)}{\kappa_2^3} \\
b_3 &= h \\
b_6 &= \frac{1}{2} h^2 \\
b_{12} &= \frac{h^2}{2 f_2(h)} \\
b_{13} &= \frac{1}{\kappa_2^2 f_2(h)} \left[h f_2(h/2) + \frac{f_2(h) \log f_2(h)}{\kappa_2} \right]
\end{aligned}$$

$$b_{14} = \frac{1}{6} \frac{h^3}{f_2(h)}$$

$$c_1 = f_2(h/2)$$

$$\kappa_2 \rightarrow 0$$

$$a_3 = h$$

$$a_6 = \frac{1}{2} h^2$$

$$a_8 = \frac{1}{\kappa_1} \left[\frac{\log f_2(h)}{\kappa_1} + h \right]$$

$$a_{12} = \frac{h^2}{2f_1(h)}$$

$$a_{13} = \frac{1}{\kappa_1^2 f_1(h)} \left[h f_1(h/2) + \frac{f_1(h) \log f_1(h)}{\kappa_1} \right]$$

$$a_{14} = \frac{1}{6} \frac{h^3}{f_1(h)}$$

$$b_2 = h f_1(h/2)$$

$$b_5 = \frac{1}{2} h^2$$

$$b_8 = \frac{1}{\kappa_1} \left[\frac{\log f_1(h)}{\kappa_1} + h \right]$$

$$b_9 = \frac{1}{2} h^2 - \frac{1}{6} \kappa_1 h^3$$

$$b_{10} = \frac{1}{6} h^3$$

$$b_{11} = \frac{1}{6} h^3 - \frac{1}{12} \kappa_1 h^4$$

$$b_{12} = \frac{\kappa_1 h + f_1(h) \log f_1(h)}{\kappa_1^2}$$

$$b_{13} = \frac{1}{\kappa_1^2} \left[h f_1(h/2) + \frac{f_1(h) \log f_1(h)}{\kappa_1} \right]$$

$$b_{14} = -\frac{2}{\kappa_1^3} [\kappa_1 h - f_1(h/2) \log f_1(h)]$$

$$c_2 = f_1(h/2)$$

$$\kappa_1 \rightarrow \kappa_2$$

$$a_8 = \frac{1}{\kappa_1} \left[\frac{h}{f_1(h)} + \frac{f_1(h)}{\kappa_1} \right]$$

$$a_{13} = -\frac{1}{\kappa_1^2 f_1(h)} \left[\frac{\kappa_1 h + f_1(h) \log f_1(h)}{\kappa_2} + \frac{\kappa_1 h + \log f_1(h)}{\kappa_1} \right]$$

$$a_{14} = -2 \frac{\kappa_1 h + f_1(h/2) \log f_1(h)}{\kappa_1^3 f_1(h)}$$

$$b_8 = \frac{1}{\kappa_1} \left[\frac{h}{f_1(h)} + \frac{\log f_1(h)}{\kappa_1} \right]$$

$$b_{13} = -\frac{1}{\kappa_2^2 f_2(h)} \left[\frac{\kappa_2 h + f_2(h) \log f_2(h)}{\kappa_1} + \frac{\kappa_2 h + \log f_2(h)}{\kappa_2} \right]$$

$$b_{14} = -2 \frac{\kappa_2 h + f_2(h/2) \log f_2(h)}{\kappa_2^3 f_2(h)}$$

$$\kappa_1, \kappa_2 \rightarrow 0$$

$$a_8 = \frac{1}{2} h^2$$

$$a_{12} = \frac{1}{2} h^2$$

$$a_{13} = \frac{1}{6} h^3$$

$$a_{14} = \frac{1}{6} h^3$$

$$b_8 = \frac{1}{2}h^2$$

$$b_{12} = \frac{1}{2}h^2$$

$$b_{13} = \frac{1}{6}h^3$$

$$b_{14} = \frac{1}{6}h^3$$

BIBLIOGRAPHY

- [1] Abbott, M. B., "Chapter 7, Weak Solutions of the Equations of Open Channel Flow," *Unsteady Flow in Open Channels*, vol. 1, Mahmood and Yevjevich, eds., Water Resources Publications, 1975, p. 283-311.
- [2] Abbott, M. B. and Rodenhuis, G. S., "A Numerical Simulation of the Undular Hydraulic Jump," *Journal of Hydraulic Research*, vol. 10, 1972, p. 239-257.
- [3] Baker, A. J., "Initial-Value Problems, Convection/Diffusion," *Finite Element Computational Fluid Mechanics*, McGraw-Hill Book Co., Chapt. 4, 1983, p. 153-231.
- [4] Baker, A. J. and Iannelli, G. S., "Finite Element Modeling in Free-Surface Hydromechanics," *ASCE 1988 National Conference on Hydraulic Engineering*, Colorado State University, Aug. 1988, p. 594-599.
- [5] Baker, A. J. and Kim, J. W., "A Taylor Weak-Statement Algorithm for Hyperbolic Conservation Laws", *Int. Journal for Numerical Methods in Fluids*, vol.7, 1987, p. 489-520.
- [6] Becker, E. B., Carey, G. F. and Oden, J. T., *Finite Elements, An Introduction*, vol. I, Prentice-Hall, Inc., 1981, p. 196.
- [7] Bettess, P. and Bettess, J. A., "Analysis of Free Surface Flows using Isoparametric Finite Elements," *International Journal for Numerical*

Methods in Engineering, vol. 6, 1983, p. 1675-1689.

- [8] Boresi, A. P. and Chong, K. P., *Elasticity in Engineering Mechanics*, Elsevier Science Publishing Co., Inc., New York, 1987, p. 220.
- [9] Carnahan, B., Luther, H. A. and Wilkes, J. O., *Applied Numerical Methods*, John Wiley and Sons, Inc., 1969, p. 319.
- [10] Cassidy, J. J., "Irrotational Flow over Spillways of Finite Height," *Proceedings of the American Society of Civil Engineers*, vol. 91, no. EM6, December 1965, pp. 155-173.
- [11] Chakravarthy, S. R., "The Split-Coefficient Matrix Method for Hyperbolic Systems of Gasdynamic Equations," Ph.D. dissertation, Department of Aerospace Engineering, Iowa State University, Ames, 1979.
- [12] Chapman, R. S. and Kuo, C. Y., "Application of the Two-Equation $k-\epsilon$ Turbulence Model to a Two-Dimensional, Steady, Free Surface Flow Problem with Separation," *International Journal for Numerical Methods in Fluids*, vol. 5, 1985, p. 257-268.
- [13] Chow, V. T., *Open-Channel Hydraulics*, McGraw-Hill Book Company, Inc., 1959.
- [14] Courant, R., Friedrichs, K. O. and Lewy, H., "Über die Partiellen Differenzgleichungen der Mathematischen Physik," *Mathematische Annalen*, vol. 100, 1928, p.32-74. Translated to English in "On the Partial Difference Equations of Mathematical Physics," *IBM, J. Res. Dev.*, vol. 11, 1967, p. 215-234.

- [15] Courant, R., Isaacson, E. and Rees, M., "On the solution of Nonlinear Hyperbolic Differential Equations," *Communications on Pure and Appl. Math.*, vol. 5, 1952, p. 243-255.
- [16] Dakshinamoorthy, S., "High Velocity Flow Through Expansions." *Proc. 17th Congress IAHR*, Baden-Baden, West Germany, vol. 2, 1977, p. 373-381.
- [17] Daubert, A. and Graffe, O., "Quelques aspects des écoulements presque horizontaux a deux dimensions en plan et non-permanents application aux estuaires," *La Houille Blanche*, vol. 8, 1967, p. 847-860.
- [18] Dendy, J. E., "Two Methods of Galerkin-Type Achieving Optimum L^2 Rates of Convergence for First-Order Hyperbolics," *SIAM Journal of Numerical Analysis*, vol. 11, 1974, p. 637-653.
- [19] Donea, J. "A Taylor-Galerkin Method for Convective Transport Problems," *International Journal for Numerical Methods in Engineering*, vol. 20, 1984, p. 101-119.
- [20] Dressler, R. F., "New Nonlinear Shallow-Flow Equations with Curvature." *Journal of Hydraulic Research*, vol. 16, no. 3, 1978, p. 205-222.
- [21] Dressler, R. F., and Yevjevich, V., "Hydraulic-Resistance Terms Modified for the Dressler Curved-Flow Equations," *Journal of Hydraulic Research*, vol. 22, no. 3, 1984, p. 145-156.
- [22] Dressler, R.F. and Yevjevich, V.M., "Comparison of the Dressler and de Saint-Venant Equations for Shallow Curved Flow," *Proceedings XX*

Congress of the International Association for Hydraulic Research, Moscow, 1983, p. 170-179.

- [23] Drolet, J. and Gray, W. G., "On the well posedness of some wave formulations of the shallow water equations," *Advances in Water Resources*, vol. 11, June, 1988, p. 84-91.
- [24] Friedrichs, K. O., "Appendix. On the Derivation of the Shallow Water Theory," *Communications on Applied Mathematics*, vol. I, no. 1, 1948, p. 81-87.
- [25] Gabutti, B., "On Two Upwind Finite Difference Schemes for Hyperbolic Equations in Non-Conservative Form," *Computers and Fluids*, vol. 11, no. 3, 1983, p. 207-230.
- [26] Gharangik, A. M. and Chaudhry, M. H., "Numerical Simulation of Hydraulic Jump," ASCE, *Journal of Hydraulic Engineering*, vol. 117, no. 9, Sep., 1991, p. 1195-1211.
- [27] Henderson, F. M., *Open Channel Flow*, The Macmillan Co., New York, 1966.
- [28] Henderson, F. M. and Tierney, D. C., "Flow at the Toe of A Spillway," *La Houille Blanche*, no. 1, 1963, p. 42-50.
- [29] Hughes, T. J. R. and Brooks, A. N., "A Theoretical Framework for Petrov-Galerkin Methods with Discontinuous Weighting Functions: Applications to the Streamline-Upwind Procedures," *Finite Elements in Fluids*, R. H. Gallagher, et. al., eds., vol. 4, J. Wiley and Sons, London, 1982.

- [30] Ikegawa, M. and Washizu, K., "Finite Element Method Applied to Analysis of Flow over a Spillway Crest," *International Journal for Numerical Methods in Engineering*, vol. 6, 1973, p. 179-189.
- [31] Ippen, A. T. and Dawson, J. H., "Design of Channel Contractions." *High-Velocity Flow in Open Channels, A Symposium*, Transactions ASCE, vol. 116, 1951, p. 326-346.
- [32] Jiménez, O. F. and Chaudhry, M. H., "Computation of Supercritical Free-Surface Flows," ASCE, *Journal of Hydraulic Engineering*, vol. 114, no. 4, April, 1988, p. 377-395.
- [33] Katopodes, N. D., "Two-Dimensional Surges and Shocks in Open Channels," ASCE, *Journal of Hydraulic Engineering*, vol. 110, no. 6, June, 1984, p. 794-812.
- [34] Katopodes, N. D., "Explicit Computation of Discontinuous Channel Flow," ASCE, *Journal of Hydraulic Engineering*, vol. 112, no. 6, June, 1986, p. 456-475.
- [35] Keller, J. B., "The Solitary Wave and Periodic Waves in Shallow Water," *Communications on Applied Mathematics*, vol. I, no. 1, 1948, p. 323-339.
- [36] King, H. W. and Brater, E. F., *Handbook of Hydraulics for the Solution of Hydrostatic and Fluid-flow Problems*, McGraw-Hill, Inc., 1963.
- [37] Kinnmark, I., "The Shallow Water Wave Equations: Formulation, Analysis and Application," *Lecture Notes in Engineering*, vol. 15, Brebbia and Orszag, eds., Springer-Verlag, 1985.

- [38] LéMéhauté B., *An Introduction to Hydrodynamics and Water Waves*. Springer-Verlag Inc., New York, 1976.
- [39] Liggett, J. A. and Vasudev, S. U., "Slope and Friction Effects in Two Dimensional High Speed Flow," *Proc. 11th International Congress IAHR*. Leningrad, U.S.S.R., vol. 1, 1965, p. 1-12.
- [40] Lighthill J., *Waves in Fluids*, Cambridge University Press, Cambridge, Great Britain, 1980, pp. 217.
- [41] Lipschutz, M. M., *Differential Geometry*, Schaum's Outline Series in Mathematics, McGraw-Hill Book Co., 1969.
- [42] Lohner, R., Morgan, K., and Zienkiewicz, O. C., "The Solution of Nonlinear Hyperbolic Equation Systems by the Finite Element Method," Institute for Numerical Methods in Engineering, University College of Swansea, England, 1983.
- [43] Wolfram, S., *Mathematica: A System for Doing Mathematics by Computer*. Addison-Wesley Publishing Co., Inc., 1988. (Computer program: Mathematica Version 1.2f33 Enhanced, Wolfram Research Inc., 1988-1989).
- [44] Moayeri, M. S., "Flow in Channels with Smooth Curved Boundaries," ASCE, *Journal of the Hydraulics Division*, vol. 99, no. HY12, Dec., 1973, p. 2217-2232.
- [45] Moretti, G., "The λ -scheme," *Computers in Fluids*, vol. 7, no. 3, 1979, p. 191-205.

- [46] Platzman, G. W., "Normal Modes of the World Ocean. Part 1, Design of a Finite Element Barotropic Model," *Journal of Physical Oceanography*, vol. 8, 1978, p. 323-343.
- [47] Raymond, W. H. and Garder A., *Mon. Weather Rev.*, no. 104, 1976, p. 1583-1590.
- [48] Reynolds, A. J., *Turbulent Flows in Engineering*, John Wiley & Sons, London, 1974, p. 196-230.
- [49] Rodi, W., "Turbulence Models and Their Application in Hydraulics - A State of the Art Review," State-of-the-Art Paper, *International Association for Hydraulic Research*, Delft, Netherlands, 1980.
- [50] Saint Venant, B. De. "Theory of Unsteady Flow, with Application to River Floods and to Propagation of Tides in River Channels," *Comptes rendus*, vol. 73, Academy of Science, Paris, 1871, p. 148-154, 237-240. (Translated into English by US Army Corps of Engineers, no. 49-g, US Army Engineer Waterways Experiment Station, Vicksburg, Miss., 1949).
- [51] Sivakumaran, N. S., "Shallow-Flow Over Curved Beds," Doctoral Dissertation, Asian Institute of Technology, Bangkok, Thailand, 1981.
- [52] Sivakumaran, N. S., Hosking, R. J., and Tingsanchali, T., "Steady Shallow Flow over a Spillway," *Journal of Fluid Mechanics*, vol. 111, 1981, p. 411-420.
- [53] Sivakumaran, N. S., Tingsanchali, T., and Hosking, R. J., "Steady Shallow Flow Over Curved Beds," *Journal of Fluid Mechanics*, vol. 128, 1983, p.

469-487.

- [54] Sivakumaran, N.S., and Yevjevich, V., "Experimental Verification of the Dressler Curved-Flow Equations," *Journal of Hydraulic Research*, vol. 25, no. 3, 1987, p. 373-391.
- [55] Steger, J. L. and Warming, R. F., "Flux Vector Splitting of the Inviscid Gas Dynamics Equations with Applications to Finite Difference Methods," *Journal of Computational Physics*, vol. 40, 1981, p. 263-293.
- [56] Stoker, J.J., *Water Waves, The Mathematical Theory with Application*, Interscience Publishers, Inc., 1976, p. 17-32.
- [57] Tate, C. H., Private Communication, Waterways Experiment Station, November, 1991.
- [58] Verboom, G. K., Stelling, G. S., and Officier, M. J., "Boundary conditions for the shallow water equations," *Engineering Applications of Computational Hydraulics*, M. B. Abbott and J. A. Cunge, eds., vol. 1, Chapt. 11, Pitman Publishing, Inc., Marshfield Mass., 1982, p. 230-262.
- [59] Walters, R. A. and Carey, G. F., "Analysis of Spurious Oscillation Modes for the Shallow Water and Navier-Stokes Equations," *J. Computers and Fluids*, vol. 11, no. 1, 1983, p. 51-68.
- [60] Walters, R.A., and Cheng, R.T., "A Two-Dimensional Hydrodynamic Model of a Tidal Estuary," *Surface Flow*, W. Gray, ed., 1984, p. 34-42.

- [61] Wang, B. N. and Hoffman, J. D., "A Simple Physical Approach for Deriving the Characteristic Equations of Fluid Dynamics," *International Journal for Numerical Methods in Fluids*, vol. 10, 1990, p. 401-410.
- [62] Watters, G. and Street, R. L., "Two-Dimensional Flow Over Sills in Open Channels," ASCE, *Journal of the Hydraulics Division*, vol. 90, no. HY4, July, 1964, p. 107-140.

REPORT DOCUMENTATION PAGE

Form Approved
OMB No. 0704-0188

Public reporting burden for this collection of information is estimated to average 1 hour per response, including the time for reviewing instructions, searching existing data sources, gathering and maintaining the data needed, and completing and reviewing the collection of information. Send comments regarding this burden estimate or any other aspect of this collection of information, including suggestions for reducing this burden, to Washington Headquarters Services, Directorate for Information Operations and Reports, 1215 Jefferson Davis Highway, Suite 1204, Arlington, VA 22202-4302, and to the Office of Management and Budget, Paperwork Reduction Project (0704-0188), Washington, DC 20503

1. AGENCY USE ONLY (Leave blank)		2. REPORT DATE August 1993	3. REPORT TYPE AND DATES COVERED Final report	
4. TITLE AND SUBTITLE Free-Surface Flow Over Curved Surfaces			5. FUNDING NUMBERS	
6. AUTHOR(S) R. C. Berger, Jr.				
7. PERFORMING ORGANIZATION NAME(S) AND ADDRESS(ES) U.S. Army Engineer Waterways Experiment Station Hydraulics Laboratory 3909 Halls Ferry Road, Vicksburg, MS 39180-6199			8. PERFORMING ORGANIZATION REPORT NUMBER Technical Report HL-93-10	
9. SPONSORING / MONITORING AGENCY NAME(S) AND ADDRESS(ES)			10. SPONSORING / MONITORING AGENCY REPORT NUMBER	
11. SUPPLEMENTARY NOTES Available from National Technical Information Service, 5285 Port Royal Road, Springfield, VA 22161.				
12a. DISTRIBUTION / AVAILABILITY STATEMENT Approved for public release; distribution is unlimited.			12b. DISTRIBUTION CODE	
13. ABSTRACT (Maximum 200 words) Flood flows in excess of a reservoir's capacity must be passed downstream in a manner that does not endanger the dam or surrounding hydraulic structures. This is not a trivial task as the flow must fall a great distance to reach the riverbed. These high current velocities coupled with a free surface can easily lead to regions of low pressure in which cavitation may occur or the formation of standing waves and an uneven flow distribution. Poor flow distribution will yield circulation and high velocities at the base of the spillway (or outlet channel) known as the "stilling basin," resulting in downstream scour, potentially undermining the structure, causing bank erosion and stilling basin damage. Numerical models of free-surface spillway flows must address high flow velocities and the nonhydrostatic pressure distribution over the curved spillway bed. Common shallow-water models invoke the hydrostatic assumption, and in the case of the St. Venant equations, also the mild-slope assumption and may not be adequate. This investigation develops the equations of a more general shallow-water formulation that includes bed curvature effects. The equations have lateral and longitudinal resolution and an assumed bed-normal (Continued)				
14. SUBJECT TERMS Finite element Petrov-Galerkin Nonhydrostatic Shallow water			15. NUMBER OF PAGES 149	
			16. PRICE CODE	
17. SECURITY CLASSIFICATION OF REPORT UNCLASSIFIED	18. SECURITY CLASSIFICATION OF THIS PAGE UNCLASSIFIED	19. SECURITY CLASSIFICATION OF ABSTRACT	20. LIMITATION OF ABSTRACT	

13. (Concluded).

velocity distribution. No restriction is placed on the velocity in the plane parallel to the bed. These equations are derived through a singular perturbation analysis in a shallowness parameter.

A finite element model is then constructed that represents a discrete version of these equations, and its usefulness is tested in comparison to water surface and pressure measurements gathered in flumes. A Petrov-Galerkin scheme is used in which the degree of modification of the original Galerkin test function is proportional to the eigenvalues, which represent the wave speed. Results with this scheme are compared to those for the standard steep-slope shallow-water equations and the St. Venant equations. The results demonstrate that the new generalized shallow-water equations are a significant improvement over these more conventional equations near the spillway crest and thus in the prediction of the spillway capacity. The St. Venant equations compare more poorly along the spillway face, but this is shown to be a result of the mild-slope assumption, not curvature. Laterally, the new generalized shallow-water equations provide only slight improvement over conventional equations in that the water surface is generally controlled by short-wave phenomena, and these models are all essentially long-wave models. They do provide some qualitative guidance on spillway performance.